NUMERICAL AND EXPERIMENTAL INVESTIGATIONS INTO THE NONLINEAR DYNAMICS OF A MAGNETO-ELASTIC SYSTEM

JEE IAN TAM, '13

SUBMITTED TO THE
DEPARTMENT OF MECHANICAL AND AEROSPACE ENGINEERING
PRINCETON UNIVERSITY
IN PARTIAL FULFILLMENT OF THE REQUIREMENTS OF
UNDERGRADUATE INDEPENDENT WORK.

FINAL REPORT

MAY 2, 2013

PHILIP HOLMES
HOWARD STONE
MAE 442
116 PAGES
FILE COPY

This thesis represents my own work in accordance with University regulations.

Abstract

We present an analytical, numerical and experimental treatment of the magneto-elastic system given by Moon and Holmes [1] for a cantilevered ferromagnetic beam between two magnets. A single-mode approximation is assumed, and the nonlinear quantities in the governing ODE of the modal amplitude that arise due to magnetic forces and moments are computed numerically using an algorithm presented by Derby [6] by modelling the magnets as ideal solenoids. This numerical model enables us to compute the static force distribution as a function of beam displacements for fixed experimental parameters. The magneto-elastic system is also built in order to compare the model with experimental data. A strain gauge is used to measure the deflection of the beam, and an electronic circuit is also constructed to collect and process data to obtain time series for the position and velocity of the beam. We find that the model displays good agreement with experiment for the static case where no external forcing is present. The predictions of buckled equilibria positions, and also of the natural frequency of vibrations about those positions from the model are close to those that of experimental results. The topological structure of the static force distribution as computed from the model is found to be similar to that of the Duffing oscillator in the case of a double-well potential, as seen by both having similarly-structured basins of attraction in the static case. Furthermore, we observe cases of single and triple well potentials from the model as well for certain parameters as well, and bifurcation diagrams and bifurcation sets are presented for varying physical parameters. Catastrophes involving stable and unstable surfaces of equilibria are also investigated, and we observe surfaces similar to those seen in cusp catastrophes[14]. In the presence of external forcing of the system, the experimental data as well as the numerical model display qualitative agreement with the theory of the Duffing oscillator [3], and we present examples of “strange attractor” structures over the Poincaré Map for moderate forcing amplitudes from both experimental and numerical results. Bifurcations of the fixed points of the Poincaré Map are also investigated using the numerical model. Discrepancies between the model and experimental data are highlighted, and limitations of the model are discussed in relation to experimental results as well as with consideration to the Duffing oscillator as an analytical model of the system.

Acknowledgements

I would like to thank my advisor, Prof. Philip Holmes, for providing me an immense amount of guidance and assistance in completing my thesis. He has been extremely patient and understanding when dealing with all of my questions, and I will always be grateful towards him for helping me in my learning throughout this journey.

I would like to thank Prof. Howard Stone for taking the time to read my thesis as my second reader.

I would like to thank the Princeton MAE department for granting me a generous allowance of funds, without which half of my thesis would not have been possible. In particular, I would like to thank Jo-Ann Kropilak Love and Prof. Luigi Martinelli for helping me secure the additional funding needed for my thesis, and also for enabling my application for such funds to be as smooth as possible. Correspondingly, I would like to thank the John Marshall II Memorial Award and Princeton SEAS for granting me additional funds as well.

I would like to thank Jonathan Prevost for allowing me use of his laboratory space to run my experiments. Thanks also goes to Mike Vocaturo, Glenn Northey and Chris Zada for providing me technical assistance in the lab as well as in the machine shop. Similar thanks goes to Prof. Michael Littman for providing me advice regarding my experiment.

I would like to thank Sonya Chu for being there with me throughout my thesis.

I am also forever grateful towards my parents Pak Cheong Tam and Li Yi Liang for giving me the opportunity to actually attend Princeton and complete a thesis, amongst all of the numerous opportunities that they have already provided me with.

Final thanks go to the chirping birds for reminding me to enjoy the morning sun.

To those who seek.

Contents

List of Figures

List of Symbols

α	Coefficient of linear term in Duffing's equation.	1
β	Coefficient of cubic term in Duffing's equation.	1
t	Time variable.	1
L	Length of undeformed beam.	4
s	Arc-length coordinate along beam.	4
u	Displacement of beam element along the x direction.	4
v	Displacement of beam element along the y direction.	4
F_x	Magnetic force per unit length along the beam in the x direction.	6
F_y	Magnetic force per unit length along the beam in the y direction.	6
C	Moment per unit length along the beam.	6
V_0	Position of platform undergoing external excitation relative to stationary state in the x-direction.	6
m	Mass per unit length along the beam.	6
E	Young's Modulus.	6
I	Area/Second Moment of Inertia.	6
w	Beam width.	6
$\triangle$	Beam thickness.	6
D	Flexural rigidity of beam.	6
T	Tension in beam created by axial forces along beam, defined as $T(s,v) = \int_s^L F_x(s,v)\,ds$	6
θ	Angle of beam element relative to x-axis.	6
ϕ	Spatial mode shape of beam in single-mode approximation.	7
a	Modal amplitude of beam in single-mode approximation.	7
F_{static}	Distribution over all contributing terms in the static case (no forcing).	9
F_{beam}	Contributing term in governing ODE due to elasticity of beam.	9
F_{beam}	Contributing term in governing ODE due to presence of magnetic field.	10
F_{moment}	Contributing term in governing ODE due to moment on the beam induced by magnetic field.	10

F_{axial}	Contributing term in governing ODE due to axial forces in the x direction on the beam induced by magnetic field.	10
$F_{transverse}$	Contributing term in governing ODE due to lateral forces in the y direction on the beam induced by magnetic field	10
A_0	Forcing amplitude of shaker.	10
ω	Forcing frequency of shaker in radians per second.	10
f	Forcing frequency of shaker in Hz.	10
v_L	Beam tip displacement in the y-direction.	10
P	Forcing amplitude in Duffing's equation.	10
δ	Damping coefficient in Duffing's equation.	10
ζ	Damping ratio.	11
ω_0	Natural frequency of beam without magnets present.	11
a_0	Buckled beam tip displacement from vertical beam tip position at $y = 0$.	11
n	Number of turns through equivalent solenoid.	12
I	Current through equivalent solenoid.	12
$B_{surface}$	Magnetic field strength at surface along center axis of cylindrical magnet.	12
r	Magnet radius.	12
h	Magnet height.	12
B_x	Magnetic field component in the x-direction.	13
B_y	Magnetic field component in the y-direction.	13
M_x	Magnetization of beam in x-direction	13
M_y	Magnetization of beam in y-direction	13
A	Cross-sectional area of beam.	13
χ	Volumetric magnetic susceptibility.	13
μ_r	Relative magnetic permeability.	13
μ_0	Magnetic constant / vacuum permeability.	13
ω_d	Damped frequency of beam oscillations without magnets present in radians per second	22
f_d	Damped frequency of beam oscillations without magnets present in Hz.	22
J	Jacobian of system.	24
ω_1	Natural frequency of beam oscillations about equilibrium buckled position with magnets present in radians per second.	26
f_1	Natural frequency of beam oscillations about equilibrium buckled position with magnets present in Hz.	26
d	Distance between magnet centers.	26
$Q(t)$	Total energy of the Duffing oscillator	30

T	Forcing Period.	52
Σ	Suface over which Poincaré map is taken.	52
G	Poincaré map of system	52
S	Strange attractor of Poincaré map	57

Chapter 1

Introduction

Nonlinear dynamics is usually introduced to students with canonical examples of nonlinear systems. One of these systems is the Duffing oscillator, whose dynamics is given by Duffing's equation:

$$\ddot{x} = \alpha x - \beta x^3 - \delta \dot{x} + Pcos(\omega t). \tag{1.0.1}$$

The Duffing oscillator is an example of a non-linear, second-order, non-autonomous, periodically-forced oscillator with non-linear restoring force. It is a relatively simple model which is known to display chaotic solutions in response to periodic forcing [15].

A physical system that can be modelled by Duffing's equation is a beam that is clamped at one end and buckled at the other end between two magnets on a platform which is periodically forced. (See figure 1.1) Moon and Holmes [1] have showed that the dynamics of this physical system can be described by Duffing's equation with $\alpha > 0$ and $\beta > 0$, corresponding to the dynamics of a particle in a double-well potential. Furthermore, experiments by Moon and Holmes have also demonstrated chaotic motions when moderate periodic forcing is applied to the platform, as evidenced from the structure of a strange attractor recorded on the Poincaré map. Under such chaotic motions, the beam jumps erratically and unpredictably back and forth from one equilibrium point to the other. Thus, such a physical system is invaluable not only as a pedagogical example of non-linear systems which display chaotic motions, but also as a simple model of possible dynamics in magneto-elastic systems such as motors, generators, Maglev trains and magneto-elastic load cells.

To compare the dynamics of Duffing's equation with that of the physical system, one would normally have to build the system, perform experiments on the system and then derive the parameters of Duffing's equation (α, β and δ) from the experimental data. Computing these parameters also enables one to make further predictions about the system via

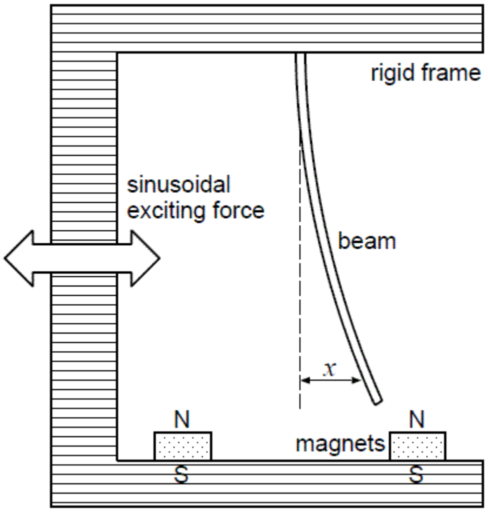

Figure 1.1: Physical analogue of the Duffing oscillator, taken from figure 3 in [8].

numerical simulations(e.g. for which forcing amplitudes or frequencies would one obtain chaotic motions).

However, in some cases one would like to be able to specify the physical parameters of the system (magnet spacing, beam dimensions, magnet size and so on) and obtain results in the form of simulation of a time series for the dynamics of the beam before building the system. Not only does this give a good estimate of what range of system parameters are feasible, it allows one to derive a more accurate approximation to the restoring forces compared to the cubic of equation 1.0.1, and also to run optimization and sensitivity analyses to find chaotic motions and also possibly simulate a control law on the system based on physical parameters to stabilize periodic orbits. Successful control of such a physical system has already been demonstrated by Hikihara and Kawagoshi based on forcing frequency as a control parameter [16].

Furthermore, it allows for the simulation of cases in which the symmetry of the system is broken (e.g. field strength of the magnets are different, or the beam is not centered between the magnets). In these cases Duffing's equation no longer models the system accurately since the restoring force is no longer symmetric around the center point between the magnets. Examples of these cases will be presented below, although the focus will be more on the symmetric case.

In the sections below the partial differential equation governing the system as given by Moon and Holmes in [1] is first presented. An analytic expression for the mode shape $\phi(s)$ of a single-mode approximation is then given, which will be used in numerical computations. The ordinary differential equation for the modal amplitude $a(t)$ is also presented, which will be the equation that is simulated.

In order to compute the non-linear quantities associated with the magnetic field, the magnets are treated as ideal finite solenoids, and the corresponding magnetic fields are computed using an algorithm given by Derby [6]. The magnetic forces and moments are then computed. Combining the magnetic forces and moments with numerical integrations of $\phi(s)$ and its derivatives gives all the information needed to compute the static forces on the beam, and thus it is possible to numerically simulate the ODE for the dynamics of $a(t)$. Two different ways of numerically simulating the resulting ODE are compared: The first way is to simulate the system using the fully computed static force distribution, the second way is the approximate it using a cubic polynomial.

The magneto-elastic system is also constructed, and experimental data is taken from it to calculate parameters of Duffing's equation. This allows us to compare experimental results with numerical simulations of the system based on physical parameters of the system. Poincaré maps generated from experimental data and numerical simulations are presented. Bifurcation diagrams based on the developed computational model are also presented.

Chapter 2

Theory and Computations for Model

In this chapter we introduce the governing partial differential equations for the motion of the beam as given by Holmes in [1], and from there we derive the governing ordinary differential equation (ODE) for the modal amplitude $a(t)$ of a single-mode approximation. We then explain the computational methods used to calculate the terms in the governing ODE, as well as the simplifications to the resulting model that would give the equations for the Duffing oscillator.

2.1 Theoretical model

We first describe the dynamics of the system. The coordinate system used for the clamped beam is shown below in figure 2.1. Define L as the length of the undeformed beam. At equilibrium (no magnetic or shaker forces), the beam lies along the x-axis.

Define s as the arc-length coordinate along the length of the beam, where $s = 0$ at the origin of the coordinate system shown above (the clamping point of the beam) and $s = L$ at the tip of the beam. Clearly $s \in [0, L]$.

Thus, for any point on the beam with coordinate s along the length of the undeformed beam, we can describe its displaced position from equilibrium as $(s + u(s,t), v(s,t))$, where $u(s,t)$ is the displacement in the x-direction and $v(s,t)$ is the displacement in the y-direction.

The primary variable of interest is the y-displacement of the beam from equilibrium, $v(s,t)$ in the presence of a static, non-homogeneous magnetic field. Moon and Holmes showed that the partial differential equation describing $v(s,t)$ can be written as equation 2.1.1. Here the dependence of various quantities on s, v and t is emphasized, and a dependence on

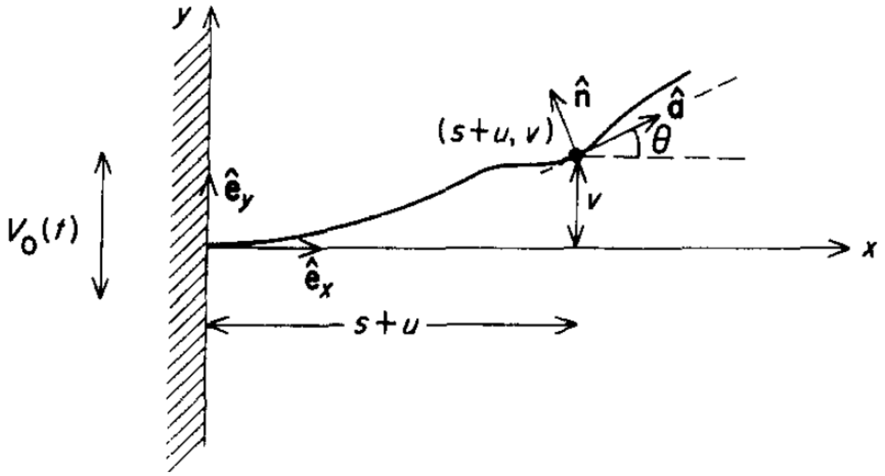

Figure 2.1: Coordinate system and related quantities for the cantilevered beam, taken from figure 4(a) in [1].

(s, v) is shorthand to mean dependence on $(s, v(s,t))$. It is important to remember that the quantities related to the magnetic field depend on the overall shape of the beam in the magnetic field. An alternate derivation of the equation 2.1.1 based on linear beam theory using differentials is presented in appendix A.

$$F_y(s,v) - D\frac{\partial^4 v(s,t)}{\partial s^4} + \frac{\partial}{\partial s}\left(-C(s,v) + T(s,v)\frac{\partial v(s,t)}{\partial s}\right) = m\left(\frac{\partial^2 v(s,t)}{\partial t^2} + \frac{\partial^2 V_0(t)}{\partial t^2}\right), \tag{2.1.1a}$$

$$T(s,v) = \int_s^L F_x(s,v)\, ds, \tag{2.1.1b}$$

where:

v is the displacement of the beam in the y direction.

F_x and F_y are the magnetic forces per unit length along the beam in the x and y direction respectively.

C is the moment per unit length along the beam due to magnetic forces

m is the mass per unit length along the beam.

V_0 is the position of the platform that undergoes external excitation (and is connected to the whole system) relative to its stationary state.

D is the flexural rigidity of the beam, given by $D = EI$, where E is the Young's Modulus and I is the area moment of inertia given by $I = \frac{w\triangle^3}{12}$ for a beam of width w and thickness $\triangle$.

The term $T(s,v)$ in equation 2.1.1 can be interpreted as the tension in the beam created by the axial magnetic forces along the beam, $F_x(s,v)$.

Equation 2.1.1 was derived by Moon and Holmes with the following assumptions:

1. The beam is inextensible. This is equivalent to the constraint $\left(1+\frac{\partial u}{\partial s}\right)^2+\left(\frac{\partial v}{\partial s}\right)^2=1$. ([20] ch.9 pg. 339)
2. We assume a linear elastic model for the beam with a constant flexural rigidity, and thus all nonlinear forces are due to the magnetic field. Therefore, all nonlinearities in slope and curvature in the beam can be neglected since experimentally the elastic behaviour of the beam is almost linear under nonmagnetic forces. This is equivalent to the approximation $\theta \approx \frac{\partial v}{\partial s}$.
3. Gravitational forces are neglected on the basis that the elastic and magnetic forces on the beam are much greater than the gravitational forces.
4. We also make the assumption that $u(s,t)\approx 0$ in the linear beam approximation. This is reasonable under the expectation that the magnitude of the elastic and magnetic forces in the x-direction are much smaller than the magnitude of the forces in the y-direction. This is based on the cantilevered setup of the beam between the two magnets, and it is indeed observed from the experimental setup that the magnitude of displacements in the y-direction is much greater than the magnitude of displacements in the x-direction. Thus, the quantities in equation 2.1.1 only depend on the displacement of the beam in the y-direction. Henceforth, all mention of "beam displacement" will be referring to the beam displacement in the y-direction.

We introduce notation for partial differentiation. Henceforth, primed terms ($[]'$) denote partial differentiation with respect to s, and over-dotted terms ($\dot{[]}$) denote partial differentiation with respect to t. We can thus rewrite equation 2.1.1 as

$$F_y(s,v) - Dv'''' - C' + [T(s,v)v']' = m\left(\ddot{v}+\ddot{V_0}\right), \tag{2.1.2a}$$

$$T(s,v)=\int_s^L F_x(s,v)\,ds. \tag{2.1.2b}$$

To convert the partial differential equation in equation 2.1.2 to a ordinary differential equation, a single-mode approximation for the beam displacement is prescribed. This is equivalent to specifying $v(s,t)=\phi(s)a(t)$, where $\phi(s)$ defines the spatial mode shape and

$a(t)$ the time-dependent amplitude. Experimentally, we observe no buckling of the beam to the second mode due to the relatively low compressive axial loads and moments compared to the lateral forces. Therefore, we consider the single-mode approximation as a good one in describing the beam shape over time. Furthermore, Holmes and Marsden have showed [4] that this approximation does not result in a loss in the qualitative information about the behaviour of the beam over time, a result due to the application of the Center Manifold Theorem ([2],[5]) to the dynamics of the problem. The result is that we can ignore all but the most unstable mode(s) of the vibration, and thus can use the single-mode approximation since it is the dominant unstable mode of the system.

Here we shall take $\phi(s)$ as the first beam mode for the linear scenario $-Dv'''' = m\ddot{v}$, which disregards all magnetic forces on the beam. We solve for $\phi(s)$ by specifying $v(s,t) = \phi(s)a(t)$ in equation 2.1.2, solving the equation by separation of variables and imposing boundary conditions for a clamped-free beam.

One might wonder whether it is possible to obtain a more accurate equation for $\phi(s)$ by solving the non-linear scenario. That is, specifying $v(s,t) = \phi(s)a(t)$ for equation 2.1.2 and then trying to solve for $\phi(s)$ based on numerically computed values for F_y , F_x and C (The numerical method that can be used to obtain these quantities will be discussed later in section 2.1.2). This will most likely involve numerical solutions for $\phi(s)$ as equation 2.1.2 is nonlinear. However, the nonlinearities involved in this problem are not trivial. F_y , F_x and C in equation 2.1.2 depend on the displacement v (and therefore $\phi(s)$) themselves, and so one will likely have to resort to an iterative method to compute $\phi(s)$. Furthermore, even if one manages to obtain such a numerical solution, another downside of lacking an analytic solution for $\phi(s)$ is the lack of precision later on when we have to compute the fourth derivative of $\phi(s)$. Thus, in the view of a simpler and more manageable model, we choose to solve for $\phi(s)$ based on the linear scenario mentioned in the previous paragraph.

We do note that it is possible to make this easier by assuming that $F_x = 0$ and that T and C are constant. Analytical solutions for this case are known [13] but the nonlinearities will still have to be dealt with using an iterative method as one has to assume some $\phi(s)$ to numerically compute $F_x(s,v)$ and $C(s,v)$ which would then be averaged to obtain the constants T and C.

For the classical linear beam equation, $-Dv'''' = m\ddot{v}$. For the cantilevered spatial boundary conditions corresponding to $v(0,t) = v'(0,t) = 0$ and $v''(L,t) = v'''(L,t) = 0$, we obtain the following expressions that define $\phi(s)$ [12]:

$$\phi(s) = c\left[K(sinh(ks) - sin(ks)) + (cosh(ks) - cos(ks))\right], \tag{2.1.3a}$$

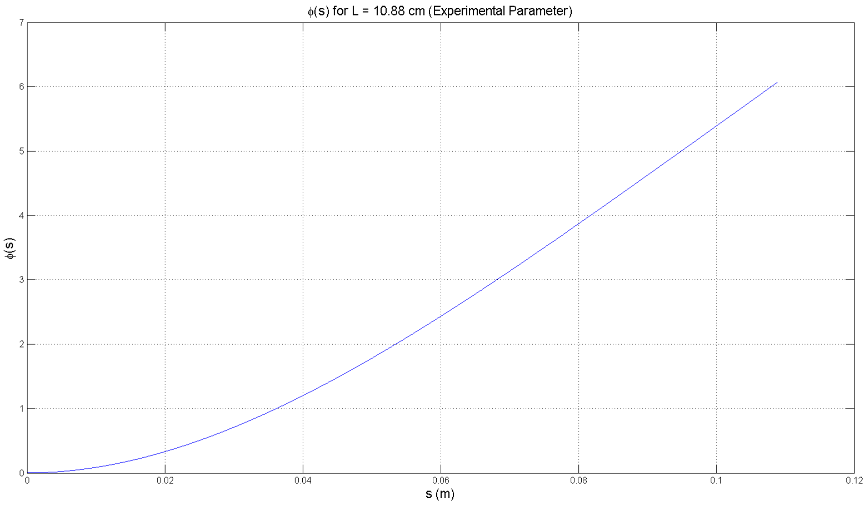

Figure 2.2: Plot of $\phi(s)$.

where k is defined by the constraint

$$cosh(kL)cos(kL) = 1, \tag{2.1.3b}$$

implying that $kL \approx 1.87510407$, and

$$K = -\frac{cos(kL) + cosh(kL)}{sin(kL) + sinh(kL)}. \tag{2.1.3c}$$

The constant c in equation 2.1.3a is chosen such that $\int_0^L \phi^2(s)\,ds = 1$, and we determine c numerically. Also, we can easily derive the analytical forms of $\phi'(s), \phi''(s)$ etc. from equation 2.1.3a. Having specified an analytic equation for $\phi(s)$, we substitute the single-mode approximation $v(s,t) = \phi(s)a(t)$ into equation 2.1.2, multiply all terms by $\phi(s)$ and take the integral of all terms over the beam length. The final result is a differential equation for the modal amplitude $a(t)$. The full derivation of these steps are given in appendix B.

$$\begin{aligned} m\ddot{a} = &\int_0^L C(s,a)\phi'(s)\,ds - \left[\int_0^L T(s,a)(\phi'(s))^2\,ds + D\int_0^L (\phi''(s))^2\,ds\right] a \\ &+ \int_0^L F_y(s,a)\phi(s)\,ds - m\ddot{V}_0(t)\int_0^L \phi(s)\,ds. \end{aligned} \tag{2.1.4}$$

Note that the signs of the terms containing T and C in equation 2.1.4 have been flipped compared the same terms in equation 2.1.2 due to the use of integration by parts.

In equation 2.1.1 we emphasized the dependence of quantities on s and v. In equation 2.1.4 the dependence of quantities on v has been replaced by a dependence on a since in the single-mode approximation, the dependence of $v(s,t)$ on $\phi(s)$ is already captured by the dependence on s, and thus we represent the dependence of $v(s,t)$ on $a(t)$ by the dependence on a.

Equation 2.1.4 is the governing ODE for the modal amplitude $a(t)$, and will be the main equation that will be used in numerical simulations.

Rearranging equation 2.1.4, we get

$$m\ddot{a} = -\left[\int_0^L T(\phi')^2\,ds + D\int_0^L (\phi'')^2\,ds\right]a + \int_0^L F_y\phi\,ds + \int_0^L C\phi'\,ds - m\ddot{V_0}\int_0^L \phi\,ds. \tag{2.1.5}$$

If we define

$$F_{static}(a) = \frac{1}{m}\left[-\left(\int_0^L T(\phi')^2\,ds + D\int_0^L (\phi'')^2\,ds\right)a + \int_0^L F_y\phi\,ds + \int_0^L C\phi'\,ds\right], \tag{2.1.6}$$

then we can rewrite equation 2.1.5 as

$$\ddot{a} = F_{static}(a) - \ddot{V_0}\int_0^L \phi\,ds. \tag{2.1.7}$$

Equation 2.1.7 defines a vector field over a, $\dot{a}$ and t. The $\ddot{V_0}\int_0^L \phi\,ds$ term is a non-inertial term that represents the contribution of the external shaker excitation to the dynamics of the modal amplitude. In the static case, the platform is stationary (no excitation), then $V_0(t) = 0$ for all t and thus equation 2.1.7 takes the form $\ddot{a} = F_{static}(a)$, an autonomous ODE.

Equation 2.1.6 is thus the governing equation behind the dynamics of the system in the static case. Looking at the terms in F_{static}, we see that we can write the equation as

$$F_{static}(a) = F_{beam}(a) + F_{magnetic}(a), \tag{2.1.8}$$

where

$$F_{beam}(a) = -\frac{1}{m}D\int_0^L (\phi''(s))^2\,ds * a \tag{2.1.9}$$

is the contributing term due to the elasticity of the beam and

$$F_{magnetic}(a) = \frac{1}{m}\left(-\int_0^L T(s,a)(\phi'(s))^2\,ds * a + \int_0^L F_y(s,a)\phi(s)\,ds + \int_0^L C(s,a)\phi'(s)\,ds\right) \tag{2.1.10}$$

is the contributing term due to the presence of the magnetic field.

We can further separate the terms in $F_{magnetic}(a)$ and write them as $F_{magnetic}(a) = F_{moment}(a) + F_{axial}(a) + F_{transverse}(a)$. We define these terms here so that we can make comparisons about their relative magnitudes later on.

$$F_{moment}(a) = \frac{1}{m}\int_0^L C(s,a)\phi'(s)\,ds, \tag{2.1.11a}$$

$$F_{axial}(a) = -\frac{1}{m}\int_0^L T(s,a)(\phi'(s))^2\,ds * a, \tag{2.1.11b}$$

$$F_{transverse}(a) = \frac{1}{m}\int_0^L F_y(s,a)\phi(s)\,ds. \tag{2.1.11c}$$

Going back to equation 2.1.7, if we assume that $V_0 = A_0\,cos(\omega t)$, then we have

$$\ddot{a} = F_{static}(a) + \omega^2 A_0 \int_0^L \phi\,ds\,cos(\omega t). \tag{2.1.12}$$

In our experimental setup, we measure the motion of the beam using readings from a strain gauge attached near the root of the beam. In order to calibrate the strain gauge readings with the displacement of the beam, the most convenient method is to measure a beam tip displacement in the y direction using a caliper and calibrate the corresponding strain gauge reading with that measurement. Thus, it is convenient for us to specify the equations of motion in terms of the beam tip displacement instead of the modal amplitude in order to compare the results from numerical simulations of the model with the experimental results.

Let $v_L(t)$ represent the horizontal displacement of the beam end from its equilibrium position at $y = 0$. Since $v_L(t) = v(L,t) = a(t)\phi(L)$, we have

$$\ddot{v}_L = F_{static}(v_L) + P\,cos(\omega t), \tag{2.1.13}$$

where $P = \omega^2 A_0 \phi(L)\int_0^L \phi\,ds$ and $F_{static}(v_L) = \phi(L)F_{static}(a)$. Adding a term to account for damping gives

$$\ddot{v}_L = F_{static}(v_L) - \delta\dot{v}_L + P\,cos(\omega t). \tag{2.1.14}$$

A linear viscous damping model is used. We assume that the damping coefficient δ captures the effect of damping due to air resistance, small eddy currents induced by magnetic fields (if they are present) and other external sources such as tape attached to the beam. δ can either be calculated from experimental data, or a damping ratio ζ can be stipulated and the corresponding value for δ can be calculated as $\delta = 2\zeta\omega_0$, where $\omega_0 = \sqrt{\frac{D\int_0^L (\phi'')^2\,ds}{m}}$, the natural frequency of the beam without the presence of any magnetic fields [20].

We take equation 2.1.14 as the governing ODE for v_L. We can numerically simulate this equation using three different methods, explained below:

1. Compute $F_{static}(v_L)$ by computing the total magnetic field around the beam. We will refer to this as the **Full Model**. The governing ODE is simulated using by interpolating the computed values of $F_{static}(v_L)$ as the beam moves through the magnetic field and as v_L changes accordingly.

2. Approximate $F_{static}(v_L)$ by a cubic polynomial to give Duffing's equation:

$$\ddot{v}_L = \alpha v_L - \beta v_L^3 - \delta \dot{v}_L + P\,cos(\omega t), \tag{2.1.15}$$

   where α and β can be determined either by:

   (a) Fitting a cubic to the computed $F_{static}(v_L)$. We will refer to this as the **Computational Cubic Approximation**.

   (b) Calculating them from the experimental data: $\alpha = \frac{\omega_1^2}{2}$ and $\beta = \frac{\omega_1^2}{2a_0^2}$, where ω_1 is the natural frequency of the beam about one of the buckled horizontal beam tip positions a_0. (For derivation, see section 4.2.1) We will refer to this as the **Experimental Cubic Approximation**.

These different methods have their own advantages and disadvantages. The full model (method 1) provides the most accurate picture of the vector field governing the dynamics of the system as it makes no approximations about the nature of the magnetic forces. However, $F_{static}(v_L)$ is defined numerically and hence not as easy to examine analytically. The computational cubic approximation (method 2a) is not as accurate as method 1, but is a good approximation for small beam tip deflections (this will be explored later on). More importantly, the cubic approximation gives Duffing's equation, the dynamics of which have been analysed extensively [3]. Furthermore, coefficients of the cubic approximation, α and β, allow us to compare the magnitude of the linear forces (elastic and magnetic) with that of the non-linear component of the magnetic forces. They also allow us to compare our experimental data (method 2b) to the theoretical model (method 2a), as it is not easy to measure the force distributions on the beam tip experimentally, but it is easier to measure the buckled beam position about one of the magnets as well as the natural frequency about that position, and therefore calculate α and β.

2.2 Computation of restoring forces

We now seek to calculate

$$
\begin{aligned}
F_{static}(v_L) = &-\frac{1}{m}\left[\int_0^L T(s,v_L)(\phi'(s))^2\,ds + D\int_0^L (\phi''(s))^2\,ds\right] v_L \\
&+ \frac{\phi(L)}{m}\int_0^L F_y(s,v_L)\phi(s)\,ds + \frac{1}{m}\int_0^L C(s,v_L)\phi'(s)\,ds.
\end{aligned}
\tag{2.2.1}
$$

Since the analytic form of $\phi(s)$ and its derivatives are easily obtained from equations 2.1.3a, 2.1.3b and 2.1.3c , the integral of quantities related to $\phi(s)$ and its derivatives can be obtained either analytically or via numerical integration. We obtain those quantities via numerical integration using a trapezoidal rule [18].

The quantities that are more complicated to calculate are those related to the magnetic field, which are $F_x(s,v_L), F_y(s,v_L)$ and $C(s,v_L)$. Intuitively, they should depend on two main factors : The magnetic field, and the shape of the beam in the magnetic field. The goal is to be able to compute these quantities based on experimental setup parameters. In terms of experimental setup parameters, the magnetic field depends on the field strengths of the magnets, the shape of the magnets, and the distance between the two magnets. The shape of the beam depends on the dimensions of the beam, the offset position of the beam relative to the two magnets, and also the beam mode $\phi(s)$ and the beam tip displacement v_L.

The key point is that we can compute the magnetic field at any given point numerically. If we model the cylindrical magnets as ideal solenoids, then from Derby [6] we can calculate the magnetic field due to an ideal solenoid using a computationally efficient algorithm for the generalized complete elliptic integral in the expression for the magnetic field of the solenoid. The evaluation contains a term that depends on nI, where n is the number of turns of the solenoid and I is the current through the solenoid. Since we are using cylindrical magnets, we can calculate the parameter nI based on the magnetic field strength at the surface of the magnet along the center axis, which is provided by the supplier. That is, if $B_{surface}$ is the magnetic field strength at the surface along the center axis of a cylindrical magnet with radius r and height $2h$, then

$$
nI = \frac{\sqrt{4h^2+r^2}}{h}\frac{B_{surface}}{\mu_0}. \tag{2.2.2}
$$

At any given point on the beam, if we know the Magnetic Field **B** due to the magnets (with components B_x and B_y in the x and y directions respectively), then we can calculate the magnetic forces **F** (per unit length) as [9][10]

$$\mathbf{F} = \mathbf{M} \cdot \nabla \mathbf{B}, \tag{2.2.3a}$$

or

$$\begin{pmatrix} F_x \\ F_y \end{pmatrix} = \begin{pmatrix} M_x \\ M_y \end{pmatrix} \cdot \begin{pmatrix} \frac{\partial B_x}{\partial x} & \frac{\partial B_x}{\partial y} \\ \frac{\partial B_y}{\partial x} & \frac{\partial B_y}{\partial y} \end{pmatrix} = \begin{pmatrix} M_x \frac{\partial B_x}{\partial x} + M_y \frac{\partial B_x}{\partial y} \\ M_x \frac{\partial B_y}{\partial x} + M_y \frac{\partial B_y}{\partial y} \end{pmatrix}. \tag{2.2.3b}$$

where **M** is the magnetization per unit length of the beam due to the magnetic field, and all quantities are functions of s and v_L. Here, we are neglecting the magnetic field produced by the magnetization of the steel beam itself.

The moment per unit length **C** is also given as

$$\mathbf{C} = \mathbf{M} \times \mathbf{B}. \tag{2.2.4}$$

If we assume that:

1. magnetic self-forces on the beam are neglected,
2. magnetic hysteresis is neglected,
3. the dependence of beam magnetization on curvature is small,
4. locally, the magnetic field can be treated as uniform,
5. the beam has uniform cross-section along its length,

then the magnetization **M** can be written as (See appendix C for derivation.)

$$\begin{pmatrix} M_x \\ M_y \end{pmatrix} = \frac{\chi A}{\mu_0 \mu_r} \begin{pmatrix} (1 + \chi cos^2(\theta))B_x + \chi cos(\theta) sin(\theta) B_y \\ \chi cos(\theta) sin(\theta) B_x + (1 + \chi sin^2(\theta)) B_y \end{pmatrix}, \tag{2.2.5}$$

where θ is the angle of the point of the beam relative to the x-axis and A is the cross-sectional area of the beam. χ is the volumetric magnetic susceptibility of the beam material (We take $\chi \approx 10^3$ [30]), $\mu_r = \chi + 1$ is the relative magnetic permeability and μ_0 is the magnetic constant, $\mu_0 = 4\pi * 10^{-7} \frac{Vs}{mA}$.

Furthermore, substituting equation 2.2.5 into equation 2.2.4 allows us to write the magnitude of the moment per unit length as

$$C = \frac{\chi^2 A}{2\mu_0 \mu_r}\left[2B_x B_y\, cos(2\theta) - (B_x^2 - B_y^2)\, sin(2\theta)\right]. \tag{2.2.6}$$

We use the approximation $\theta(s, v_L) \approx v_L(t)\phi'(s)$. Furthermore, we calculate the spatial derivatives of the magnetic field ($\frac{\partial B_x}{\partial x}$, $\frac{\partial B_x}{\partial y}$ etc.) for a given point numerically using a 4^{th}-order central finite difference [18] of the magnetic field, which requires us to evaluate the magnetic field at points near the point on the beam. The distance between these points is chosen to be very small, on the order of 10^{-11} m, relative to an experimental length scale of 10^{-1} m.

Hence, for any given point on the beam, we can calculate the magnetic field (B_x, B_y) at that point (and at nearby points) due to the magnets, and thus calculate F_x, F_y and C. Note that if we specify a beam tip displacement v_L, then we in turn already specify a beam shape since we are using the single-mode approximation.

We can thus compute each term in equation 2.2.1 as follows:

1. Partition an interval in which the beam tip displacement v_L lies over into a finite number of points. A grid of 10000 points is usually chosen over an interval between the magnet centers. Experimentally, this corresponds to a grid size on the order of 10^{-6} m.

2. Partition the beam length $[0, L]$ into a finite number of points. A density of 1000 points is usually used. Each point represents a node on the beam, with arc-coordinate $s \in [0, L]$. Experimentally, this corresponds to a grid size on the order of 10^{-4} m.

3. Calculate $\int_0^L (\phi''(s))^2\, ds$ and $\int_0^L \phi(s)\, ds$ using a trapezoidal rule.

4. $F_{static}(v_L)$ is then computed according to the pseudocode given below:

```
For each beam tip displacement $v_L$
    For each node $s$
        - Calculate the node displacement $v(s) = \frac{\phi(s)}{\phi(L)} v_L$ and angle $\theta = \frac{\phi'(s)}{\phi(L)} v_L$.
        - For the displaced node at location $(s, v(s))$,
          calculate the magnetic field $(B_x, B_y)$ and hence $F_x$, $F_y$ and $C$ as given above.
        - Evaluate $\phi(s)$, $(\phi'(s))^2$ and $(\phi''(s))^2$.
    End
    - Evaluate the integrals in equations 2.1.11a, 2.1.11b and 2.1.11c
```

```
        using a trapezoidal rule.
      - Calculate $F_{static}(v_L)$ by summing the previously computed integrals.
  End
```

We thus have computed $F_{static}(v_L)$ over the interval initially chosen for v_L based on physical parameters. This now allows us to simulate equation 2.1.14 numerically (this is the full model). The actual code used is presented in appendix F.

Chapter 3

Experimental Setup

In this chapter the details of the experimental setup are discussed. We present the physical parameters of the apparatus as well as the electronic circuit that is used to collect and process the strain gauge signal.

3.1 Mainframe, shaker and instrumentation

The experimental setup is shown figure 3.1.

The mainframe is constructed out of hard white maple wood 0.5 inches thick, with the wood pieces joined using three wood screws per connection. The wooden pieces are oriented such that the grains are along the longitudinal direction of the mainframe to provide maximum resistance against bending/flexure of the mainframe due to the forcing from the shaker. The mainframe occupies a volume of 8.73 cm x 7.63 cm x 15.29 cm (all ± 0.01 cm).

A steel strip of 1018 steel 0.9 ± 0.2 mm thick, 8.742 ± 0.005 cm long and 3.04 ± 0.01 cm wide is glued to top surface of the bottom part of the mainframe (henceforth referred to as "base") to provide an attachment surface for the magnets. A thin steel strip of 1095 steel (blue tempered spring steel) with thickness $\triangle$ =0.25 ± 0.02 mm and width w =0.95 ± 0.05 cm serves as the beam to be cantilevered from the top of the mainframe. The steel of the beam is chosen for its high yield strength (552 MPa), since it is important that the beam does not undergo plastic deformation under the magnetic and elastic forces. The Young's Modulus of the steel is $E = 2.06 * 10^5$ MPa, and the density ρ is 7.83 ± 0.02 g cm^{-3}. Two wood screws are used to cantilever the beam against the mainframe using another piece of wood. The length of the cantilevered beam, L = 10.88 ± 0.05 cm. The vertical distance from the base to the cantilever point is 12.80 ± 0.03 cm, thus the distance from the beam

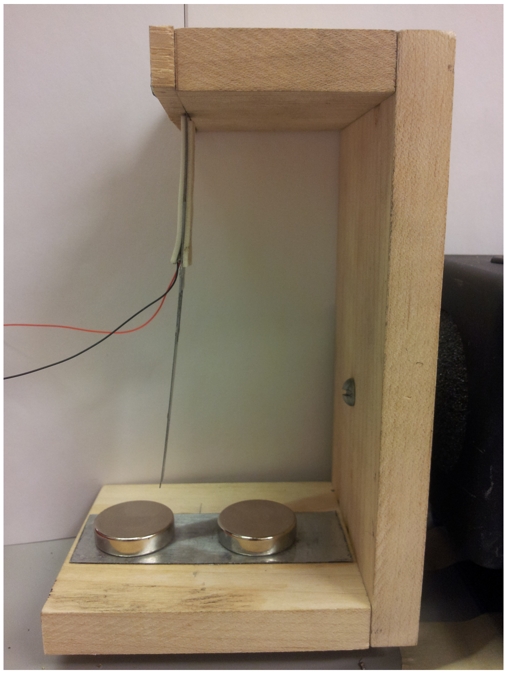

Figure 3.1: Experimental setup.

tip to the base of the mainframe in the is 1.92 ± 0.05 cm.

Two cylindrical magnets each with radius r = 0.5 inches and height h =0.25 inches are used. The magnets each have a magnetic surface field strength of $B_{surface} = 0.21$ Tesla. We ensure that the polarities of the face-up sides of the magnets are the same when they are attached to the steel strip described in the previous paragraph. It is worth noting that there is a non-zero minimum separation distance between the magnets that can be achieved due to the repelling magnetic forces between the magnets. This separation distance can be decreased by roughening up the surface of the steel strip using sandpaper. In our case the minimum distance between magnet centers is 3.74 ± 0.01 cm.

A hole is drilled through the side of the mainframe to serve as a connection point to the shaker. The position of the hole is such that its axis passes through the vertical and lateral component of the center of mass of the mainframe so that undesired vibration modes in the mainframe from the shaker are minimized. In order to do this, the mainframe and the magnets are modelled in Creo Pro/Engineer, and the center of mass is computed from the model. We measure that the largest deviation from the computed center of mass is roughly 1 mm. See figure 3.2 for an illustration of the setup dimensions. Pictures of the Pro/E model and the computed mass properties are given in appendix D.

The mainframe is fastened against the shaker using a machine screw. We make sure that the mainframe is upright and not tilted sideways during the fastening process. See figure 3.3

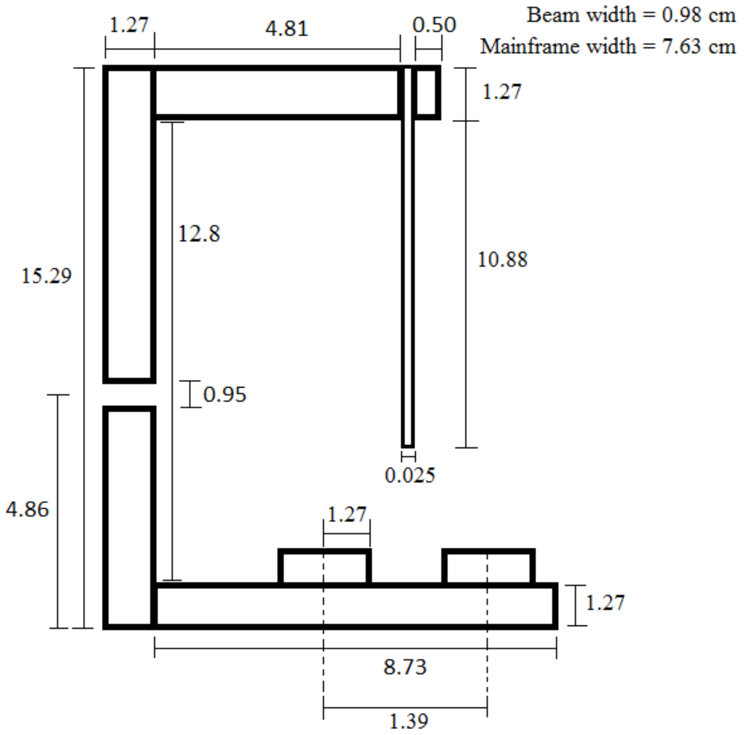

Figure 3.2: 2-D Cross section of setup with dimensions in given in cm. Figure not drawn to scale.

for a picture of the mainframe with the shaker.

The shaker is a K2007E01 SmartShaker electromagnetic shaker (The Modal Shop, Cincinnati OH) that contains an integrated amplifier. An Agilent 33220A signal generator (Agilent Technologies, Santa Clara CA) is used to supply the driving signal to the shaker. The driving signal is always sinusoidal, and the frequency and peak-to-peak voltage are varied. The driving signal from the signal generator is viewed in an oscilloscope to ensure that the signal is as desired before connecting the signal generator to the shaker. In order to secure the shaker so that it does not move due to the vibration, the bottom of the shaker is also taped to the surface that it is resting on. We assume that the connection of the mainframe to the shaker is secure enough, and that the mainframe is rigid enough so that the motion of the shaker translates to the same motion of the mainframe. We also assume that the forcing frequency and amplitude from the shaker are the same as that of the driving signal to the shaker from the signal generator.

In order to increase the damping of the system, strips of Scotch tape 3.92 ± 0.01 cm long, 0.96 ± 0.01 cm wide and 1.5 ± 0.2 mm thick are attached to both sides of the beam near the root of the beam (close to the cantilever point).

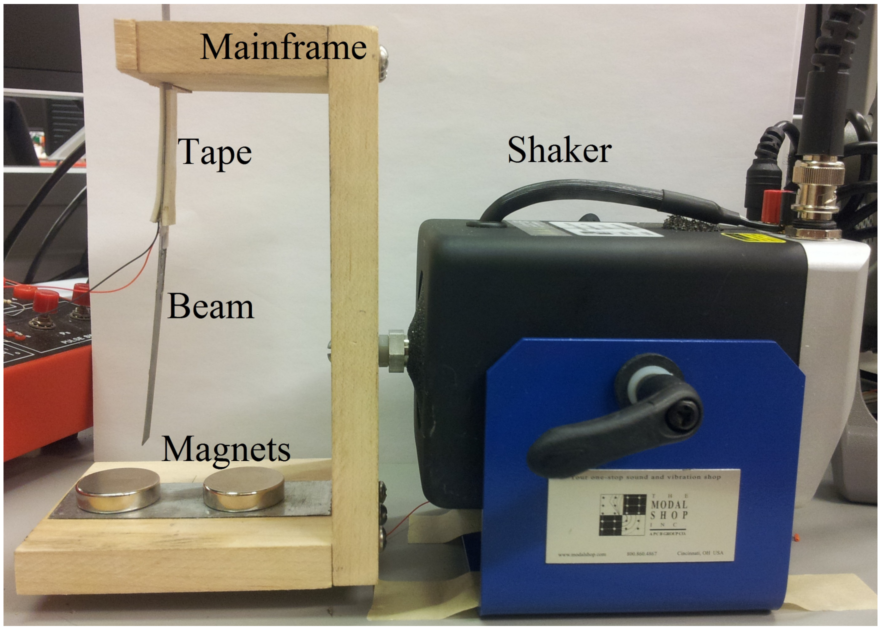

Figure 3.3: Experimental setup of mainframe attached to shaker. Also noticeable are the magnets and also the strips of tape attached to the root of the beam

3.2 Data collection

A strain gauge is attached using a Loctite 401 adhesive near the root of the beam. We use an SGD-7/350-LY11 Omega strain gauge (Omega, Stamford CT) with a 350 Ω resistance and gauge factor of 2.13. The strain gauge is chosen such that the design contact surface is that of steel. We construct an electronic circuit on a breadboard to process the analog signal from the strain gauge. The constructed circuit is described as follows:

The leads from the strain gauge are soldered to thin wire, which are then connected to a Wheatstone quarter-bridge circuit that is temperature-compensated. The temperature compensation is achieved by attaching another strain gauge to the Wheatstone bridge that is in a similar setup to the experimental conditions of the first strain gauge.

The signal from the Wheatstone bridge is then connected to a AD623 Instrumentation Amplifier (Analog Devices, Norwood MA) to obtain an amplification of the signal by a factor of 260, since the change in the output signal of the Wheatstone bridge is very low due to the low change in resistance of the strain change in response to strain. (change of 0.7 Ω per millistrain). A potentiometer connected to a positive voltage at one end and to the reference input of the AD623 at the other allows us to calibrate the output signal so that the output signal is at an appropriate voltage value when the beam tip displacement is zero. The output signal from the amplifier is thus treated as a signal that is proportional to the beam tip displacement. Furthermore, this output signal is also connected to an op-amp differentiator circuit, allowing us to measure the velocity of the beam tip as well. For the schematic of the circuit used, please refer to appendix E

The output signals from both the amplifier (representing position) and differentiator (representing velocity) are connected to an Arduino Uno (Arduino, Adafruit Industries, Varick St NY). The Arduino is a single-board microcontroller, which has an on-board 10-bit Analog-to-Digital converter (ADC), an 8-bit ATmega328 microcontroller, as well as a USB port. Using the Arduino interface, we program the Arduino to read in both position and velocity signals that have been digitized by the ADC and send them over a serial port at a transmission rate of 115200 baud via USB. The data sent over the serial connection via USB to a laptop is read in using Matlab. A mean sampling rate of 620 ± 20 Hz was achieved, or 1 measurement every 1.61 ± 0.05 ms. There is an uncertainty of ± 5 digital units in position and an uncertainty of ± 10 digital units in velocity due to electrical noise. The digital range of both the position and velocity as sampled from the 10-bit ADC is $2^{10} = 1024$ digital units.

To determine the beam tip displacement corresponding to a digital unit, the distance between the buckled beam tip positions is measured using a caliper, and the corresponding digital readings for each beam tip position are also recorded. The displacement per digital unit is obtained by dividing this measured distance by the difference in digital readings

Chapter 4

Results and Discussion I

In this chapter we focus on results obtained in the case where no forcing from the shaker is present. We first discuss the results obtained from free vibrations where no magnets are present, where the main purpose is to check that experimental results agree with classic Euler-Bernoulli beam theory, and also to calculate the damping ratio ζ and obtain the damping coefficient δ from there. We then discuss the case of free vibrations where magnets are present but without forcing from the shaker. We first present the relevant theory for the Duffing oscillator, and then compare the experimental results with the computational model in terms of buckled beam positions, natural frequencies and basins of attraction. We then present an analysis of the bifurcations of the system as various physical parameters are varied based on numerical simulations of the full model.

4.1 Free vibrations without magnets

In the absence of a magnetic field, all quantities related to the magnetic field are equal to zero. Thus, F_x, F_y and C in equation 2.1.1 are equal to zero. If we have no forcing from the shaker, then the partial differential equation for the system (without damping) is $-Dv'''' = m\ddot{v}$, which is the classical Euler-Bernoulli equation [20] with no external loads. If we assume a single-mode approximation, equation 2.2.1 gives

$$F_{static}(v_L) = -\frac{D\int_0^L (\phi''(s))^2\, ds}{m} v_L, \tag{4.1.1}$$

and thus, from equation 2.1.14, the governing ODE for the system is

$$\ddot{v_L} = -\frac{D\int_0^L (\phi''(s))^2\, ds}{m} v_L - \delta \dot{v_L}. \tag{4.1.2}$$

Equation 4.1.2 for the beam tip displacement v_L is the equation for a damped harmonic oscillator. The (undamped) natural frequency is

$$\omega_0 = \sqrt{\frac{D\int_0^L (\phi'')^2\, ds}{m}}. \tag{4.1.3}$$

The damping ratio is $\zeta = \frac{\delta}{2mD\int_0^L (\phi''(s))^2\, ds}$, and the damped frequency is given as $\omega_d = \omega_0\sqrt{1-\zeta^2}$ [21].

In our case the system is under-damped ($\zeta < 1$), and the solution to equation 4.1.2 is given as $v_L(t) = e^{-\zeta\omega_0 t}[Acos(\omega_d t) + Bsin(\omega_d t)]$, where A and B are constants dependent upon the initial conditions $v_L(0)$ and $\dot{v}_L(0)$ [22]. Thus, fitting an exponential curve to the amplitude envelope of the beam tip displacement over a time series will give the exponential constant $\zeta\omega_0$, and performing a Fast Fourier Transform (FFT) on the time series will give the damped frequency ω_d. We can solve for ζ and calculate δ accordingly for the computational model. In the proceeding calculations we express frequencies in Hertz rather than in radians per second, and so we use the symbol f in place of ω for all quantities involving frequencies, with the conversion $f = 2\pi\omega$.

The beam is displaced and released, and the experimental time series is recorded. The time series and the exponential fit is shown in figure 4.1. From the exponential fit, we obtain $\zeta\omega_0 = 3.10 \pm 0.05$. From the Fourier transform of the experimental time series, we get that $f_d = 17.6 \pm 0.5$ Hz. Solving for ζ and f_0 gives $\zeta = 0.173 \pm 0.005$ and $f_0 = 17.9 \pm 0.3$ Hz. Correspondingly, $\delta = 6.2 \pm 0.2$.

The theoretical value of f_0, calculated from equation 4.1.3, is 17.81 Hz, which is within the uncertainty bounds of the experimentally-calculated f_0 (and correspondingly the theoretical $f_d = 17.54$ Hz assuming $\zeta = 0.173$). See figure 4.2 for a comparison of the FFT of experimental data with the theoretical value of f_d. The broadness of the FFT curve and the distance between data points is due to the low amount of time available to collect data from the free vibrations before they are damped out.

Using the calculated value of δ and the physical parameters of the experiment such as the beam length, thickness, material etc., we can also numerically simulate equation 4.1.2 and compare the computed results to that of the experimental results. A comparison of the experimental and computational results is shown in figure 4.1. We see that the numerical

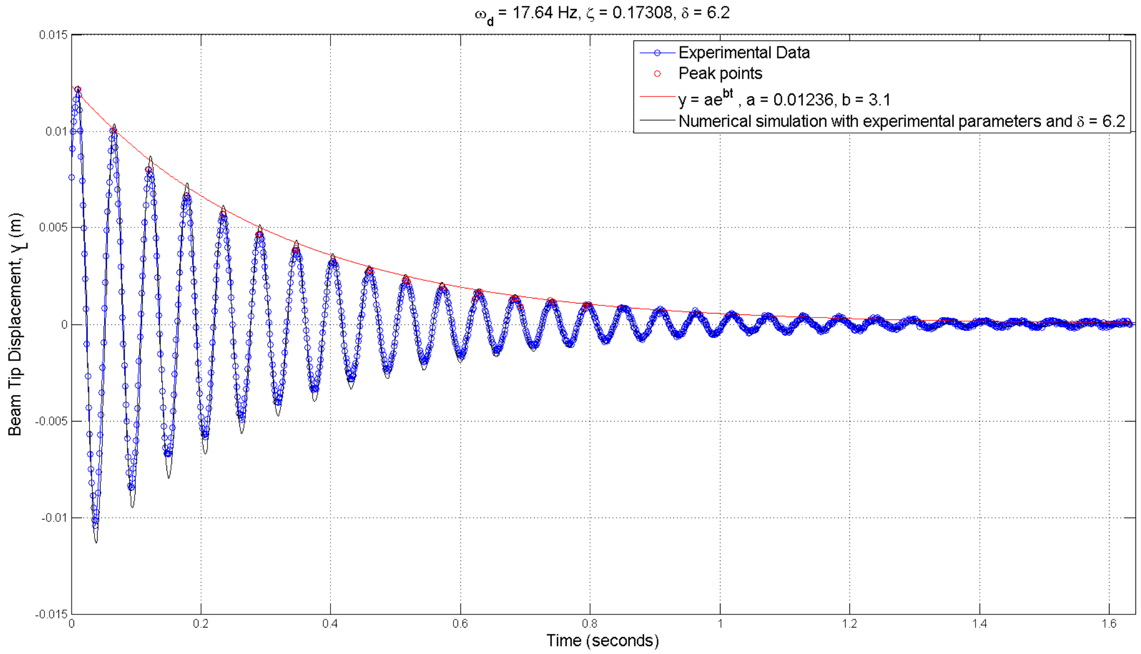

Figure 4.1: Experimental time series, exponential fit and numerical simulation for damped oscillator.

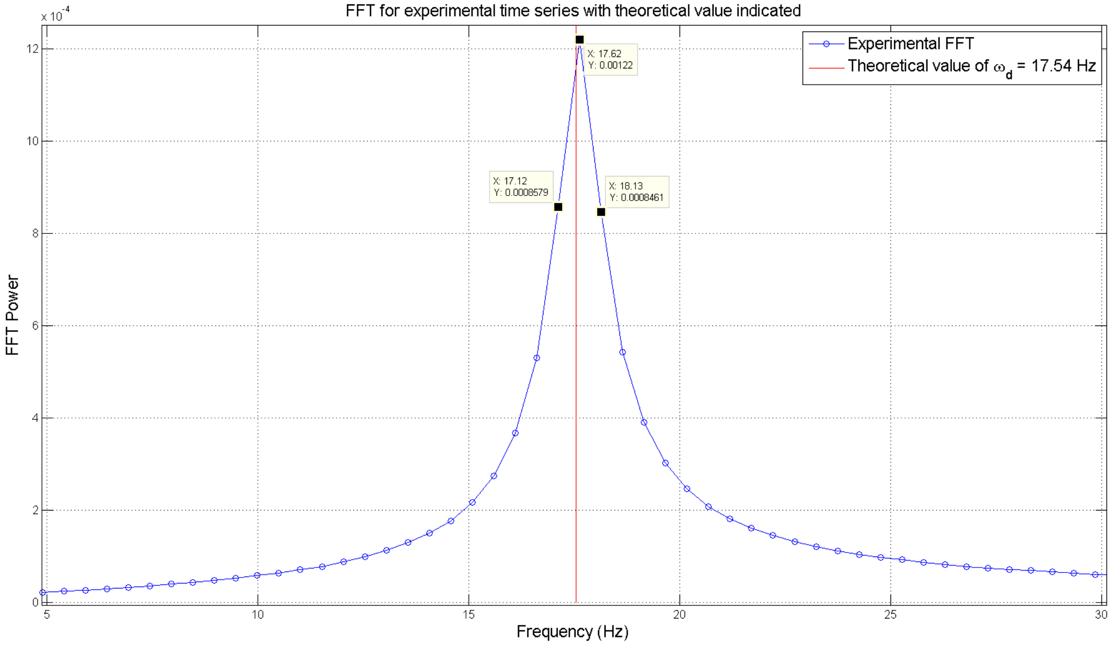

Figure 4.2: Fourier transform of experimental data and theoretical value of ω_d.

simulations using the experimentally-derived value for δ and the experimental parameters gives a good fit to the experimental data.

4.2 Free vibrations with magnets

With no forcing, $A_0 = 0$ (hence $P = 0$), but F_x, F_y and C are non-zero. Thus, we need to consider all the terms in equation 2.2.1.

The governing ODE for the beam tip position presented in equation 2.1.14 can be written as a 2-dimensional system with $v_1 = v_L$ as follows:

$$\begin{aligned} \dot{v_1} &= v_2, \\ \dot{v_2} &= F_{static}(v_1) - \delta v_2. \end{aligned} \tag{4.2.1}$$

The fixed points of this system are $(F_{static}(v_1), 0) = (F_{static}(v_L), 0)$. Thus, the zeros of $F_{static}(v_L)$ specify the fixed points of the system. The Jacobian is given by

$$J = \begin{pmatrix} 0 & 1 \\ \frac{\partial F_{static}}{\partial v_L} & -\delta \end{pmatrix}. \tag{4.2.2}$$

In general we will have $\delta > 0$, and so trace$(J) = -\delta < 0$, and det$(J) =$ -$\frac{\partial F_{static}}{\partial v_L}$. Hence if $\frac{\partial F_{static}}{\partial v_L} < 0$ at a fixed point, then det$(J) > 0$ and the fixed point will be a stable spiral sink node. If $\frac{\partial F_{static}}{\partial v_L} > 0$ at a fixed point, then det$(J) < 0$ and the fixed point will be a saddle [14].

We first introduce the relevant theory for the Duffing oscillator in this case. We then present an example of the computed $F_{static}(v_L)$ and the corresponding computational and experimental cubic approximations for fixed physical experimental parameters. These are the parameters that will be fixed experimentally when we consider non-zero forcing. We will then examine the bifurcations of the system as certain physical parameters such as distance between magnet centers and magnet field strengths are changed.

4.2.1 Theoretical model

The equation for the Duffing oscillator in this case is given as

$$\ddot{v_L} = \alpha v_L - \beta v_L^3 - \delta \dot{v_L}, \tag{4.2.3}$$

or with $v_1 = v_L$,

$$\begin{aligned} \dot{v_1} &= v_2 \\ \dot{v_2} &= \alpha v_1 - \beta v_1^3 - \delta v_2. \end{aligned} \tag{4.2.4}$$

The fixed points are at $(0, 0)$ and at $(\pm a_0, 0) = \left(\pm\sqrt{\frac{\alpha}{\beta}}, 0\right)$, and the Jacobian is given as

$$J = \begin{pmatrix} 0 & 1 \\ \alpha - 3\beta v_1^2 & -\delta \end{pmatrix}. \tag{4.2.5}$$

Hence,

$$J|_{(0,0)} = \begin{pmatrix} 0 & 1 \\ \alpha & -\delta \end{pmatrix}, \tag{4.2.6}$$

meaning that (0,0) is a saddle point since $\det(J) = -\alpha < 0$ (Remember that $\alpha > 0$). Also,

$$J|_{\left(\pm\sqrt{\frac{\alpha}{\beta}},0\right)} = \begin{pmatrix} 0 & 1 \\ -2\alpha & -\delta \end{pmatrix}, \tag{4.2.7}$$

meaning that $\det(J) = 2\alpha > 0$ for the fixed points at $\left(\pm\sqrt{\frac{\alpha}{\beta}}, 0\right)$. They will be stable spiral sink nodes if $\delta > 0$ (since trace(J)< 0) or centers if $\delta = 0$ (since trace(J)$= 0$).

We now linearize about the fixed points $\pm(a_0, 0)$ to find the natural frequency about the buckled positions a_0. We present derivations below for a_0, the procedure for $-a_0$ is similar.

We take $v_L = v_1 = a_0 + \eta$, and substituting this into equation 4.2.3 gives

$$\ddot{\eta} = \alpha a_0 + \alpha\eta - \beta a_0^3 - 3\beta a_0^2\eta + O(\eta^2) - \delta\dot{\eta}. \tag{4.2.8}$$

Since $\alpha a_0 - \beta a_0^3 = 0$, if we ignore terms higher than order 2 in η we get

$$\ddot{\eta} = -(3\beta a_0^2 - \alpha)\eta - \delta\dot{\eta}. \tag{4.2.9}$$

If we define $\omega_1^2 = 3\beta a_0^2 - \alpha$, we obtain

$$\ddot{\eta} = -\omega_1^2\eta - \delta\dot{\eta}. \tag{4.2.10}$$

Thus, we see that the motion of $v_L = v_1$ around the buckled position a_0 is simply that of a damped harmonic oscillator similar to that presented in section 4.1, only that the natural frequency in this case is $\omega_1 = \sqrt{3\beta a_0^2 - \alpha} = \sqrt{3\beta\frac{\alpha}{\beta} - \alpha} = \sqrt{2\alpha}$. Since $a_0 = \sqrt{\frac{\alpha}{\beta}}$ and $\omega_1 = \sqrt{2\alpha}$, we can solve for α and β to get

$$\begin{aligned} \alpha &= \frac{\omega_1^2}{2}, \\ \beta &= \frac{\omega_1^2}{2a_0^2}. \end{aligned} \tag{4.2.11}$$

a_0 is easily measured experimentally, and ω_1 can be obtained from a FFT of the time series of oscillations around the buckled position a_0, if we assume that the damping is small enough that the damped frequency is close to the natural frequency, and that there is no additional damping from the magnetic forces.

4.2.2 Equilibrium buckled positions and natural frequencies

The experimental setup is such that $d = 3.93 \pm 0.02$ cm, where d is the distance between the magnet centers. A plot of the magnitude-normalized magnetic field is shown in figure 4.3. We then present graphs below in figure 4.4 for $F_{moment}(v_L)$, $F_{axial}(v_L)$, $F_{transverse}(v_L)$ and $F_{beam}(v_L)$ which are computed according to the pseudo-code given in section 2.2. We also present a graph comparing $F_{magnetic}(v_L)$ with $F_{beam}(v_L)$ in figure 4.5.

From $F_{static}(v_L)$ for the full model seen in figures 4.4 and 4.5, we see that the computational full model indicates that we will have a double-well potential with an unstable fixed point (saddle) at (0,0) and two stable fixed points (spiral nodes) at (±1.10 cm,0). Taking a cubic approximation for the computed $F_{static}(v_L)$ for small beam tip displacements, we obtain $\alpha = 8.848 \times 10^3$ and $\beta = 8.113 \times 10^7$ for the computational cubic approximation, shown in figure 4.6. Thus, the computational cubic approximation predicts buckled equilibria at $v_L = \sqrt{\frac{\alpha}{\beta}} = \pm 0.0104$ m, and a natural frequency of $f_1 = \frac{\sqrt{2\alpha}}{2\pi} = 21.17$ Hz.

Experimentally, we find that there are two stable equilibrium points, and we measure a buckled beam tip displacement of 1.00 ± 0.02 cm about one side and 0.98 ± 0.02 cm about the other, with respective damped natural frequencies of 24.4 ± 0.1 Hz and 24.1 ± 0.1 Hz. The difference in the displacements and damped natural frequencies reflect the breaking of symmetry due to factors such as imperfect magnet positioning and imperfections in beam shape as a result of manufacturing. Nevertheless, the displacements and frequencies are close enough that we can take the average of the two measurements so that we can compute α and β for the experimental cubic approximation. We calculate an average experimental buckled beam tip displacement $a_0 = 0.99 \pm 0.02$ cm and average natural frequency about the buckled

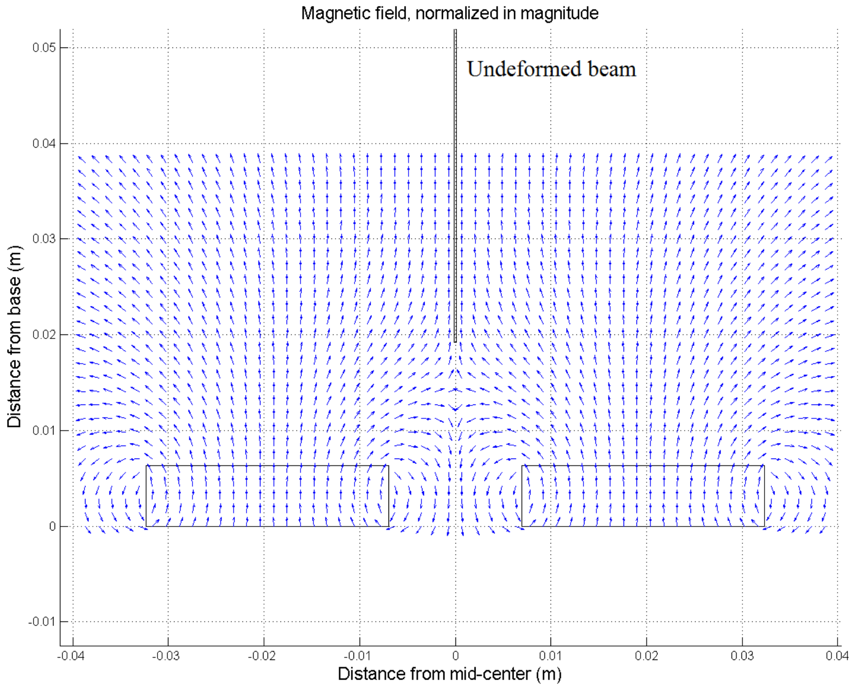

Figure 4.3: Computed magnetic field in experimental setup (normalized in magnitude).

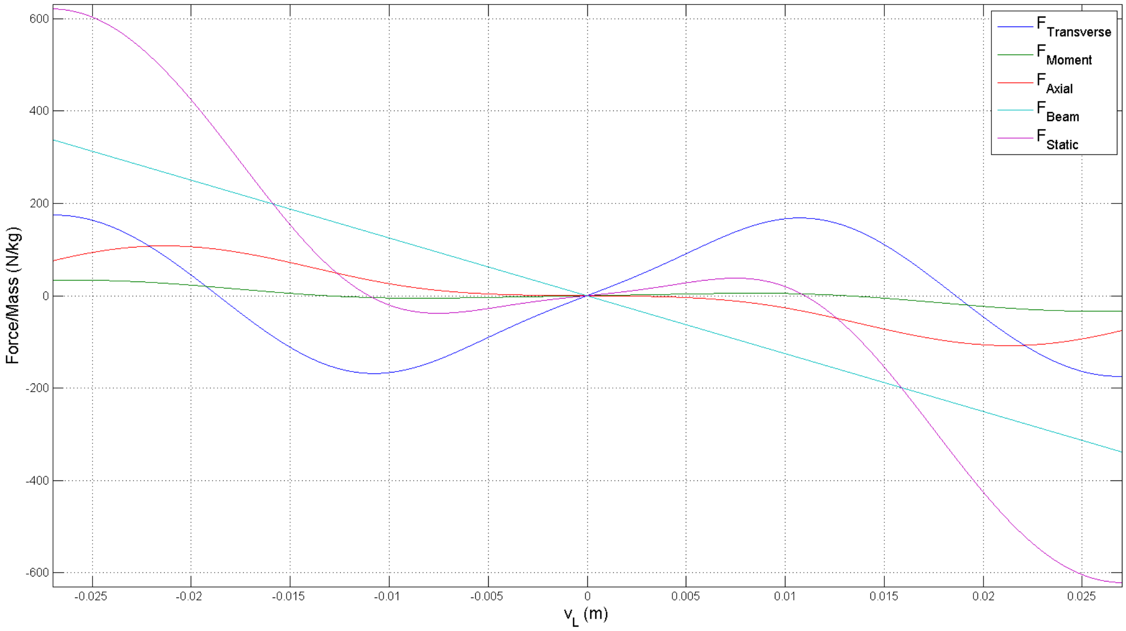

Figure 4.4: Full Model: The separate terms in F_{static} with $d = 3.93$ cm.

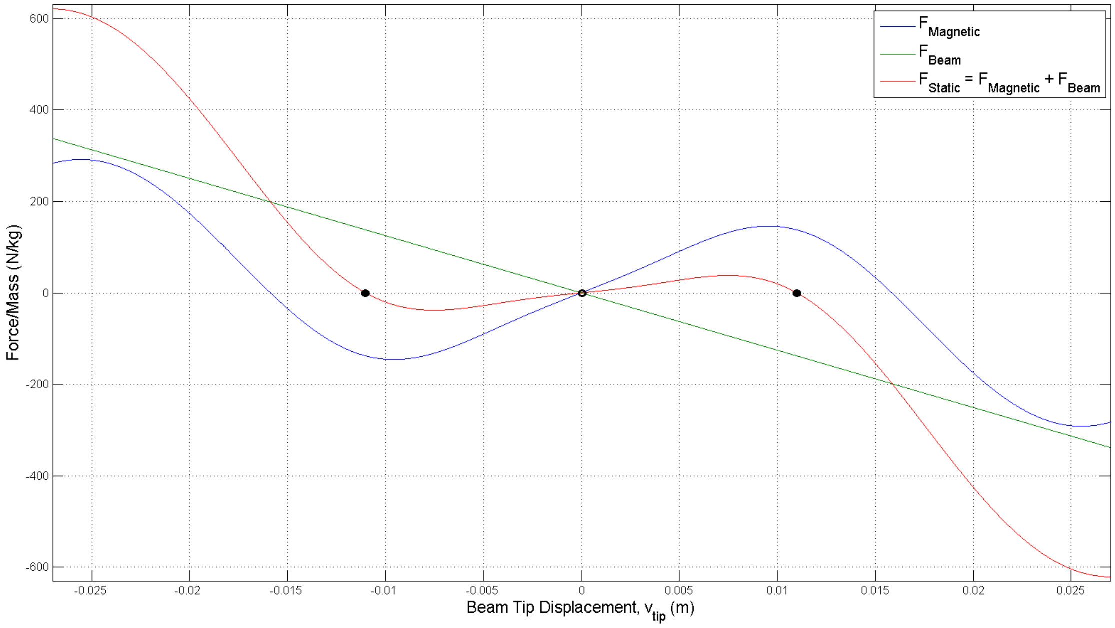

Figure 4.5: Full Model: Contributions of $F_{magnetic}$ and F_{beam} to F_{static} with $d = 3.93$ cm. Stable fixed points indicated as dots, unstable fixed points indicated as circles.

position of $f_1 = 24.3 \pm 0.1$ Hz. Thus, the corresponding parameters for the experimental cubic approximation are $\alpha = 1.161 \times 10^4$ and $\beta = 1.172 \times 10^8$.

We see that α and β as computed from the computational cubic approximation are noticeably different compared to the α and β calculated from experimental measurements. One reason for this is that there is some error in the computational cubic approximation distribution of F_{static} from the full model, especially for smaller displacements. This is seen in figure 4.6. Even though the computational cubic approximation gives a closer prediction of the experimental buckled beam position, the full model gives a better match to the measured natural frequency about the buckled positions (more similar slopes near the fixed points).

From figure 4.6, we see that the full model slightly over-estimates the equilibrium buckled beam tip displacement. Specifically, the full model indicates that the beam tip displacement is 1.100 ± 0.005 cm, overestimating the experimental measurements by about 10%. Furthermore, numerical simulations using the full model give a damped frequency about the equilibrium points of 24.45 ± 0.05 Hz, which within 0.6% to the experimentally measured value. On the other hand, the computational cubic approximation to the full model predicts a buckled beam tip displacement of 1.04 cm (closer to experimental value) and a natural frequency of 21.17 Hz (further from experimental value). Hence, these discrepancies between the full model, its cubic approximation and experimental results lead to the aforementioned differences in α and β.

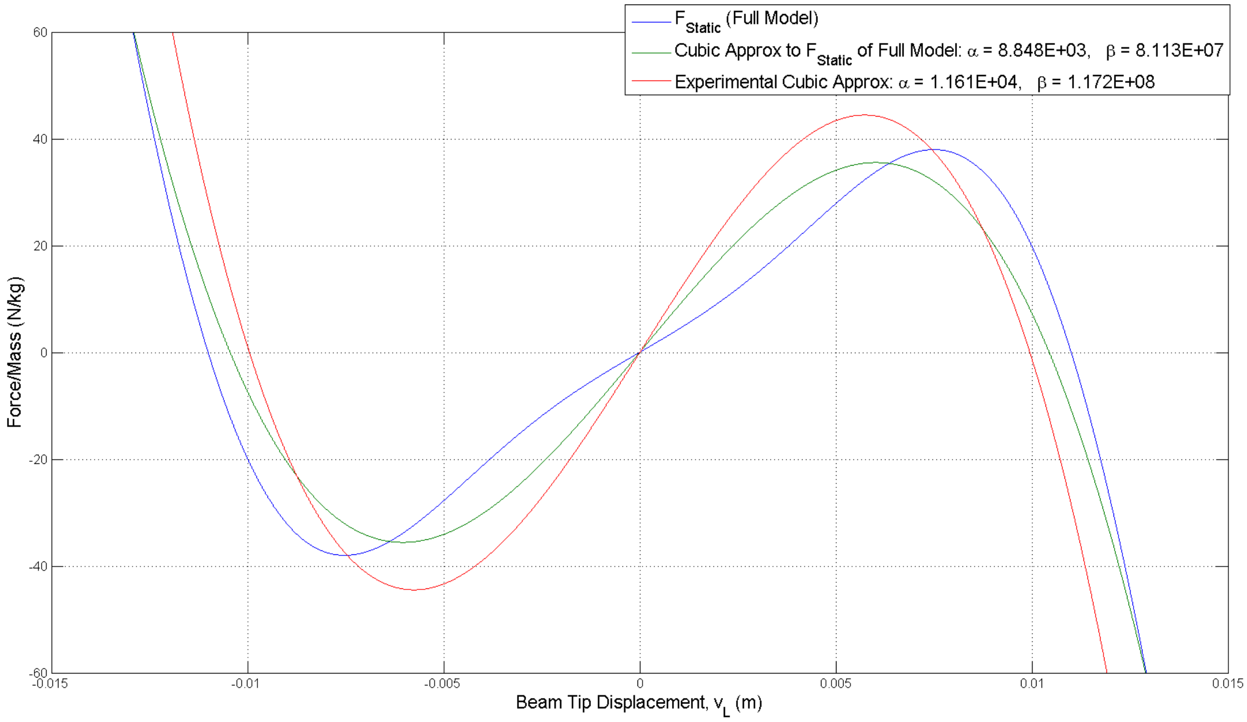

Figure 4.6: Comparison of full model, computational cubic approximation ($\alpha = 8.848 \times 10^3$, $\beta = 8.113 \times 10^7$) and experimental cubic approximation ($\alpha = 1.161 \times 10^4$, $\beta = 1.172 \times 10^8$) for F_{static}.

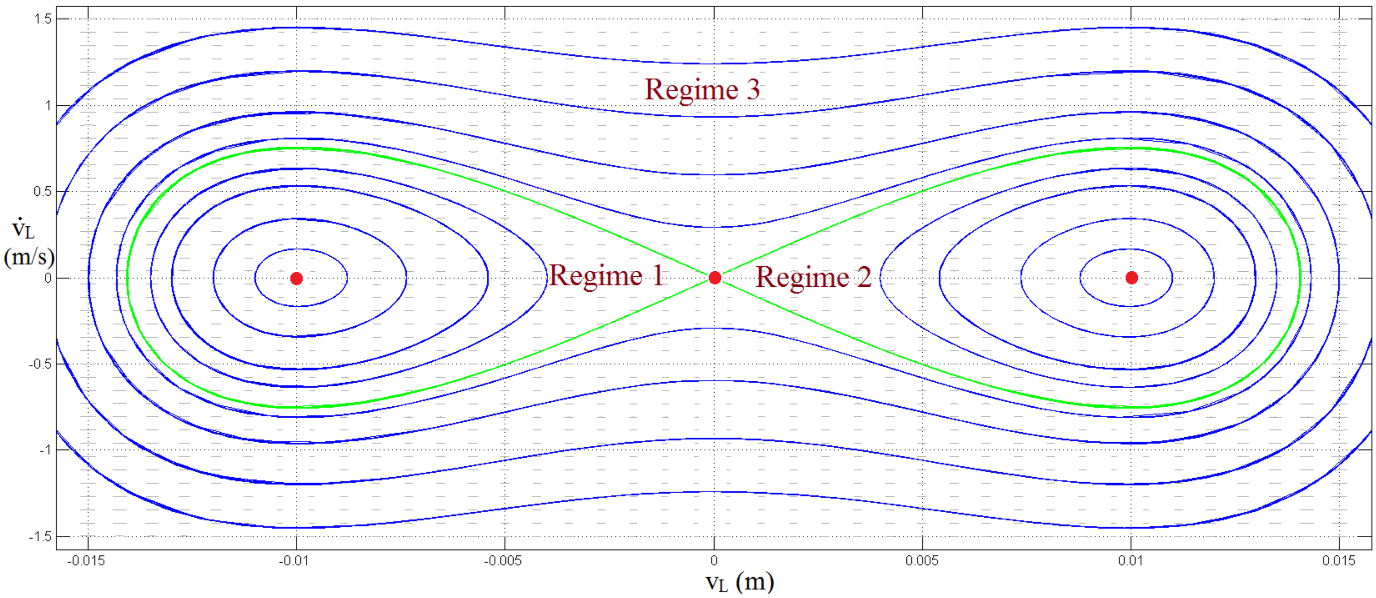

Figure 4.7: Level curves of an undamped Duffing Oscillator using experimental cubic parameters. The homoclinic orbit is highlighted in green, fixed points are indicated as red dots level curves are plotted in blue.

4.2.3 Phase portraits and dynamics

As mentioned in the section 2.2, approximating $F_{static}(v_L)$ using a cubic polynomial yields the equation for Duffing's oscillator, which is equation 2.1.15. The dynamics of the unforced Duffing oscillator are well-understood [14], and some results are repeated here for comparison with the computational model and experimental results.

In the absence of damping ($\delta = 0$), the fixed point at (0,0) is a saddle, and the fixed points at $\left(\pm\sqrt{\frac{\beta}{\alpha}}, 0\right)$ are centers (see section 4.2.1). The equation for the undamped Duffing Oscillator can be integrated to show that it is a Hamiltonian system with total energy $Q(t) = \frac{1}{2}\left(\dot{v_L}^2 - \alpha v_L^2 + \frac{1}{2}\beta v_L^4\right) =$ constant. The energy $Q(t)$ describes a double-well potential over v_L and $\dot{v_L}$, and the corresponding level curves are shown in figure 4.7. The trajectory of any initial condition starting on the level curve stays on the level curve. Thus, an orbit along a level curve represents an orbit of the system for a given energy, and all orbits are periodic except for the two homoclinic orbits to the saddle at (0,0), which is discussed below.

An important orbit to notice is a homoclinic orbit which joins the saddle point to itself. It corresponds to the level curve with energy 0 in figure 4.7, highlighted in green. Formally, a trajectory on such an orbit approaches the saddle point as $t \to \pm\infty$. Thus, such a homoclinic orbit lies in the intersection of the stable and unstable manifolds of an equilibrium [2], and these manifolds will be important in explaining chaotic behaviour of the system when periodic

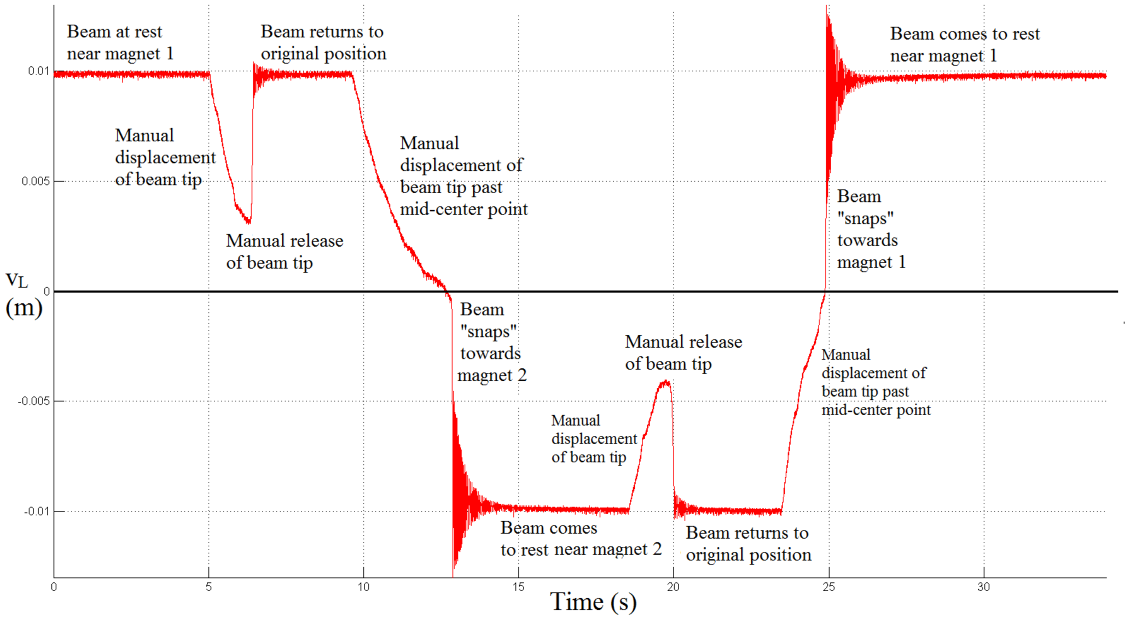

Figure 4.8: Manual displacement of beam tip to investigate fixed points of system.

forcing is introduced. For now, it suffices to notice that the homoclinic orbit of the saddle point separates the phase plane into 3 different regimes with two possible behaviors : There are small periodic oscillations that go back and forth about the two stable fixed points (regimes 1 and 2 with negative energy in figure 4.7), and there are large periodic oscillations that go back and forth encircling both stable fixed points (regime 3 with positive energy in figure 4.7).

We now consider non-zero damping. The fixed point at (0,0) is still a saddle, but the two fixed points at $\left(\pm\sqrt{\frac{\beta}{\alpha}}, 0\right)$ are now stable spiral nodes, as analyzed in section 4.2.1. We see from the full model in this case that there are also three fixed points, a saddle at (0,0) and two stable nodes at $(\pm v_L^*, 0)$, where $F_{static}(v_L^*) = 0$. The two stable fixed points are observed experimentally as seen from measurements for the equilibrium buckled beam tip positions.

The unstable saddle point can be observed experimentally where the beam tip tends towards one of the equilibrium points as it is pushed away from that point, but then suddenly snaps towards the other equilibrium point as it is pushed past the unstable equilibrium. See figure 4.8 for observations of this phenomenon.

Non-zero damping also implies that there is energy dissipation in the system. It can be shown that $\frac{dQ(t)}{dt} = -\delta \dot{v_L}^2 \leq 0$ [14], and thus all trajectories are such that the energy decreases until v_L converges to one of the fixed points of the system where $\dot{v_L} = 0$. This can be illustrated by considering the basin of attraction for the fixed points of the system, shown in figure 4.9 for the experimental cubic approximation.

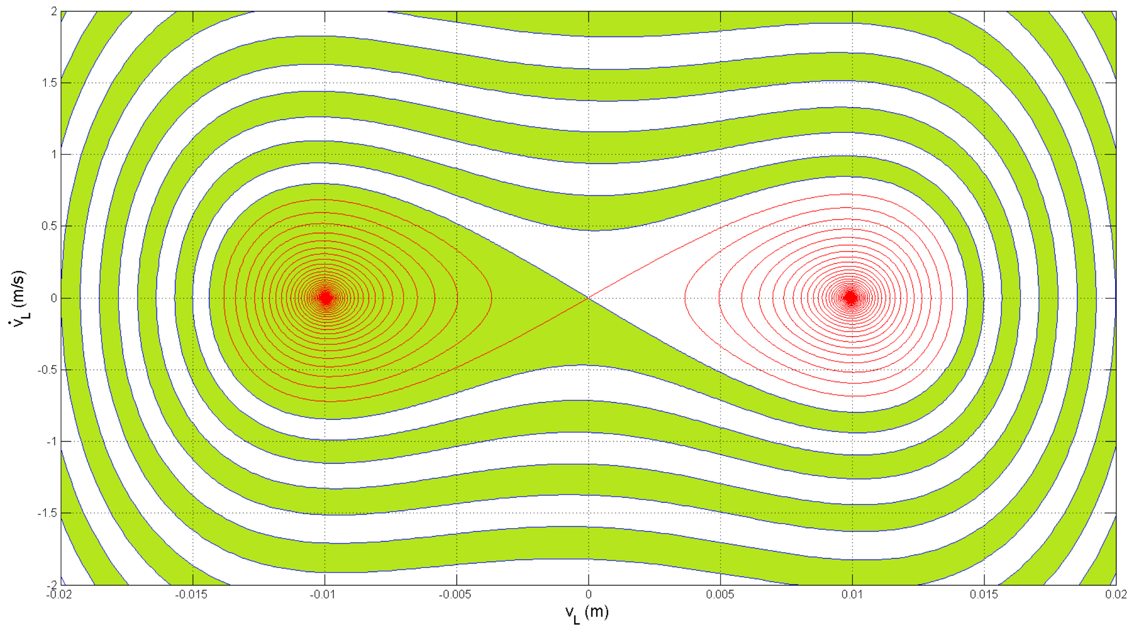

Figure 4.9: Experimental cubic approximation: basin of attraction for fixed points (± 0.99 cm, 0) shown in white and green respectively. Stable manifold of saddle shown in blue, unstable manifold of saddle shown in red.

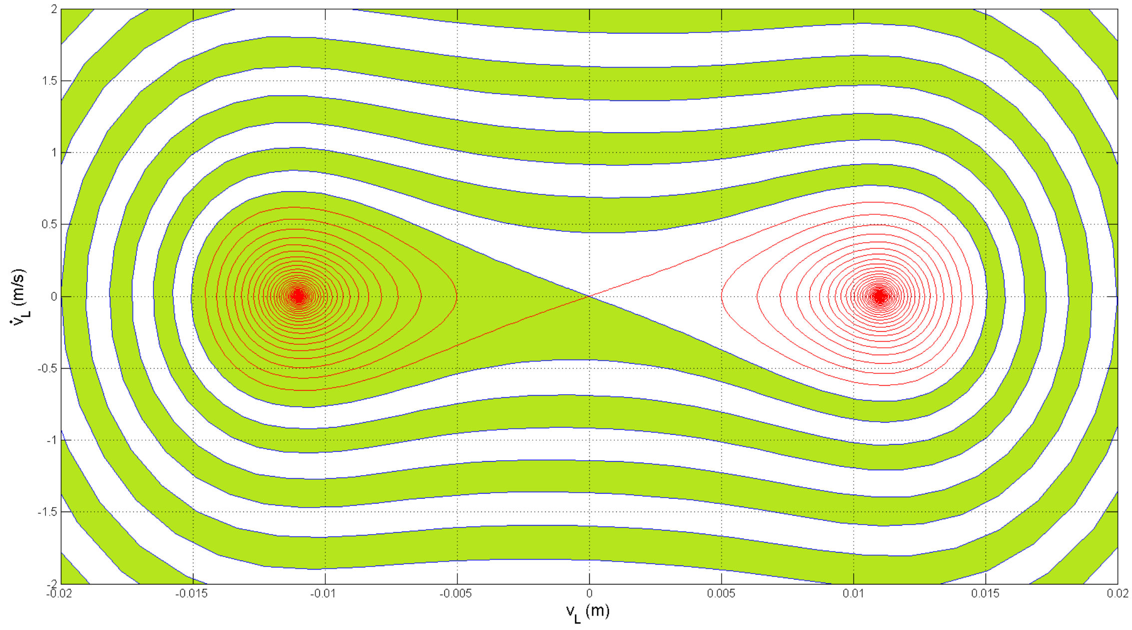

Figure 4.10: Full model: Basin of attraction for fixed points (± 1.1 cm, 0) shown in white and green respectively. Stable manifold of saddle shown in blue, unstable manifold of saddle shown in red.

We see that with damping, the homoclinic orbit is 'broken' and the stable and unstable manifolds of the saddle point are separated. The unstable manifolds of the saddle point spiral into the stable fixed points, whereas the stable manifolds of the saddle point extend out to the whole phase plane, separating the basins of attraction of the two stable fixed points. Thus, the stable and unstable manifolds of the saddle point determine the global behaviour of the system. The basin of attraction for the saddle point is a curve (the stable manifold of the saddle), whereas the basin of attraction of the two stable fixed points are areas separated by that curve.

We also observe such behaviour in the full computational model. The orbits observed in numerical simulations involving the full model are similar to that those of the Duffing oscillator, with similar shapes for the basins of attraction, as seen in figure 4.10.

An important consideration in thinking about this similarity is that both the full model and the cubic approximation possess a saddle in between two stable spirals, and that these are the only fixed points for both systems. Thus, the linearization of $F_{static}(v_L)$ near these fixed points for both the full model and the cubic approximation are necessarily isomorphic to each other [2]. A related idea is that the general shape of $F_{static}(v_L)$ for the full model is similar to that of the cubic approximation over v_L for moderate displacements, which can be seen in figure 4.6. For larger displacements, the cubic approximation increases in magnitude faster than the full model (cubic vs linear). The experimental cubic approximation is replotted in figure 4.11 over a larger range of v_L. However, this is not important since energy dissipation due to damping means that the all trajectories still have to go to fixed points of the system as $t \to \infty$ regardless whether $F_{static}(v_L)$ is modelled by the full model or by the cubic approximation, and the fixed points of the system are well-approximated by the cubic, meaning we expect the behaviour of the orbits for the full model to be similar to that of the Duffing oscillator, at least for moderate displacements.

The structure of the basin of attraction can also be observed experimentally. If we displace the beam tip outwards slightly from one of the fixed points and release it, the trajectory is such that the beam tip should return to the same fixed point. However, for larger displacements, the trajectory is such that the beam tip will end up at the other fixed point, and for even larger displacements the beam tip will end up at the fixed point on the same side and so on. This is seen in figures 4.12 and 4.13, where the trajectories of the orbits follow the structure of the basin of attraction presented in figures 4.9 and 4.10. We note that the uncertainty in the digital readings caused by electrical noise (as mentioned in section 3.2) results in 'noisy' plots of the orbits on the phase plane as taken from experimental data. We generally see a large-scale component of the noise when the beam is in motion, as well as a small-scale component of the noise when the beam is at rest. Although the orbit trajectories

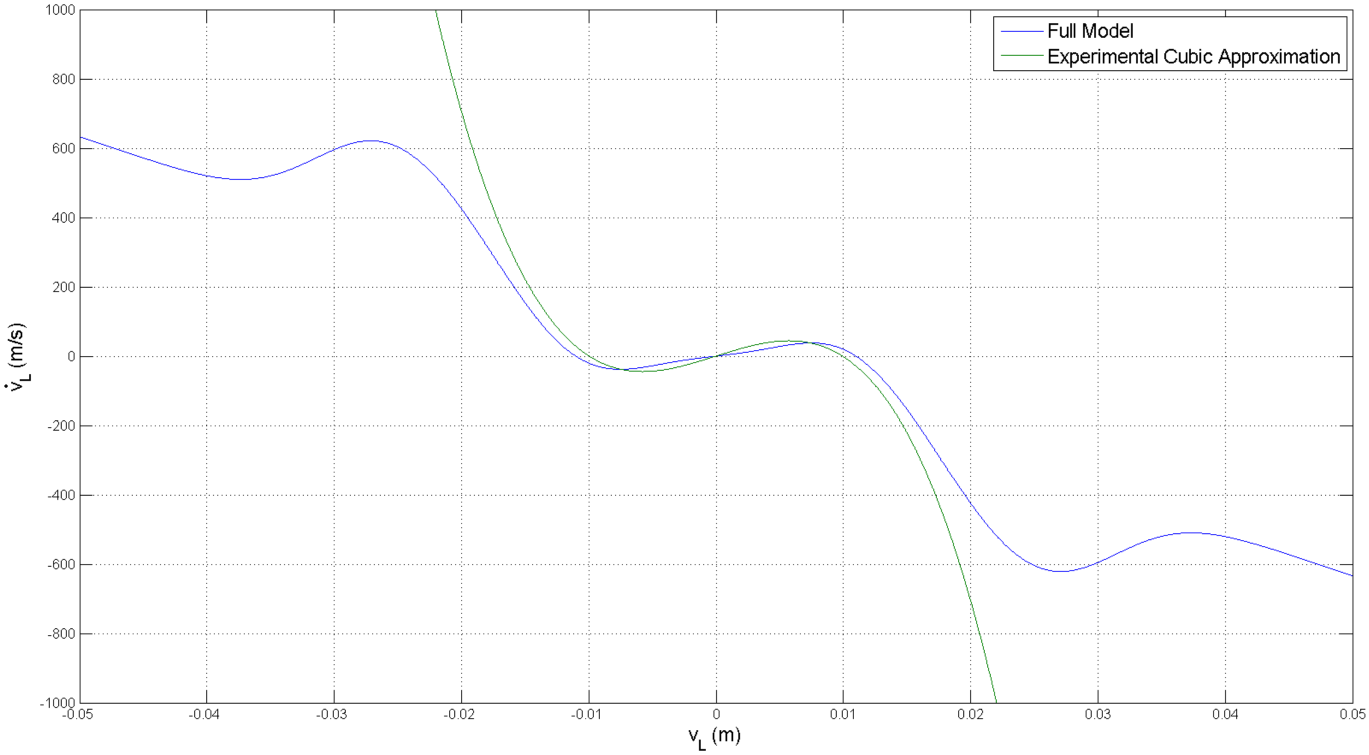

Figure 4.11: Comparison between experimental cubic approximation with full model, with qualitative divergence between the two for $||v_L|| > 0.02$.

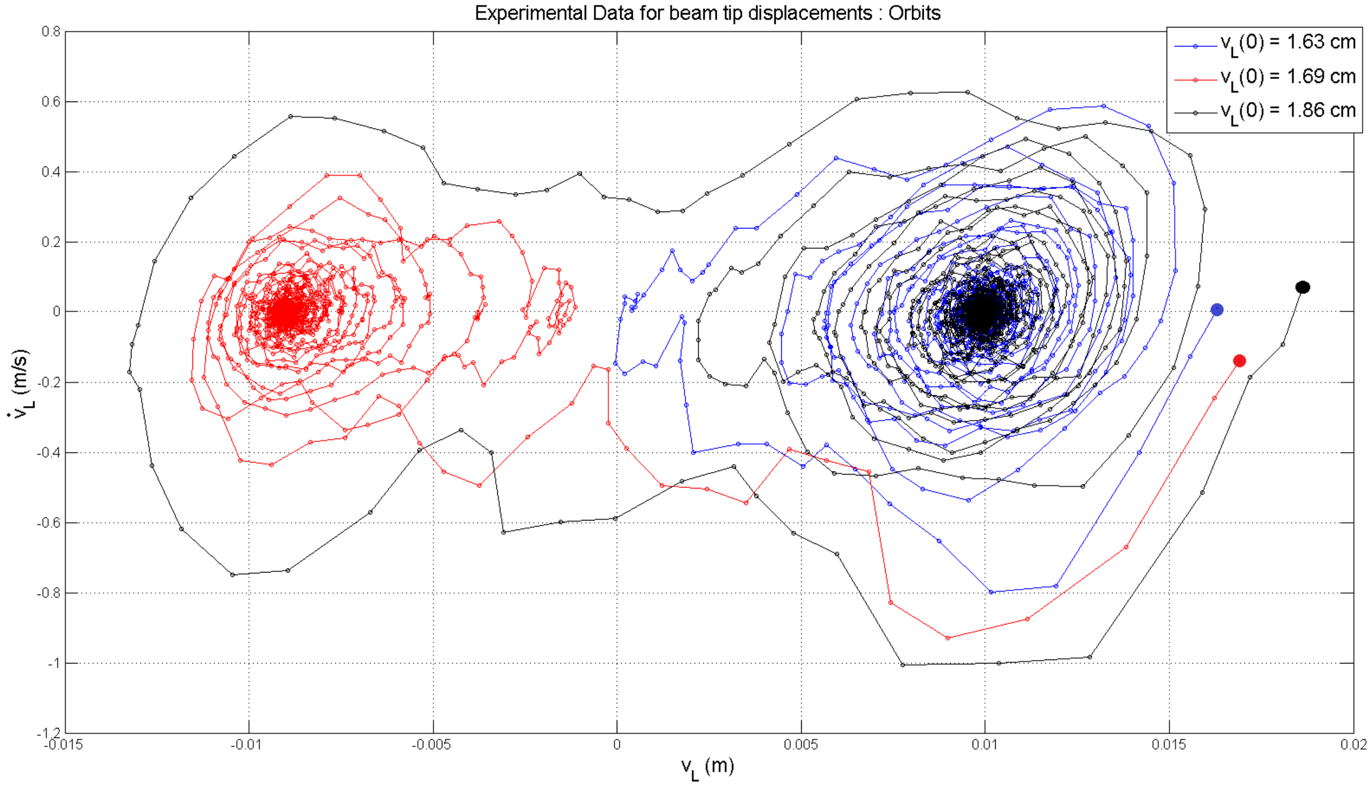

Figure 4.12: Orbits for displacement of beam tip near (0.99,0) along the basin of attraction. Initial points are indicated as filled circles.

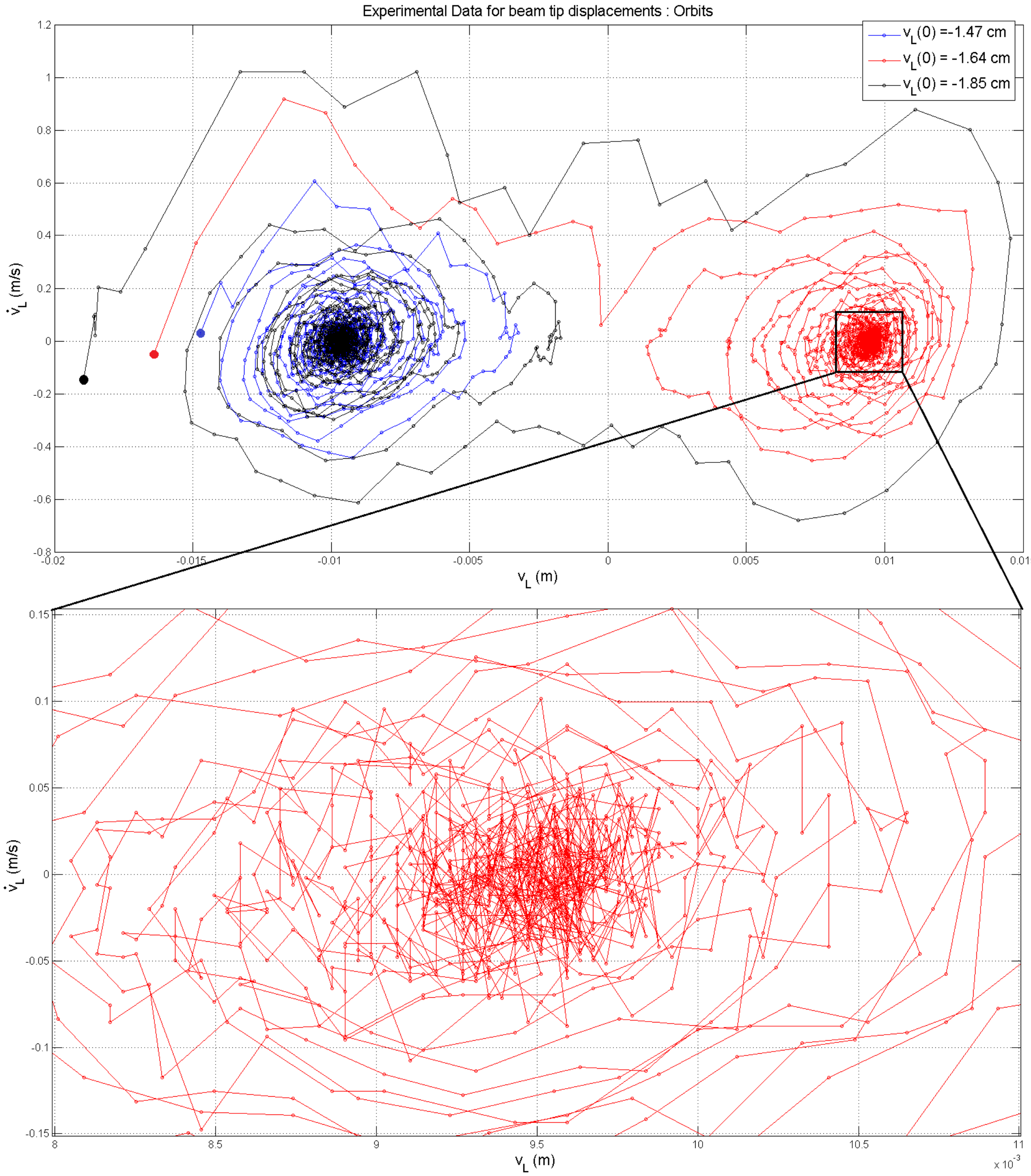

Figure 4.13: Orbits for displacement of beam tip near (-0.99,0) along the basin of attraction, and magnification of a region near (-0.99,0). Initial points are indicated as filled circles.

in figures 4.12 and 4.13 appear to cross, this is an artefact of the large-scale noise from the readings. The small-scale noise is clearly seen in the magnified region in figure 4.13, where we still have some noise in the position and velocity readings even when the beam is at an equilibrium point and is no longer moving. Nevertheless, the experimental data is sufficient to show the general structure of the basins of attraction of both stable fixed points.

4.3 Bifurcations of equilibria

Approximating $F_{static}(v_L)$ by a cubic approximation is valid for moderate beam tip displacements, but it is also important that $F_{static}(v_L)$ is such that there are three fixed points (as in the case described above) and that it is adequately modelled by a cubic. As detailed in Holmes [1], depending on the physical system parameters it is also possible for the system to have one or five fixed points as well. In these cases the cubic approximation does not model $F_{static}(v_L)$ accurately. We now investigate such bifurcations as physical parameters of the setup are changed, and show how $F_{static}(v_L)$ from the full model changes accordingly.

4.3.1 Varying distance between magnet centers while maintaining symmetry

We first present the bifurcation diagram as d increases in figure 4.14. All other physical parameters are the same as in section 3.1 from chapter 3. The bifurcation diagram is created by computing the fixed points and their stabilities from $F_{static}(v_L)$ of the full model. The shape of the bifurcation diagram is similar to that presented in figure 6 in [1].

In general, there are two main forces that determine the fixed points of the system: The magnetic force from the magnets and the elastic force from the beam. This is seen in equation 2.1.8. The proceeding discussion will reference the regions indicated in figure 4.14.

In region 1, for very small d, the magnets are very close to each other and are approximately right below the beam. We see that there is only one stable fixed point at $v_L = 0$. This is because the direction of the magnetic field is very similar to that of a single magnet underneath the beam, as seen in figure 4.15. Figure 4.16 shows a plot of $F_{static}(v_L)$ for $d =$ 2.74 cm. No experimental data in this section was available due to the strong repulsive force between the magnets making it hard to bring them close to each other.

In region 2, we see that a supercritical pitchfork bifurcation occurs and two new stable fixed points emerge while the stable fixed point at $v_L = 0$ becomes unstable. The two magnets are far enough apart now that the magnetic field is different from that described in

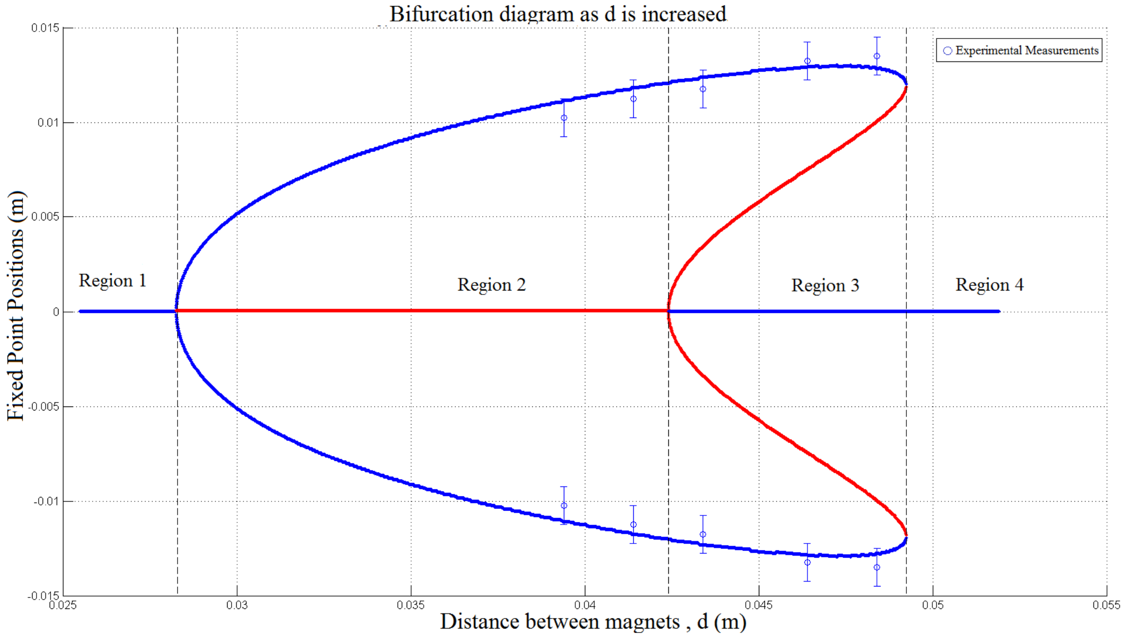

Figure 4.14: Bifurcation diagram as distance between magnets is increased. Solid curves are computed from the full model, circles are experimental data points with standard error bars. Red indicates unstable fixed points, blue indicates stable fixed points.

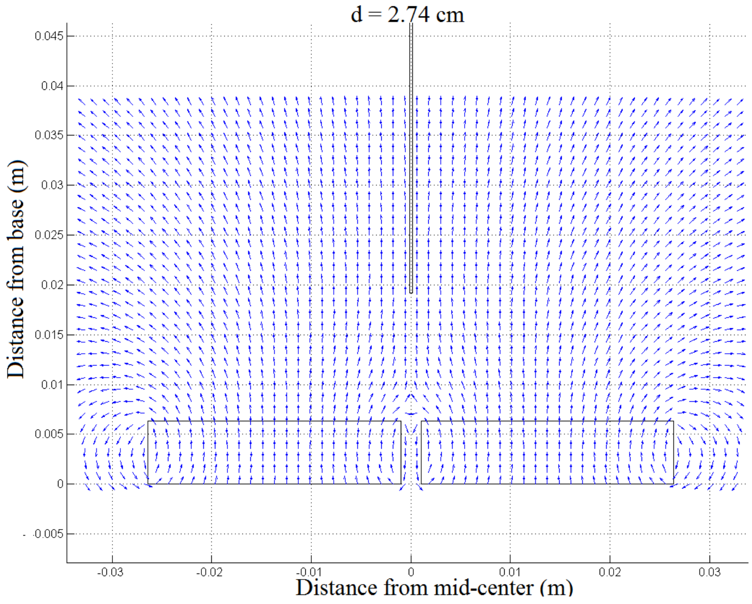

Figure 4.15: Magnet placement and magnetic field for $d = 2.74$ cm.

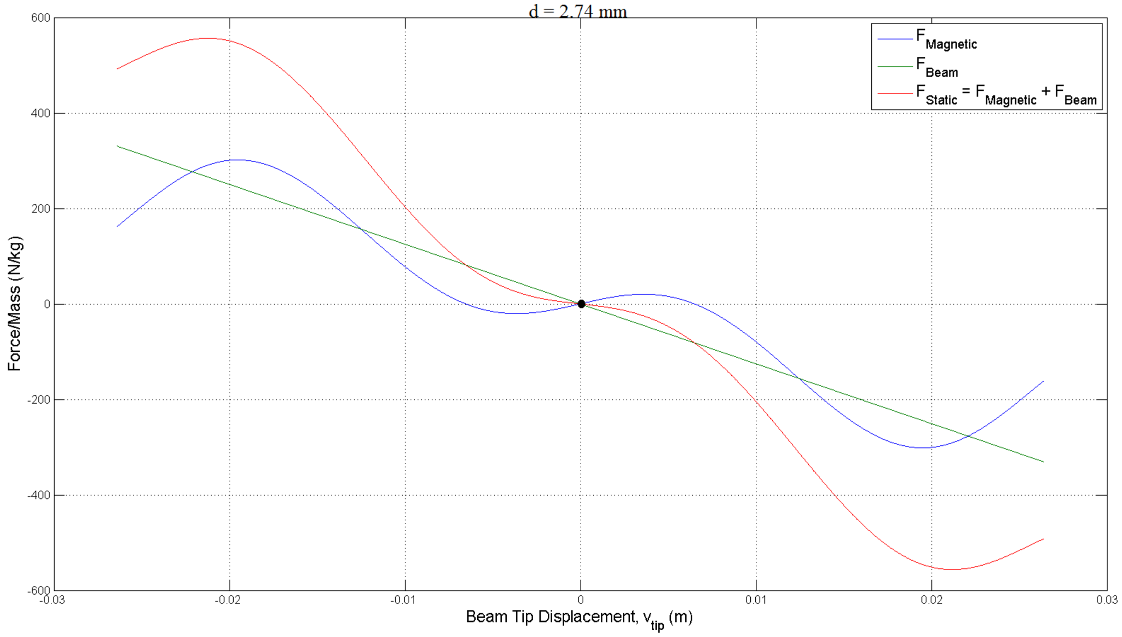

Figure 4.16: Full model: Contributions of $F_{magnetic}$ and F_{beam} to F_{static} for $d = 2.74$ cm. Stable fixed points indicated as dots.

the previous paragraph, but they are close enough to the beam tip such that the magnetic force on the beam tip is larger than the elastic restoring force, causing the beam tip to be attracted to either one of the magnets. Each magnet has its own domain of attraction, and the beam tip will be attracted towards the magnet that is closer to it. Our experimental setup ($d = 3.93$ cm) lies in this domain of the bifurcation diagram, and the magnetic field and corresponding F_{static} have been presented in figures 4.3 and 4.5.

In region 3, we see that a subcritical pitchfork bifurcation occurs, and the unstable fixed point at $v_L = 0$ becomes stable again while two new unstable fixed points emerge. The magnets are now far enough from the center vertical beam position that for small beam tip displacements from the center, the elastic restoring force is greater than the attracting force from the magnets. Thus for small beam tip displacements the beam tip will not be attracted towards the magnets and instead oscillate back towards the center. However, for large enough displacements, the beam tip is attracted towards the closer magnet as magnetic forces dominate again. The corresponding graph for F_{static} is presented in figure 4.17. We see from figure 4.17 that the system is close to a saddle-node bifurcation.

In region 4, we see that two saddle-node bifurcations occur and the pair of stable and unstable fixed points that were generated by the two pitchfork bifurcations annihilate. Physically, the magnets are now so far away from the center that the magnetic field is too weak, and the elastic restoring force of the beam dominates for all beam tip displacements. Hence,

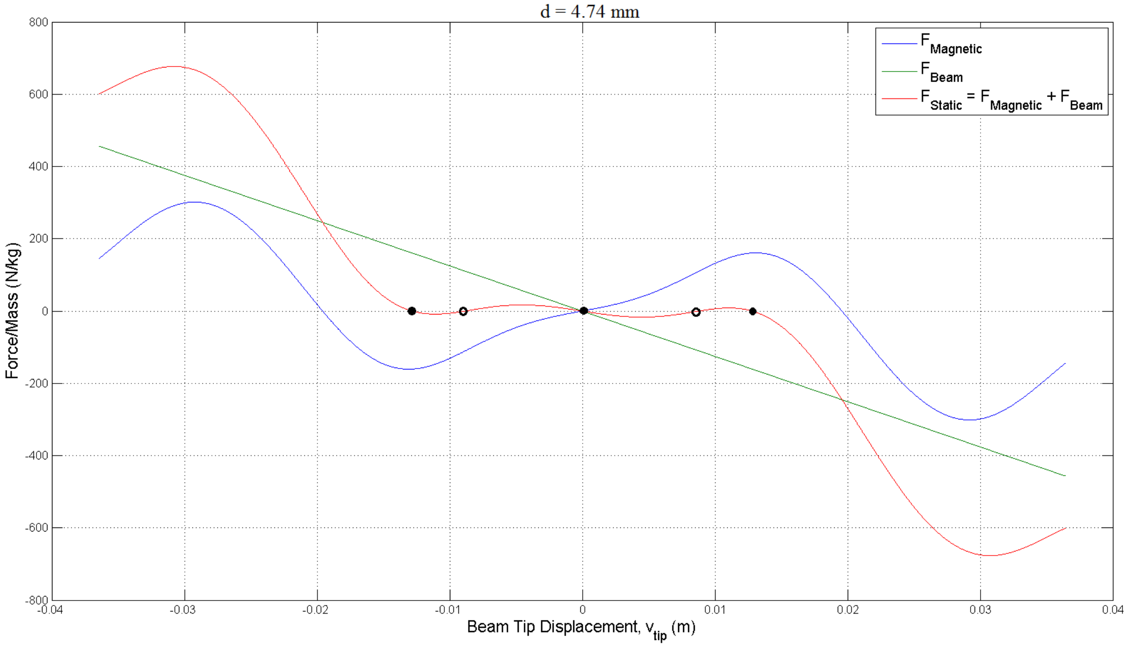

Figure 4.17: Full model: Contributions of $F_{magnetic}$ and F_{beam} to F_{static} for $d = 4.74$ cm. Stable fixed points indicated as dots, unstable fixed points indicated as circles.

the only fixed point is the stable fixed point at $v_L = 0$. The corresponding graph for F_{static} is presented in figure 4.18.

Pitchfork and saddle-node bifurcations are also observed for certain parameters that preserve the symmetry of the setup. The bifurcation diagram is shown in figure 4.19 for increasing Young's Modulus of the beam material. Increasing the Young's Modulus corresponds to increasing the stiffness of the beam material (we assume that no plastic deformation occurs in the beam). We see that a subcritical pitchfork bifurcation occurs follow by saddle-node bifurcations as E is increased.

4.3.2 Symmetry breaking via changing beam tip offset

Up until now we have assumed a symmetry of the system with respect to the vertical beam tip position. We now consider a situation where the symmetry of the setup is broken due to the magnets not being placed symmetrically about the vertical beam tip position. The result of this is that the vertical equilibrium beam tip position (without magnets) is offset from the center of the line between the magnet centers (henceforth referred to as the center point). An example is shown in figure 4.20 for an offset of 0.01 cm and $d = 3.93$ cm.

The bifurcation diagram is shown in figure 4.21 as this offset is varied with $d = \text{constant} = 3.93$ cm. Note that the fixed point positions are measured relative to the vertical equilibrium

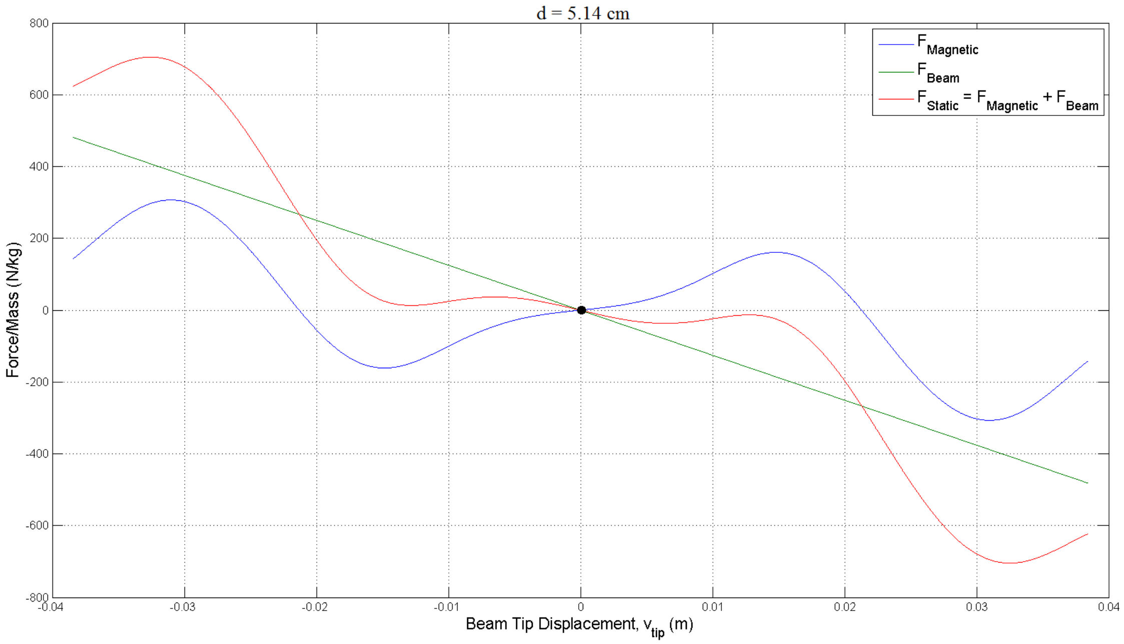

Figure 4.18: Full model: Contributions of $F_{magnetic}$ and F_{beam} to F_{static} for d = 5.14 cm. Stable fixed points indicated as dots.

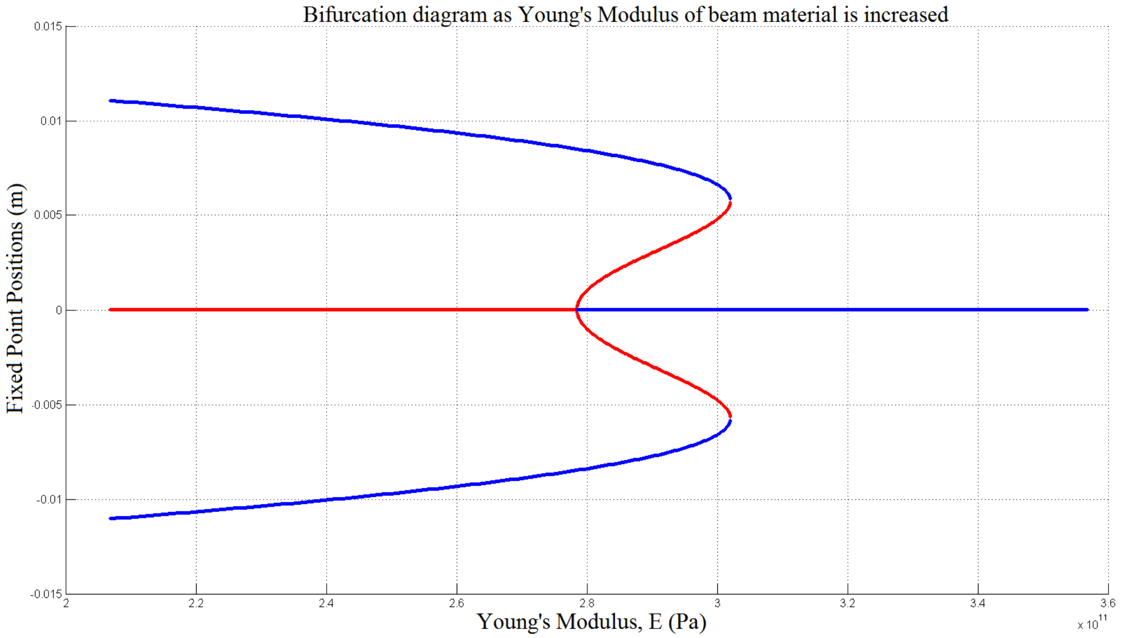

Figure 4.19: Bifurcation diagram for increasing Young's Modulus, $d = 3.93$ cm. Solid curves are computed from the full model. Red indicates unstable fixed points, blue indicates stable fixed points.

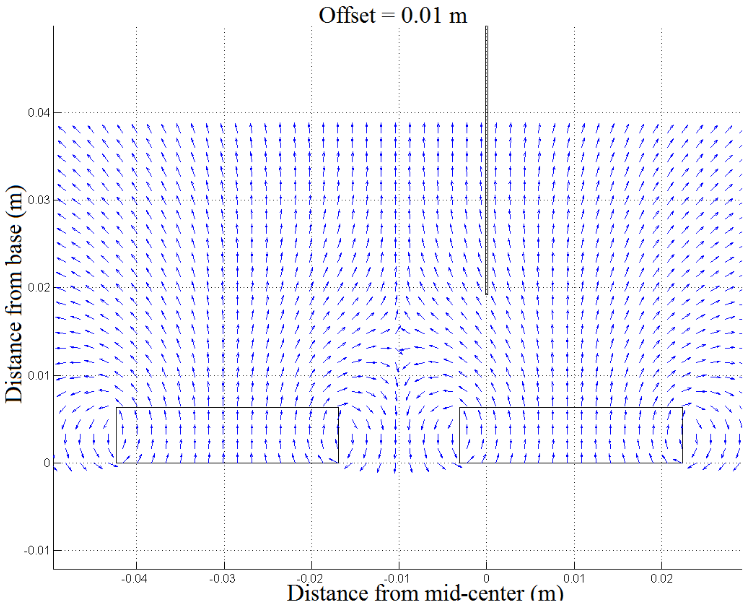

Figure 4.20: Setup with beam offset of 0.01 cm and $d = 3.93$ cm.

beam tip position, and not the center point between the magnets.

We see that for small offsets (region 1 in figure 4.21), there is still a saddle in between two stable fixed points, but as the offset is increased the saddle point moves closer to one of the stable fixed points corresponding to the magnet that is further away from the vertical beam tip position. This makes sense physically since the magnet that is closer to the beam exerts a stronger attracting force on the beam compared to the magnet that is further away from the beam, and hence we have to displace the beam further to get the beam to snap toward the further magnet. F_{static} is shown in figure 4.22 for an offset of 0.1 cm with $d = 3.93$ cm.

For larger offsets (region 2 in figure 4.21) a saddle-node bifurcation occurs at around an offset magnitude of 2.71 mm. Only one stable fixed point remains. This corresponds to the having one of the magnets being too far away from the beam, and hence the elastic restoring force is larger than the magnetic force exerted by that magnet for all beam tip displacements. F_{static} is shown in figure 4.23 for an offset = 0.5 cm with $d = 3.93$ cm.

We can examine the full behaviour of the system by considering even larger offsets (see figure 4.24). In addition to the saddle-node bifurcations at offsets of ± 2.71 mm that have been seen in figure 4.21, we have additional saddle-node bifurcations at offsets of ± 4.4 cm and ± 4.6 cm. These additional saddle-node bifurcation correspond to a weakening of the magnetic field around the beam due to the distance of the beam from both magnets.

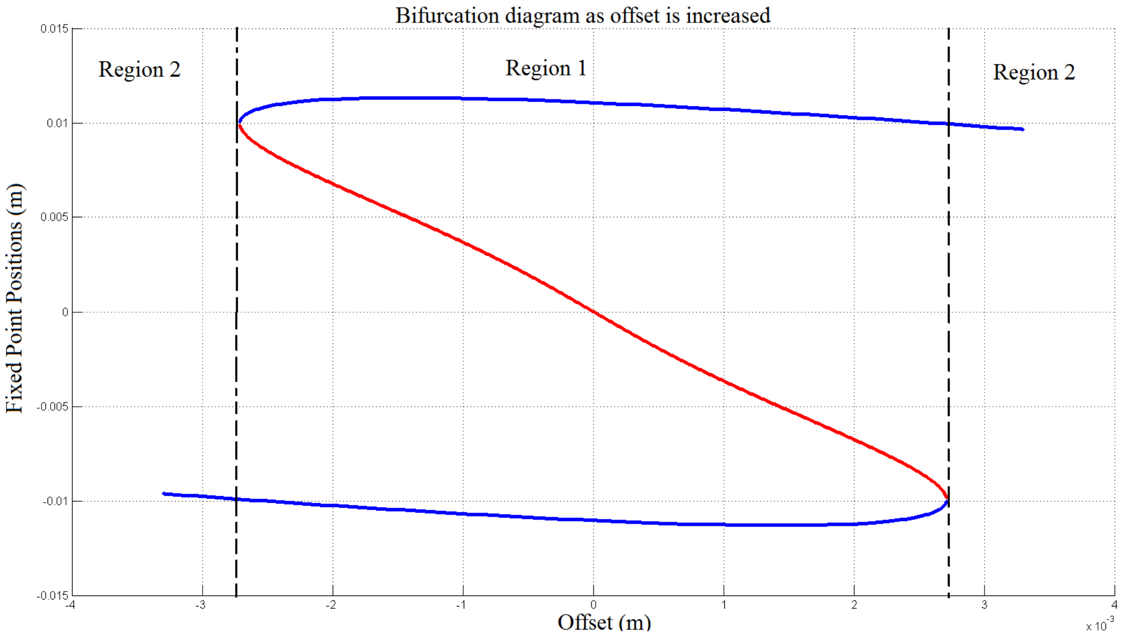

Figure 4.21: Bifurcation diagram for offset magnitudes of up to 3.3 mm, with $d = 3.93$ cm.

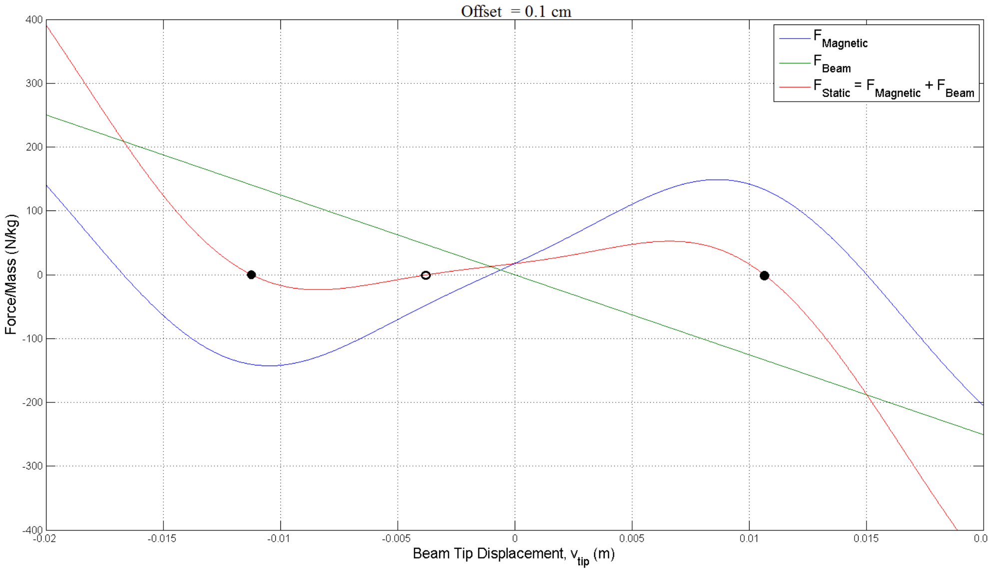

Figure 4.22: Full model: Contributions of $F_{magnetic}$ and F_{beam} to F_{static} for an offset of 0.1 cm with $d = 3.93$ cm. Stable fixed points are indicated as dots, unstable fixed points are indicated as circles.

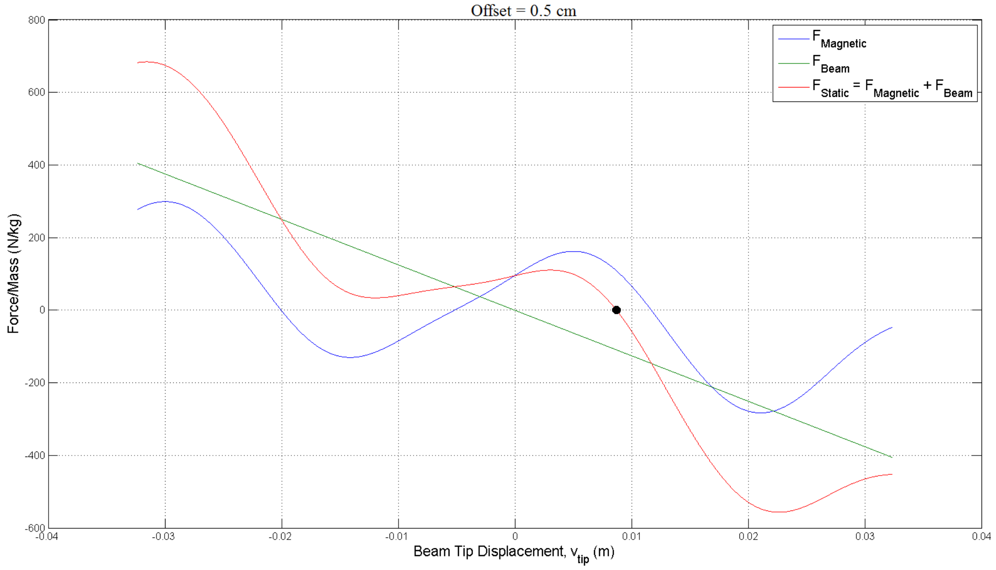

Figure 4.23: Full model: Contributions of $F_{magnetic}$ and F_{beam} to F_{static} for an offset of 0.5 cm with $d = 3.93$ cm. Stable fixed points are indicated as dots

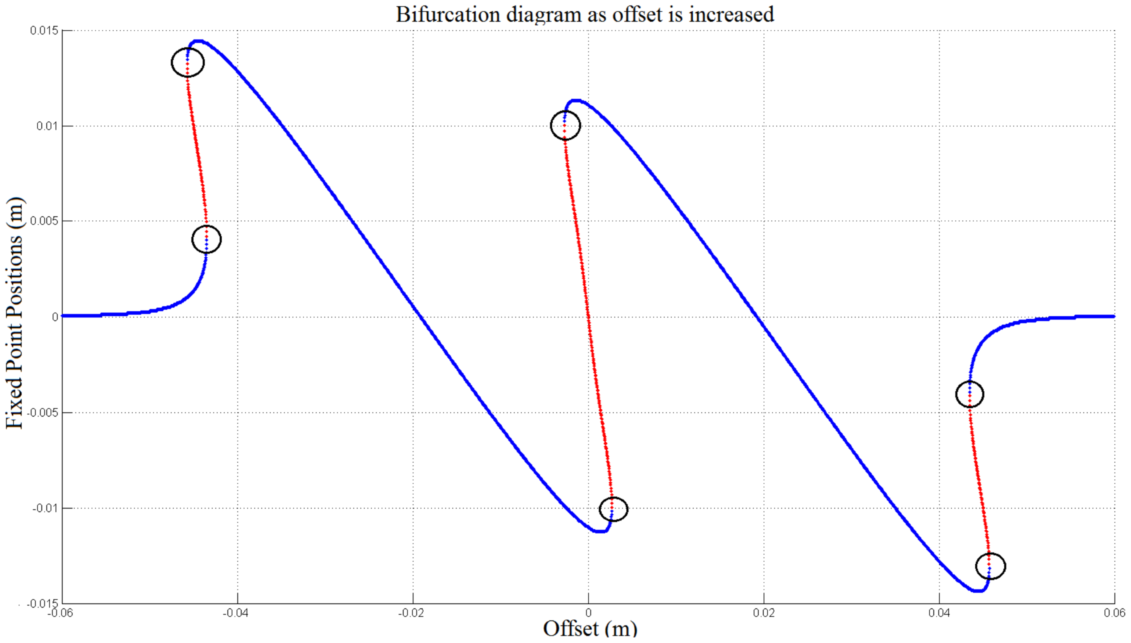

Figure 4.24: Bifurcation diagram for offset magnitudes of up to 6 cm wit $d = 3.93$ cm. Solid curves are computed from the full model. Red indicates unstable fixed points, blue indicates stable fixed points. Saddle-node bifurcations are highlighted in circles.

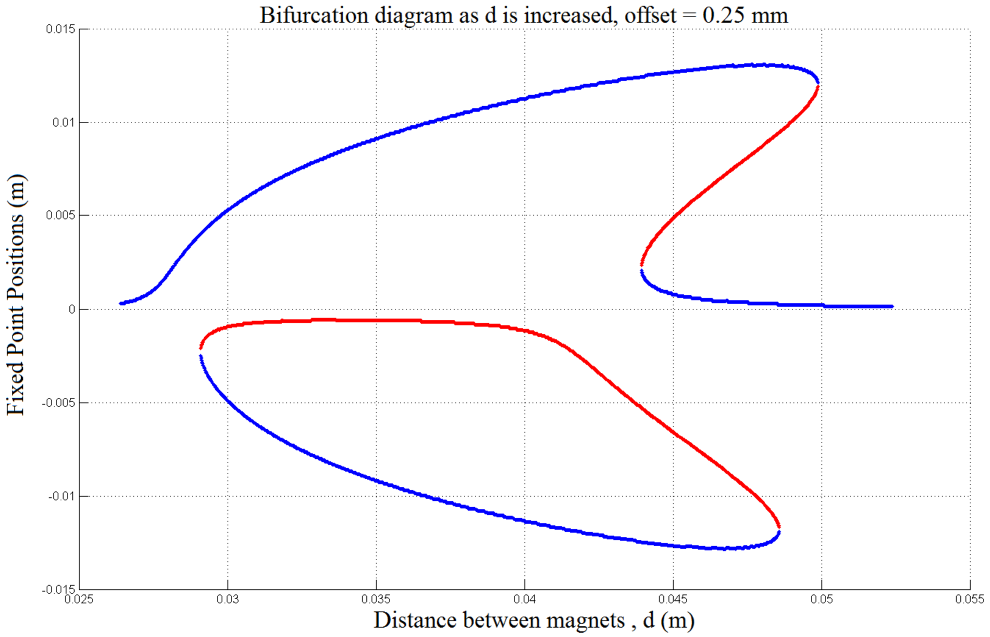

Figure 4.25: Bifurcation Diagram as d is increased with a constant offset of 2.5 mm. Solid curves are computed from the full model. Red indicates unstable fixed points, blue indicates stable fixed points.

4.3.3 System stability in two-parameter space

In subsection 4.3.1, the parameter that was varied (distance between magnet centers) was one that preserved the symmetry of the setup, whereas in subsection 4.3.2, the variation of the parameter (beam tip offset) resulting in a breaking of symmetry. In order to gain a larger view of the bifurcations, we can consider a two-dimensional parameter space. Thus, the fixed points over this parameter space form a surface. For an example of such a surface, see page 72 of [14]. To visualize this whole surface requires visualization in three dimensions - two dimensions for the parameters and one for the fixed point positions. However, we can take slices of this surface via bifurcation diagrams by holding one parameter constant. Two such bifurcation diagrams have already been presented in figures 4.14, 4.21 and 4.24. We can also visualize the structure of this surface by constructing a bifurcation set for the two parameters. In the following figures, we consider a parameter space with d as one parameter and the offset as another parameter.

We first consider the case where there is a non-zero offset which breaks the symmetry, and vary d. This is shown in figure 4.25. The shape of the bifurcation diagram is similar to that of an imperfect pitchfork [14].

We next consider the case where there are 5 fixed points for a zero offset, and vary the offset. This is shown in figure 4.26.

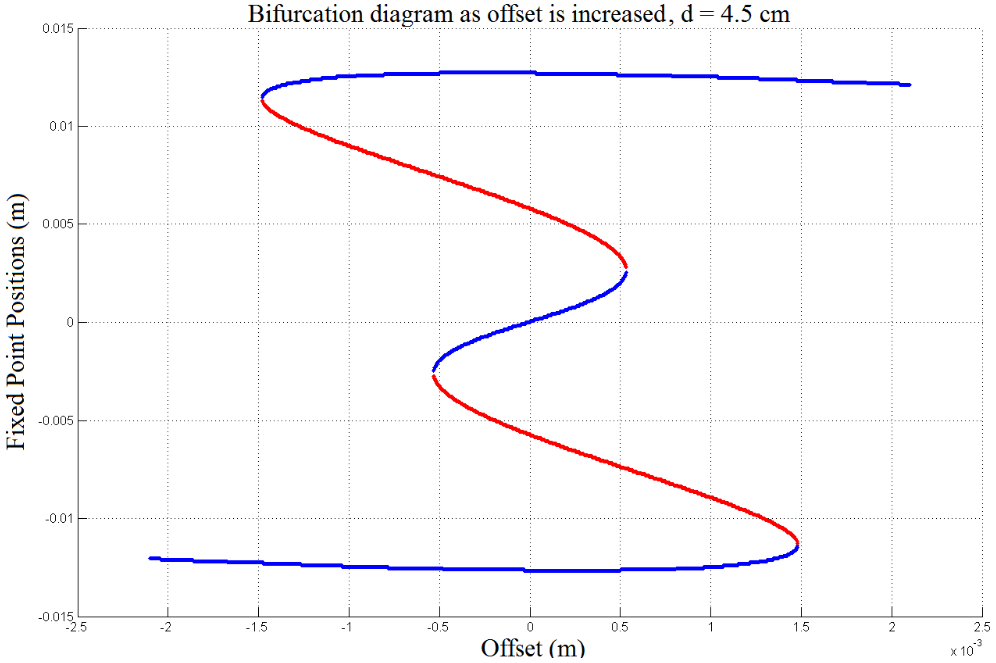

Figure 4.26: Bifurcation Diagram as offset magnitude is increased for a constant d of 4.5 cm. Solid curves are computed from the full model. Red indicates unstable fixed points, blue indicates stable fixed points.

We can construct a bifurcation set of the system for the two parameters, shown in figure 4.27. The same bifurcation set with corresponding 'slices' of bifurcation diagrams is shown in figure 4.28. Slice numbers are shown in circles next to corresponding slice lines. Slice 1 corresponds to figure 4.14, slice 2 corresponds to figure 4.25, slice 3 corresponds to figure 4.21, and slice 4 corresponds to figure 4.26.

We can also plot the fixed points over the two parameters in 3-dimensional space, given in figure 4.29. The resulting points that lie on the stability surface actually forms a cusp catastrophe surface, of which research has been done on [23]. However, this surface is slightly more complicated due to there being two pitchfork bifurcations instead of just one, resulting in three stable surfaces (surfaces formed by the set of stable fixed points) - An 'upper' one, a 'middle' one and a 'lower' one. These stable surfaces are connected by unstable surfaces, giving the impression of the stable surfaces being 'folded' over the other stable surfaces, with the unstable surfaces being the connecting 'fold'. The number of 'folds' that one can see when projecting the surface onto the two-parameter space corresponds to the number of fixed points in the bifurcation set shown in figure 4.27.

A physical example of a catastrophe is to consider the case of our system being such that the beam offset is zero, and the distance between magnet centers is 3.93 cm, so that we have an unstable fixed point (saddle) between two symmetric stable fixed points. Let

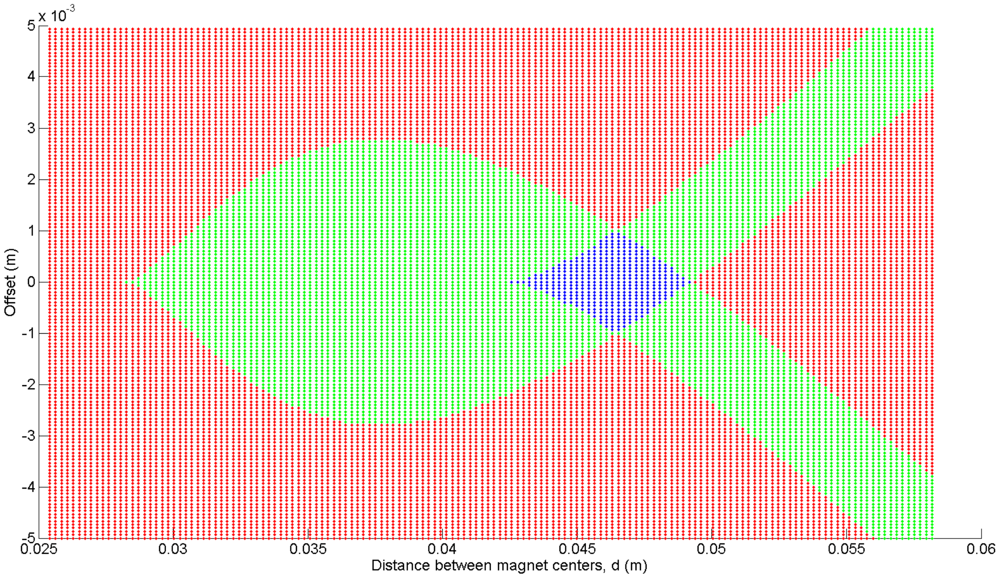

Figure 4.27: Bifurcation set for parameters d and offset. Red regions denote 1 fixed point, green regions denote 3 fixed points, blue regions denote 5 fixed points. Saddle node bifucations occur on boundaries between regions, except at cusps on the line offset = 0, where pitchfork bifucations occur.

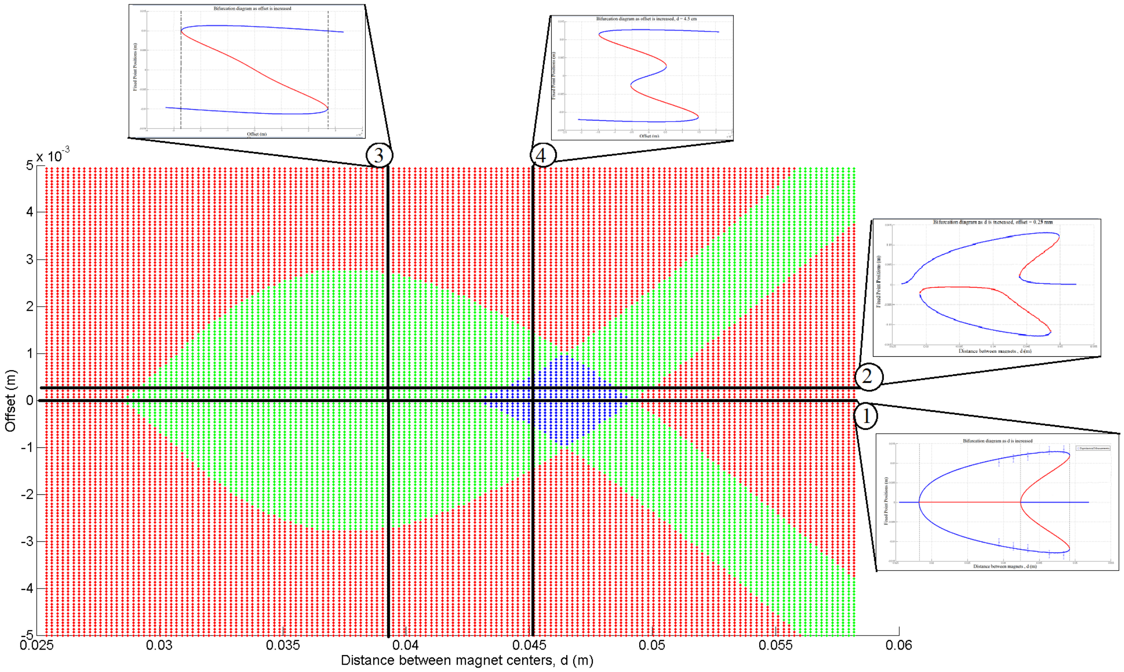

Figure 4.28: Same Bifurcation set as for parameters d and offset, shown with 'slices' corresponding to previously-presented bifurcation diagrams.

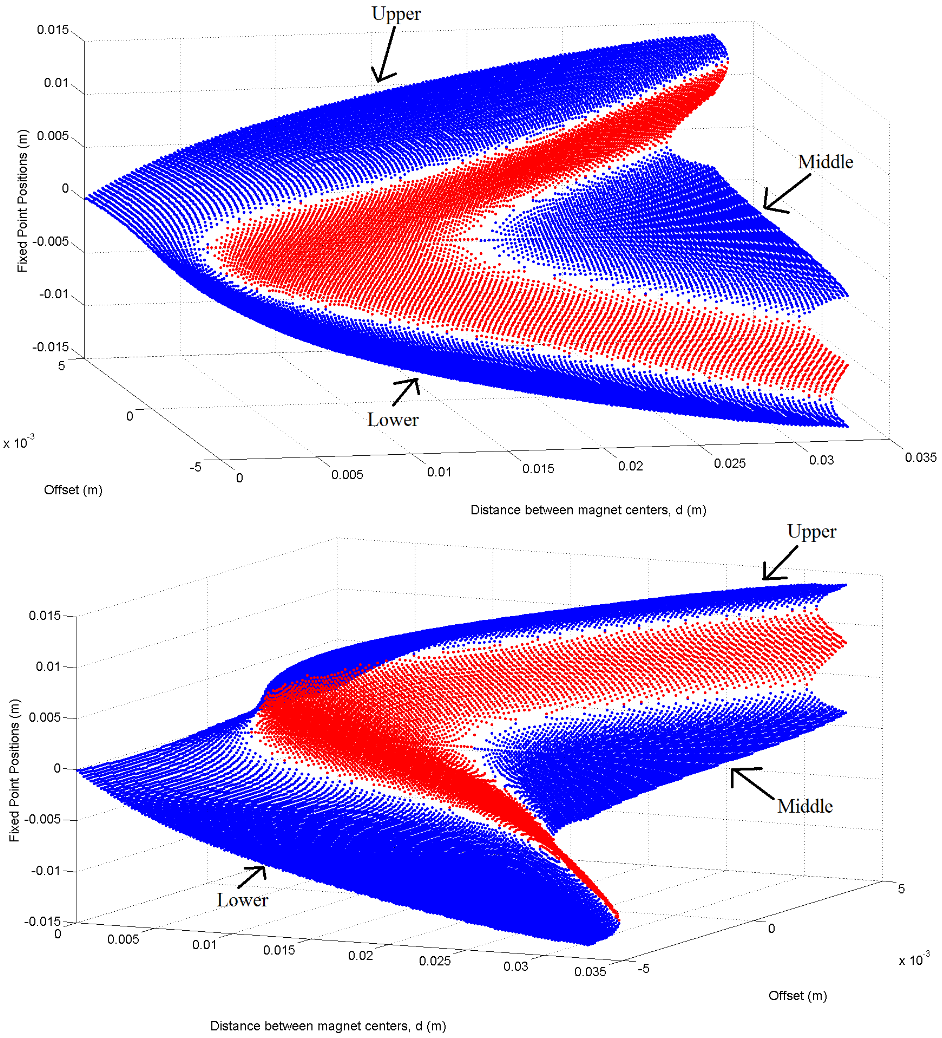

Figure 4.29: The surface of equilibria as computed using the full model over the two-parameter bifurcation set : two different views, with the relative positions of stable surfaces indicated. Blue denotes stable equilibria, red denotes unstable equilibria.

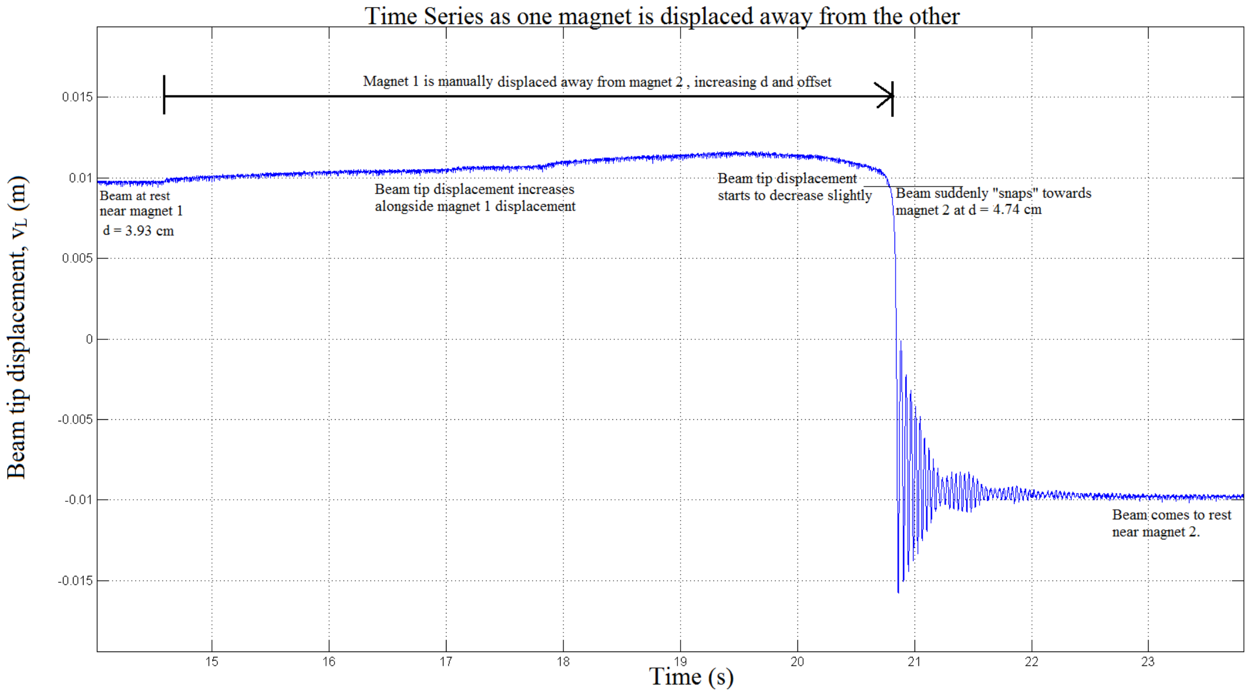

Figure 4.30: Time series as magnet 1 is displaced away from magnet 2 from an initial $d =$ 3.93 cm to $d =$ 4.74 cm, illustrating a catastrophe as the stable fixed point 'jumps' from one stable surface to another.

the beam tip be attracted towards one of the magnets (call this magnet 1, and the other magnet, magnet 2), and consider what happens as we move magnet 1 away from magnet 2, keeping all other variables constant. This is equivalent to increasing d *and* increasing the offset magnitude as well. Initially the beam tip will be displaced further outward as magnet 1 is moved further outward, moving along with the stable equilibrium point associated with magnet 1. However, there is a certain point where the elastic force on the beam is greater than the magnetic force exerted on the beam, and the stable equilibrium point associated with magnet 1 disappears due to the saddle-node type bifurcations seen in figure 4.21, and the beam tip will then swing towards magnet 2, demonstrating the catastrophe. See figure 4.30 for experimental measurements of this. In terms of the 3-D equilibria surface in figure 4.29, this corresponds to 'jumping off' from the edge of one of the stable surfaces to another. Hysteresis can also be seen by considering what happens if we start to move magnet 1 back towards magnet 2. We will need to move magnet 1 closer to magnet 2 compared to the initial conditions of d = 1.4 cm to get the beam tip to swing back towards magnet 1.

We see how the full model is very useful in studying the bifurcations and catastrophes that happen in the system as the physical parameters are varied, something that would not have been possible if we had just used a cubic approximation for F_{static}. We now turn our attention towards the case where the system is periodically forced.

Chapter 5

Results and Discussion II

In this chapter we focus on the case where we have magnetic fields as well as forcing from the shaker. We first provide an explanation of the Poincaré map, which allows us to analyze the 3-D orbits of the system in terms of a map on a 2-D surface. We then consider the system as small-amplitude forcing is introduced, providing results from both our experimental setup as well as from numerical simulations of the full model. Next, we investigate the system when the forcing is increased such that "strange attractor" motions start to occur. We provide some background theory behind these motions as well as experimental and numerical results that demonstrate these "strange" motions. We conclude the chapter by presenting the bifurcation diagram as a physical parameter (magnet field strengths) is increased in order to demonstrate to usefulness of the full model.

5.1 Poincaré map

If we now include periodic forcing, we now need to consider all of the terms in equation 2.1.14, With $P \neq 0$, the ODE is now non-autonomous. (Remember that $P = \omega^2 A_0 \phi(L) \int_0^L \phi \, ds$ as defined in equation 2.1.13). However, we can rewrite equation 2.1.14 as an autonomous 3-dimensional system as follows, with $v_1 = v_L$:

$$\begin{aligned} \dot{v_1} &= v_2, \\ \dot{v_2} &= F_{static} - \delta v_2 + Pcos(\omega\tau), \\ \dot{\tau} &= 1. \end{aligned} \tag{5.1.1}$$

Notice that the vector field presented in equations 5.1.1 is periodic in τ (and therefore periodic in t) with period $\frac{2\pi}{\omega}$. Thus, the solutions of the system actually reside in the 3-D space $\mathbb{R}^2 \times \mathbb{S}^1$, where $\mathbb{S}^1$ is a circle of length $T = \frac{2\pi}{\omega}$, T being the period of the forcing. Note that this does not necessarily mean that the orbits of the system are also periodic.

Now consider the 2-D surface consisting of the v_L-$\dot{v_L}$ planar cross-section Σ at $\tau = 0$, formally defined as $\Sigma = \{(v_L, \dot{v_L}, \tau) \in \mathbb{R}^2 \times \mathbb{S}^1 | \tau = 0\}$. Hence, $\Sigma \in \mathbb{R}^2$. Since $\dot{\tau} = 1$, this surface is always transversal to the flow of the system. Hence, we can consider the Poincaré map G defined on the surface Σ for the system in equations 5.1.1.

The 2-D Poincaré map G can be defined in our case as follows: Let p be a point on Σ. p generates a 3-D trajectory that evolves in time under the flow specified by equations 5.1.1. Since the τ component of the flow is defined over $\mathbb{S}^1$, this trajectory must eventually intersect Σ again at some point q after a duration of $T = \frac{2\pi}{\omega}$. The Poincaré map G over Σ is defined such that $G(p) = q$ for every point p on Σ. Thus, the Poincaré map maps points on Σ to points on Σ, and (in our case) is a non-linear map with stable and unstable manifolds [2]. By analysing the orbit structure of the 2-D Poincaré map, we can correspondingly gain insight into the orbit structure of the 3-D system in equations 5.1.1 without having to visualize the flow and orbits in 3 dimensions. For a Poincaré map G, let $G^n(p)$ denote n iterations of G on a point p. For an arbitrary point p_0 on Σ, if there is a cycle of k distinct points $p_j = G^j(p_0), j = 0, 1, ..., k-1$ and $G^k(p_0) = p_0$, then there is a periodic orbit of period k for the map defined by G [2].

If we approximate F_{static} using a cubic, we obtain the equation for the forced damped Duffing oscillator. The dynamics of the corresponding Poincaré map have been thoroughly analyzed [3]. Some of the relevant theory is repeated here for comparison with results from the full model as well with experimental results. In the following discussion, it is assumed that we are in the double-well potential regime where $F_{static}(v_1)$ is well-approximated by a cubic, unless explicitly specified. The experimental parameters are the same as given in section 3.1 from chapter 3.

For the numerical simulations involving the full model in this section, we use a higher grid density and increased ODE solver accuracy. We use 5000 nodes along ϕ and 20000 nodes along v_L corresponding to a grid size of 2.6×10^{-6} . Matlab's ODE113 is used as the ODE solver, which is has more stringent error tolerances than ODE45. We specify a relative tolerance of 10^{-10} and an absolute tolerance of 10^{-8} for the ODE solver.

All Poincaré maps are produced from processing data of the position and velocity time series, both experimentally and numerically. In terms of numerical simulations, a particular forcing frequency f is specified, which will correspond to a period of $T = 1/f$ that is used to sample points for the Poincaré maps from the position and velocity time series, which are produced from numerical simulations.

Poincaré maps from experimental data are produced by noting the frequency f of the driving signal as displayed digitally by the signal generator, and then calculating a period $T = 1/f$ that is used to sample points for the Poincaré maps via linear interpolation of the experimental data. The circuit used to collect and process the position and velocity measurements has already been discussed in section 3.2 of chapter 3. An important detail is that the sampling of points for the Poincaré map from experimental data is not directly synchronized with the driving signal of the signal generator. Rather, we only measure the position and velocity of the beam tip, and then from post-processing of the resulting time series we generate a Poincaré map based on the driving frequency as displayed by the signal generator. Thus, one of the assumptions is that the frequency as displayed by the signal generator is close to the actual output signal to the shaker. If the signal frequency is different than the output frequency, then the error from the differences in frequency will result in a drift of a fixed point across the projected orbit when generating the Poincaré map. Even though this method is not as accurate as if we had synchronized the driving signal with the sampling of the position and velocity signals from the ADC, the resulting Poincaré maps are sufficiently clear enough to display the relevant fixed points and structures of the Poincaré map.

5.2 Forced oscillations : Small forcing amplitudes

5.2.1 Theory

For small forcing, the topology of the Poincaré map is similar to the case of no forcing. The saddle and stable spiral sink *nodes* in the 2-D phase plane analysis in section 2.3.2 for the unforced case now become saddle-type and sink-type period-1 *orbits* in the 3-D phase space. If A_0 is small, then P is small and hence there are two attracting and one repelling closed orbits for the system described by equations 5.1.1 as the previously fixed points of the unforced case“oscillate” as τ evolves. Thus, the Poincaré map has a saddle and two stable sinks corresponding to the one repelling and two attracting closed orbits, with similarly-shaped stable and unstable manifolds of the saddle at (0,0) as that of the unforced case. As the forcing amplitude increases, so do the amplitudes of the orbits (but maintaining low forcing amplitudes).

An experimental observation is that for a constant low-amplitude forcing, there can exist both small-amplitude periodic oscillations of the beam tip about both static equilibrium points as well as large-amplitude periodic oscillations encircling all three equilibrium points. In general such coexistence of periodic orbits can occur (See [2], page 87.)

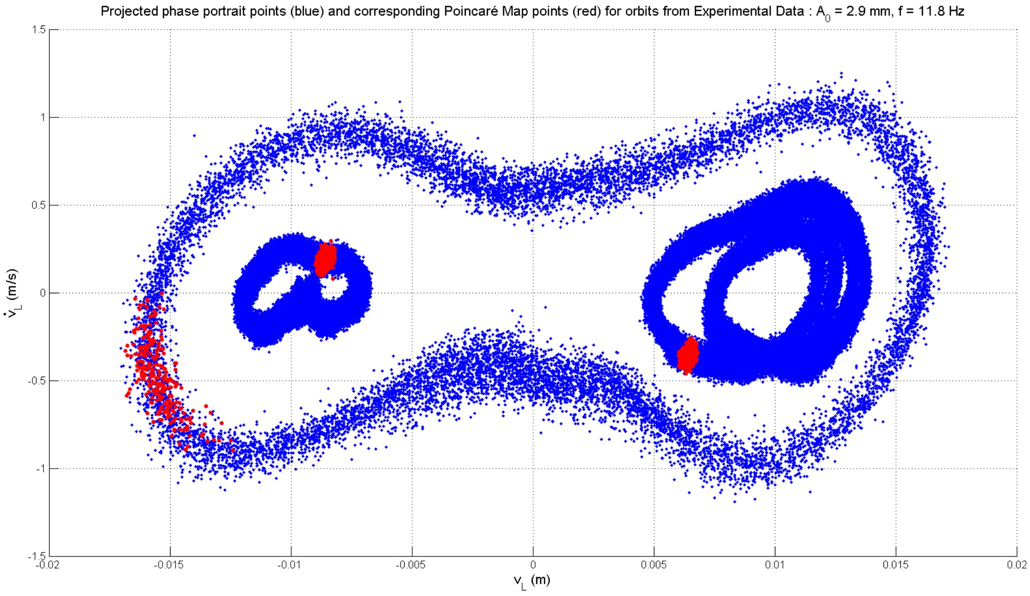

Figure 5.1: Projected orbits (blue) and corresponding Poincaré Map points (red) from experimental data, with $A_0 = 2.9$ mm and $f = 11.8$ Hz. Correspondingly, $P = 24.96$.

5.2.2 Results from experiment and numerical simulations

We present the Poincaré maps from experimental data, as well as from numerical simulations of the full model in figures 5.1 and 5.2 respectively for $A_0 = 2.90 \pm 0.05$ mm and $f = 11.38 \pm 0.05$ Hz.. The blue points correspond to the relevant orbit projected onto the v_L-$\dot{v_L}$ plane, and red points are points from the Poincaré map taken from the orbit.

We see that the structure of the orbits from experimental data are similar to that those computed from the full model. However, the projected orbits and Poincaré map points for the experimental data are much more "fuzzier" and spread out compared to the numerical simulations. A factor in this is the errors introduced by the electronic components used to collect data such as the strain gauge, amplifier and analog-to-digital converter, as well as electronic noise which is amplified by the amplifier. However, we also notice that the experimental Poincaré map points are more spread out compared to the numerical simulations (which are computed with much higher accuracy than can be afforded with experiment). This is especially noticeable for the large-amplitude orbit. A reason for this is due to the uncertainty and possible drift in the forcing frequency from the signal generator. Thus, if our sampling frequency for the Poincaré map is slightly different from that of the forcing frequency (possibly due to the lack of synchronization as explained in section 5.1), this will lead to a drift in the Poincaré map points over the projected orbit. Thus, there is a limit to the time-span over which the Poincaré map can be taken from the experimental data.

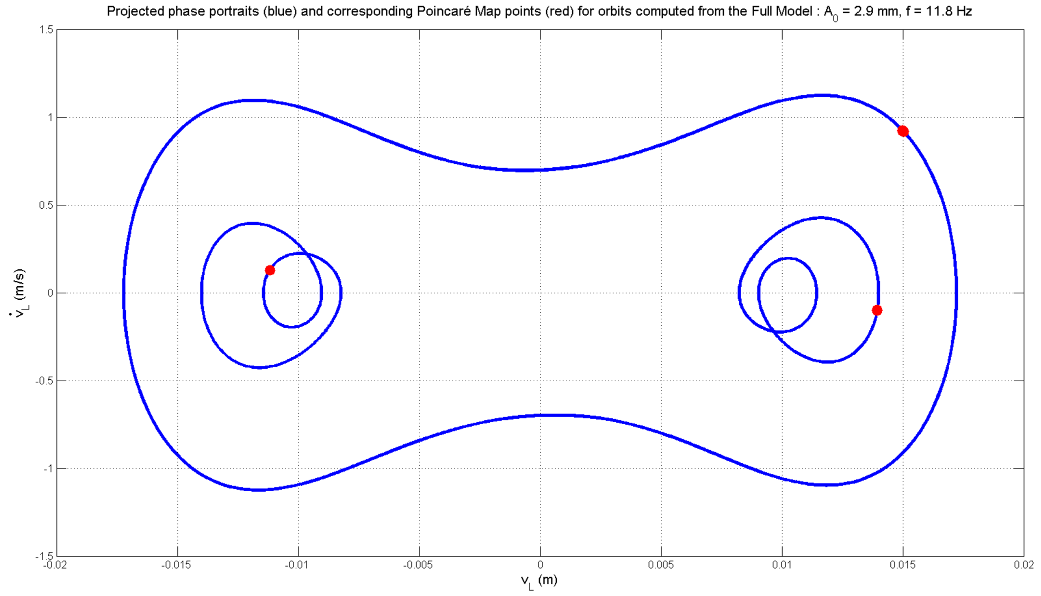

Figure 5.2: Projected orbits (blue) and corresponding Poincaré Map points (red) from numerical simulations of full model, with $A_0 = 2.9$ mm and $f = 11.8$ Hz. Correspondingly, $P = 24.96$.

For the larger-amplitude orbit, the Poincaré map is taken over a time series of 20 seconds, or 236 forcing periods. For the smaller-amplitude orbits, the Poincaré map is taken over a time series of 180 seconds, or 2124 forcing periods. We notice that the larger-amplitude orbit shows more error compared to the smaller-amplitude orbits as the Poincaré map points are more spread out, even though the Poincaré map for the larger-amplitude orbit is taken over a shorter time frame. A possible reason for this is the nature of the large-amplitude oscillations themselves, as there is a higher relative uncertainty in position and velocity over the same time step for large-amplitude oscillations compared to small-amplitude oscillations at the same frequency, assuming a constant sampling rate for both. Thus, there will be an increased error associated with the linear interpolation used to generate the Poincaré map for the large-amplitude oscillations, on top of the error due to differences between sampling and forcing frequencies.

Another difference is that the fixed points of the experimental Poincaré map are at different positions compared to the numerically-simulated Poincaré map. This is because the cross-section Σ for the experimental data is not taken exactly at $\tau = 0$, as it is difficult to synchronize the beginning of data collection with the exact time the orbit crosses Σ at $\tau = 0$. This is another error that arises from not being able to synchronize the data collection with the driving signal from the signal generator, and also from the time difference between initializing and starting data acquisition. The result is that the fixed points of the experimental Poincaré map will lie at different locations along the projected orbit compared to the fixed points of the numerically-computed Poincaré map. However, this is not a significant error as our goal is to show the agreement between experimental and computational data in terms of possible orbits that can be achieved and their corresponding fixed points on the Poincaré map, which differ by just a phase.

5.3 Forced oscillations : Medium and large forcing amplitudes

5.3.1 Theory

As the forcing of the Duffing oscillator is increased, it has been shown using the methods of Mel'nikov [24] that the stable and unstable manifolds of the saddle point (0,0) of the Poincaré map wind back and forth and grow closer to each other until they eventually touch and then intersect transversally. Specifically, the critical forcing parameter for which they touch is given as[1][3]:

$$P_c = \frac{4}{3}\left[\frac{\delta\alpha^{\frac{3}{2}}}{\pi\omega\sqrt{2\beta}}\right]\sinh\left(\frac{\pi\omega}{2\sqrt{\alpha}}\right). \tag{5.3.1}$$

The transverse intersection of the stable and unstable manifolds that occur for $P > P_c$ mean that there will be homoclinic points on the Poincaré map giving rise to homoclinic orbits. Moreover, since the manifolds are invariant under the Poincaré map (invariant meaning that orbits on the manifold stay on the manifold), the existence of one intersection implies the intersection of infinitely many intersections. The result is an extremely complex invariant set Ω_h, a "Smale horseshoe", in the neighbourhood of the stable and unstable manifolds. Ω_h possesses orbits of all periods in addition to dense non-periodic orbits.

This complex structure induces homoclinic motions, which causes the orbit to 'wander' erratically before approaching an attracting set. For P slight larger than P_c, the two stable sinks still exist and almost all orbits approach either one of the sinks as $t \to \pm\infty$. As the forcing is increased, the fixed points (sinks) become saddle points and they each throw off a pair of sinks, and this bifurcation occurs for each pair of sinks as the forcing is increased further, giving rise to orbits of period $2, 4, 8, 16, \ldots$. After a certain point there are so many bifurcations that periodic points on the Poincaré map can no longer be clearly distinguished,

---

[1] The equation for P_c given here is different compared to the equation given in [3], in that α and β are switched. This is due to the way α and β are defined differently in [3]

and the iterates of the Poincaré map move irregularly in a sense that they are not attracted to a periodic point. This suggests the presence of a "strange attractor", which we shall refer to as S, that possesses a fractal structure, with an infinite number of saddles associated with the original sinks and a countable infinity of periodic points due to the homoclinic intersections of the stable and unstable manifolds.

Holmes [3] also observed stable attracting motions of Period 5 instead of strange motions for certain parameters. Finally, for much larger forcing parameters a sink and a saddle appear 'outside' of the homoclinic points and S, meaning that as $t \to \pm\infty$ the orbits will once again be periodic as they are attracted towards the sink. (See figure 2.2.5 in [2])

5.3.2 Results from experiment

We present the results of experimental data for $f = 10.43$ Hz. The focus will be to investigate the "strange attractor" motions that were described in the previous paragraph.

Using the experimentally-derived values of α and β given in figure 4.6 where $\alpha = 1.161 \times 10^4$ and $\beta = 1.172 \times 10^8$, we use equation 5.3.1 to calculate that $P_c = 3.6232$, or equivalently $(A_0)_c = 0.54$ mm. Remember that this is the forcing amplitude at which homoclinic points theoretically start to appear, but is lower than the forcing amplitude at which sustained strange attractor motions occur. Since the electromagnetic shaker has a maximum forcing amplitude of 6 mm, we are confident that we can observe at least transient chaotic motions before the orbit is attracted to one of the sinks, or perhaps even strange attractor motions.

For a lower forcing amplitude of $A_0 = 2.98 \pm 0.05$ mm (or $P = 20.04$), the experimental orbits are similar those presented in figure 5.1, where we have periodic small-amplitude oscillations around one of the equilibrium points, depending on the initial conditions. However, large-amplitude oscillations between both equilibrium points were not stable and eventually decayed to small-amplitude oscillations.

For a higher forcing amplitude of 3.95 ± 0.05 mm (or $P = 26.57$), we observe occurrences of transient chaotic motions as the beam displays irregular motions for 25-35 seconds when perturbed before settling into sustained periodic motion, similar to the predicted behaviour from Duffing oscillator theory. We do not observe transitions from periodic motion into irregular motions. The transition from chaotic to periodic motion is shown in figure 5.3 and the Poincaré map is shown in figure 5.4. From the Poincaré map in figure 5.4, we see that the orbit wanders along the structure of the strange attractor before being eventually attracted to a sink of Period 2. (Contrast the 'outline' of the initial transient chaotic orbit to the structure of the Strange Attractor presented later in figure 5.6)

Note that the points on the Poincaré map are coloured such that points that are sampled earlier in the time series are ‘colder’ colours, and points sampled later are ‘hotter’ colours. The order from earliest to latest is dark blue → light blue → light green → yellow → orange → red → dark red.

If we now increase the forcing amplitude to 4.31 ± 0.05 mm (or $P = 28.99$), we observe irregular motions which were sustained for over 4 hours, or roughly 1.35×10^5 forcing periods. An example of these irregular beam tip motions is presented in figure 5.5, and the corresponding Poincaré map is shown in figure 5.6. The Poincaré map is taken over the first 2 hours of the experimental data (and not the whole 4 hours) to reduce Poincaré map errors due the forcing frequency drift as described in the previous section.

The structure of the strange attractor in figure 5.6 is similar to those investigated by Holmes [1],[3]. We see that there are certain areas on the Poincaré map that display obvious colour gradients. Due to the finite width of points, later time points will be superimposed upon earlier time points as the Poincaré map rendered, and thus it is possible for ‘hotter’-coloured points to obscure ’cooler’-coloured points, but not vice-versa. See figure 5.11 below for an example of this in a Poincaré map computed using numerical simulations of the full model. Thus, the existence of colour gradients indicates that there is some frequency drift in the forcing frequency over time, resulting in a slight shift of the strange attractor due to the Poincaré map sampling frequency being slightly different than that of the forcing frequency. Nevertheless, we see that this slight shift does not significantly alter the structure of the strange attractor. Unfortunately, experimental error constraints combined with this frequency drift limit the resolution at which we can view the strange attractor, and hence magnification of figure 5.6 does not yield any further appreciable structure.

We also compute the natural logarithm of the FFT power spectra from the time series. The power spectra peaks at $f = 10.46$ Hz, which is close to the forcing frequency of 10.43 Hz. Furthermore, we find that the power spectra decays exponentially with f, as evidenced from a linear fit of the log power spectra with frequency, presented in figure 5.7. This is in agreement with the theory presented by Brunsden and Holmes [17] for power spectra of strange attractors near homoclinic orbits.

In conclusion, we find that the experimental data is consistent with Duffing oscillator theory as we increase the forcing amplitude. We next present results using the numerical simulations of the computational full model.

5.3.3 Results from numerical simulations

We present a bifurcation diagram using simulations of the full computational model. A_0 is varied from 0.1 cm to 1.7 cm (or equivalently P is varied from 6.73 to 114.3) for a fixed

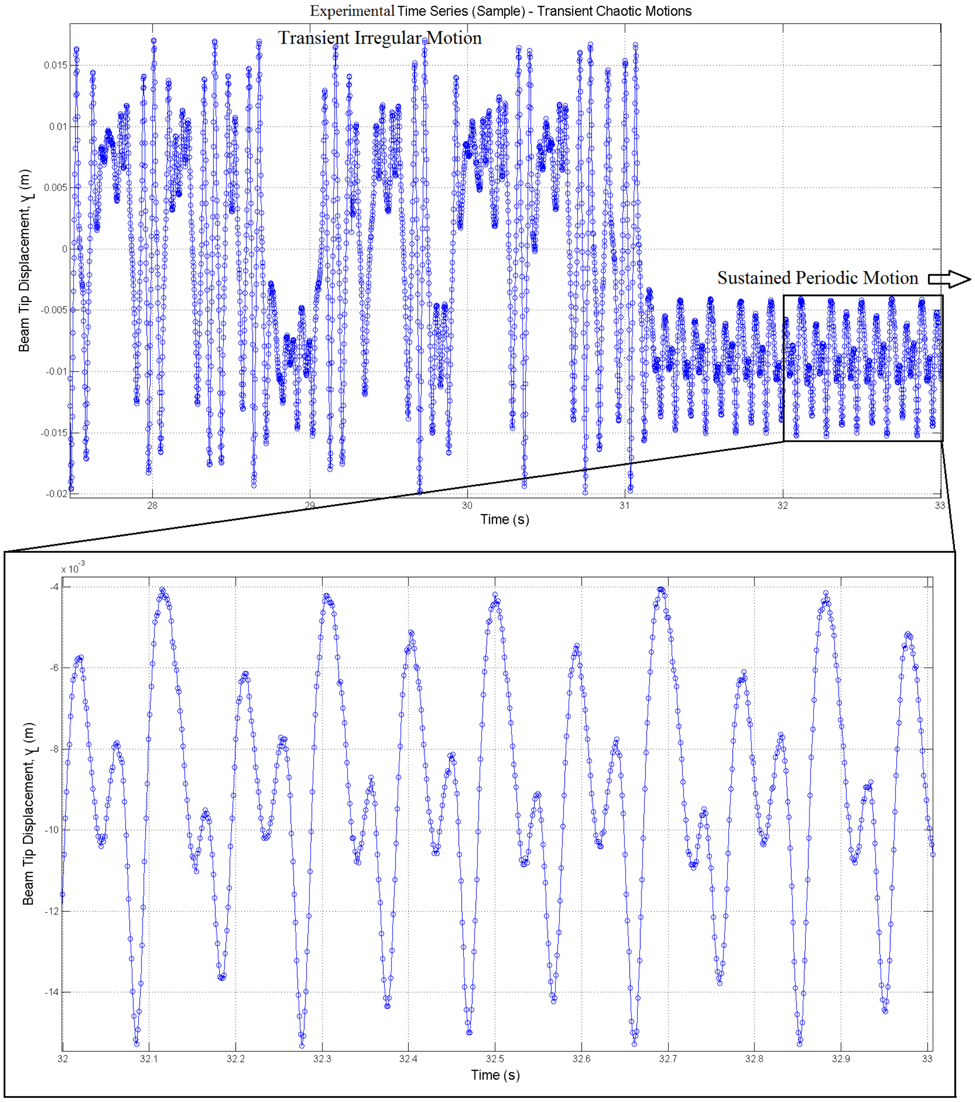

Figure 5.3: Experimental (Sample) Time Series : Transition from chaotic to periodic motion (period 2) after 31 seconds, with $A_0 = 3.95$ mm and $f = 10.43$ Hz, correspondingly $P = 26.57$. Magnified region shows period-2 orbit.

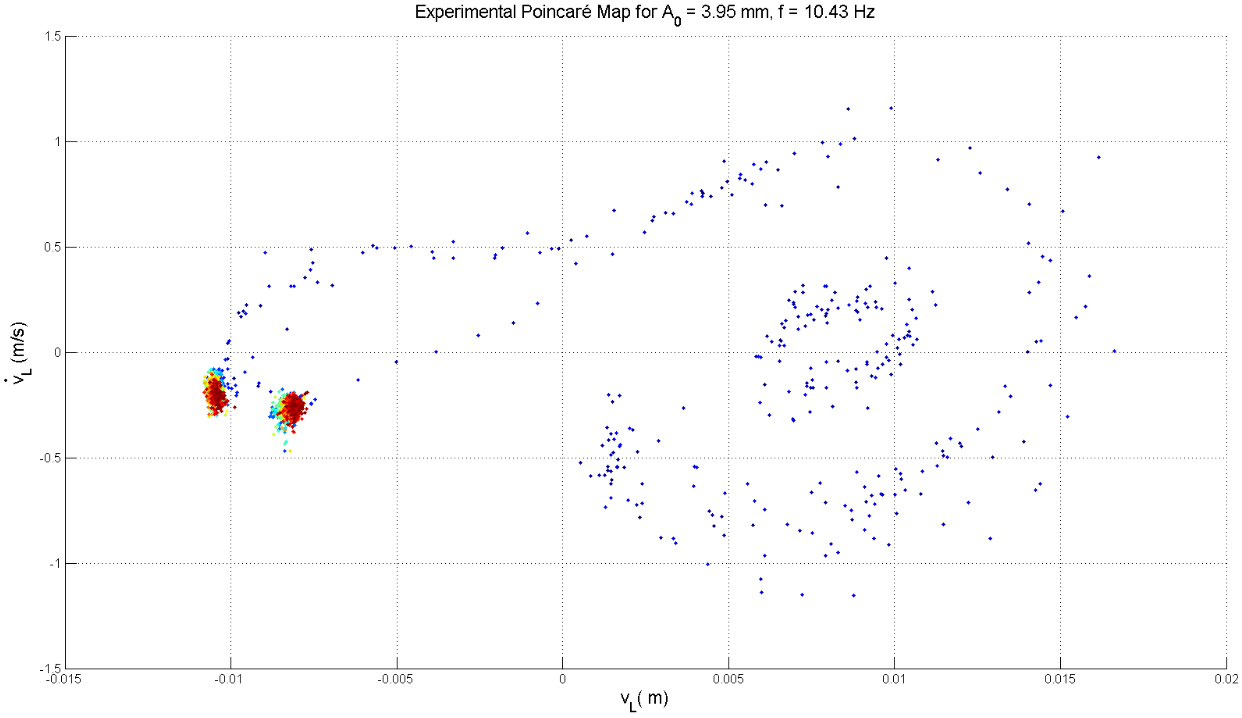

Figure 5.4: Experimental Poincaré map from experimental data with $A_0 = 3.95$ mm and $f = 10.43$ Hz : Transition from chaotic to period-2 motion. "Colder" colors indicate points taken earlier in the time series,"hotter" colors indicate points that are taken later.

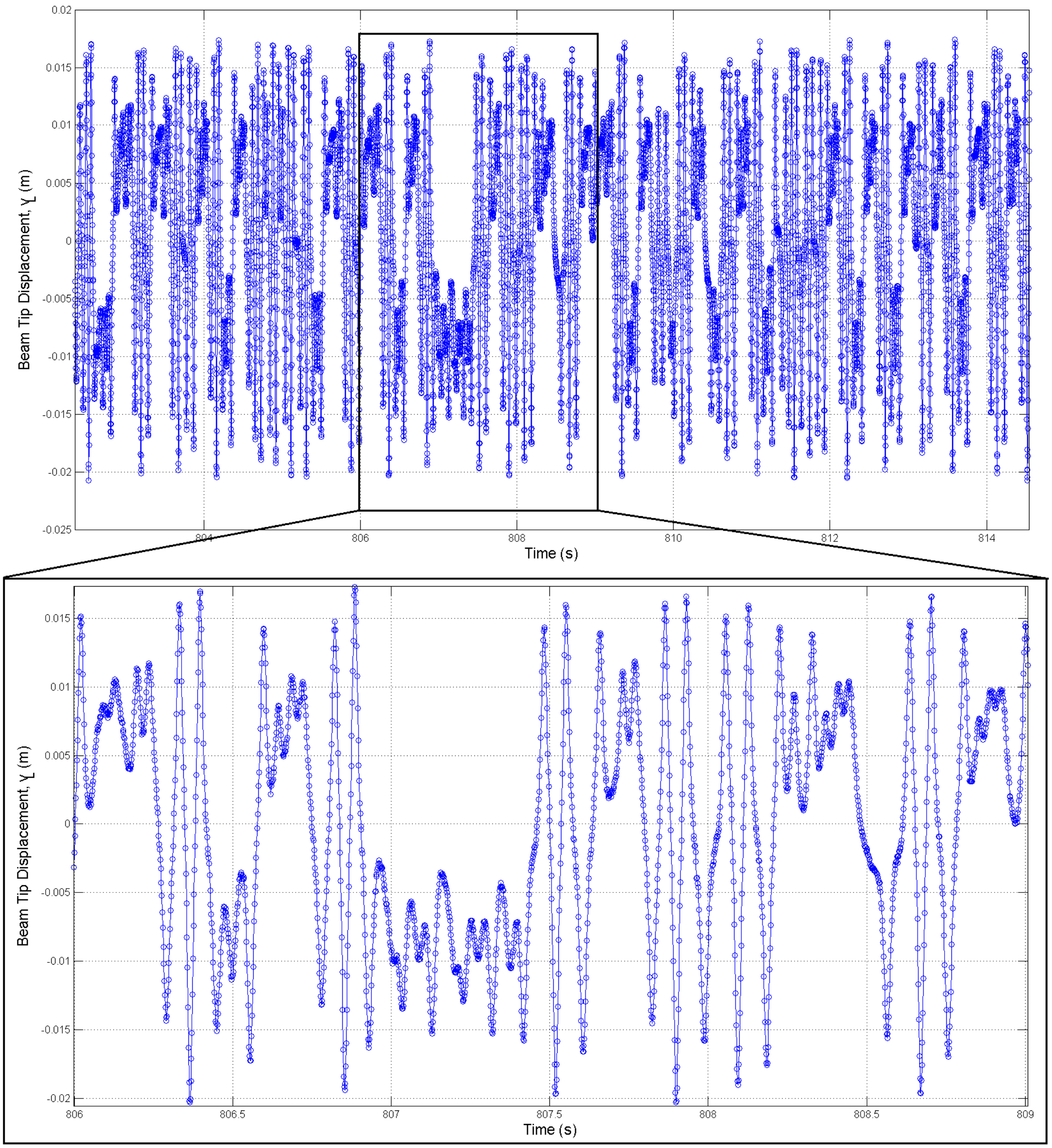

Figure 5.5: Experimental (Sample) Time Series : Irregular Motions for $A_0 = 3.95$ mm and $f = 10.43$ Hz, correspondingly $P = 28.99$. Magnified region shows motions over a smaller time scale.

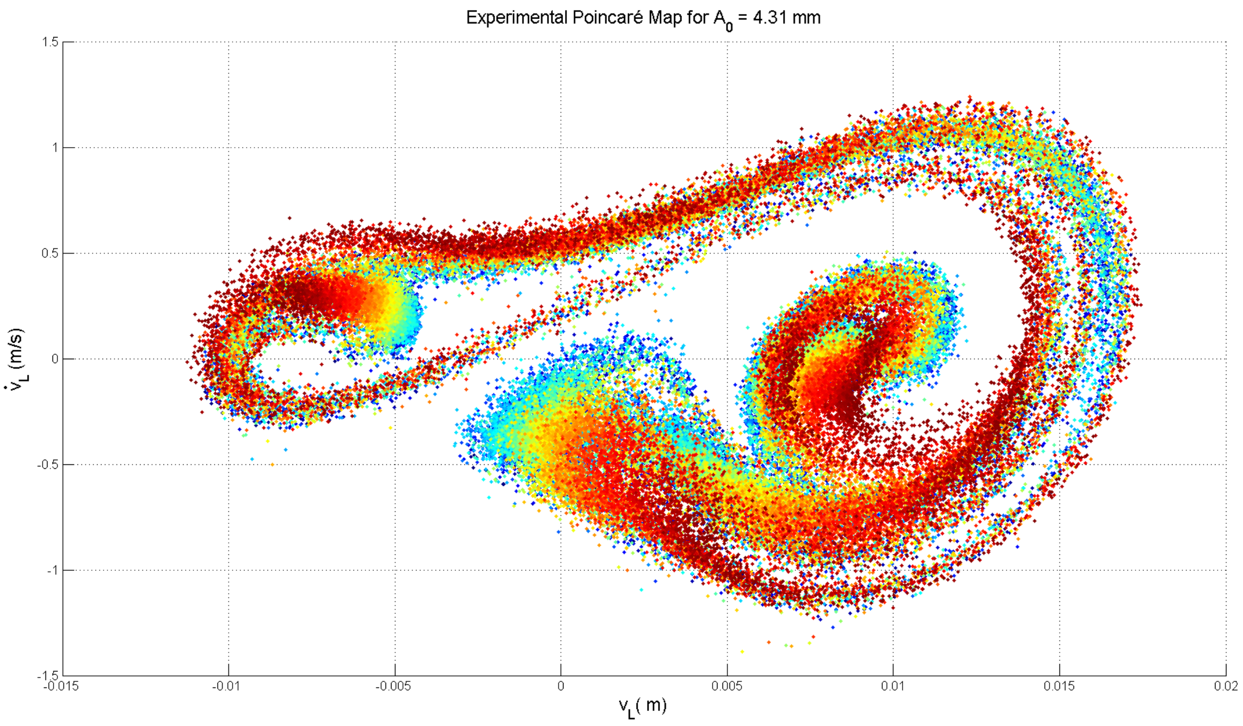

Figure 5.6: Experimental Poincaré map from experimental data with $A_0 = 3.95$ mm and $f = 10.43$ Hz taken over 2 hours. "Colder" colors indicate points taken earlier in the time series, "hotter" colors indicate points that are taken later. Presence of color gradients indicates slight shift in forcing frequency, resulting in a slight shift in the structure of the strange attractor.

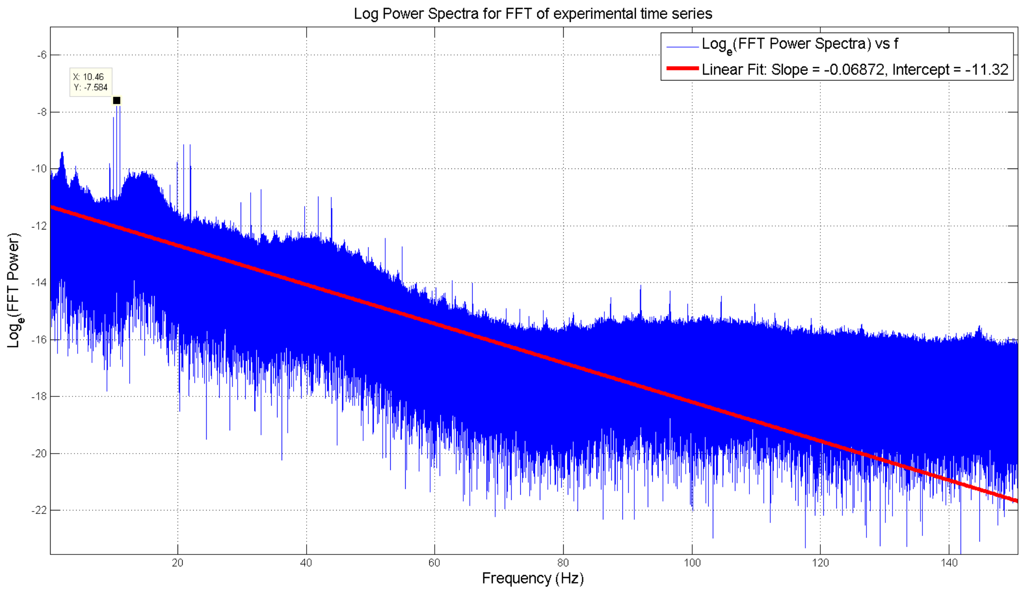

Figure 5.7: Logarithm of power spectra for time series corresponding to strange attractor motions. Linear fit is taken over $0 \leq f \leq 80$ Hz.

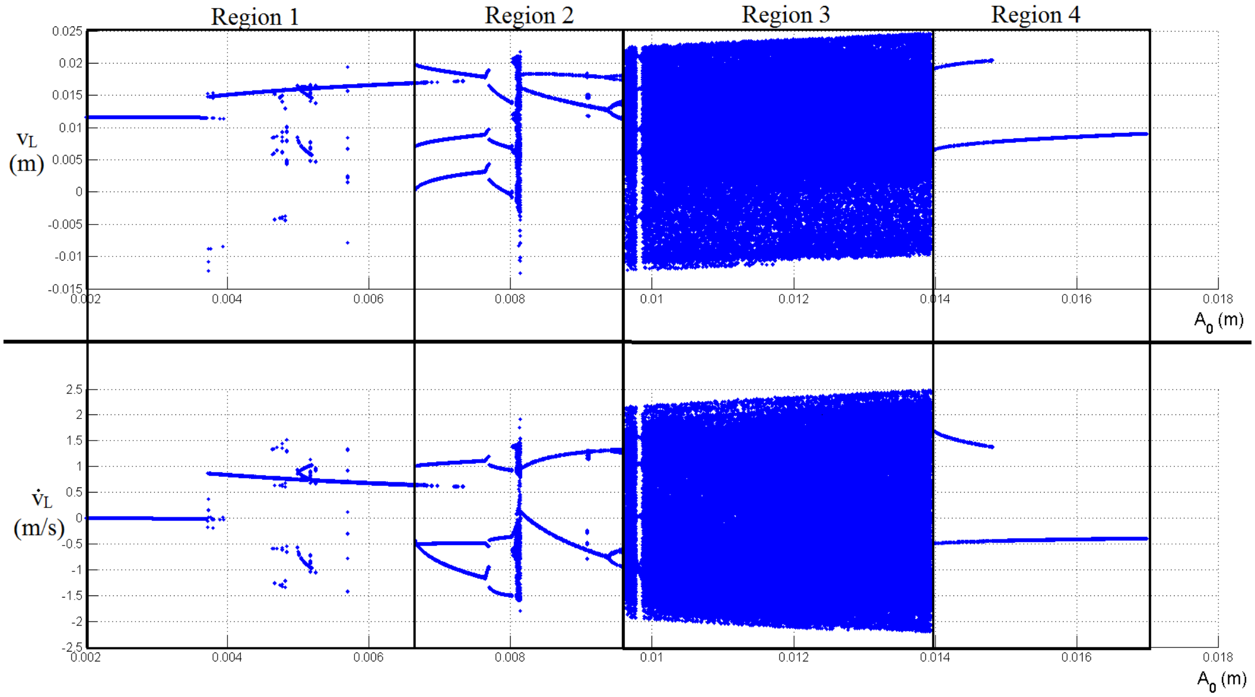

Figure 5.8: Poincaré Map components as A_0 is increased for the full computational model.

forcing frequency of 10.43 Hz, and the Poincaré map is computed from the resulting time series simulation for each A_0. Here $d = 3.93$ cm with zero offset. The initial conditions for each case are $v_L(0) = 1$ cm , $\dot{v_L}(0) = 0$. Each case is simulated for 100 seconds, but the Poincaré map is taken over the last 20 seconds of the simulation (207 forcing periods) to exclude transients. For computational efficiency we use 5000 nodes over v_L instead of 20000 when computing the bifurcation diagram. We plot the v_L and $\dot{v_L}$ components of the Poincaré map as A_0 is varied in figure 5.8. The various regions indicated in figure 5.8 will be referenced in the following discussion.

We feel that it is important to point out the limitations associated with the methods used to compute the bifurcation diagram in figure 5.8. Unlike the bifurcation diagrams presented in section 4.3, chapter 4 where all fixed points of the system and their corresponding stabilities are determined by the zeros and their corresponding slopes of the one-dimensional function F_{static} (which is easily computed), finding the fixed points of the Poincaré map involves computing the Poincaré map for points over the two-dimensional plane Σ, and so the associated computational complexity is higher due to the higher dimensionality of the problem. Furthermore, the full model is not amenable to analytic methods due to its numerical definition, and thus numerical detection of the fixed points of the Poincaré map as well as numerical estimation of their corresponding eigenvalues will be required.

In place of calculating the Poincaré map for a grid of points over Σ and having to deal with numerical methods to detect the fixed points and their stabilities, we choose an alternate method of picking an initial point on Σ (we choose $v_L(0) = 1$ cm, $\dot{v_L}(0) = 0$), numerically simulating the system using the full model over a long period of time and recording the intersections of the resulting trajectory with Σ. This will give us a 2-D orbit of points given by the Poincaré Map over Σ. Although this method is more straightforward, there are several limitations to it, since

1. we will not be able to locate any fixed points of the Poincaré Map that have unstable components (eigenvectors with eigenvalues having modulus > 1) such as saddle points, since the orbits will either settle into a sink of period k (k some positive integer) or end up moving around on a strange attractor structure, and
2. if an orbit settles into a sink of period k, we will not be able to detect any other sinks with periodic orbits associated with the Poincaré Map due to the orbit already being at the stable sink of period k.

The first limitation means that we will not be able to see any saddle points on the bifurcation diagram. The effect of this is that fixed points on the bifurcation diagram will sometimes seem to disappear and appear as a parameter is increased, whereas the actual situation is such that they are being created and annihilated by saddle-node bifurcations. This is seen from the abrupt "jump" in the branch of fixed points in region 1, as well as the appearance of higher-period orbits for certain parameters in region 1. See figure 5.9 for clarification of this.

The second limitation means that a branch of fixed points will appear to bifurcate into two branches of fixed points via period-doubling, with one branch of period k visible on the bifurcation diagram but the other branch will be missing. In actuality, the missing branch is associated with another sink of the same period k that the orbit is not attracted to. See figure 5.10 for clarification of this.

Thus, the bifurcation diagram in figure 5.8 represents an incomplete bifurcation diagram in the sense that we can only determine how the period of a single sink changes as the parameter is varied due to the method we chose to compute the Poincaré maps. Even in the presence of such limitations, the bifurcation diagram in figure 5.8 provides enough information for us to visualize how the orbit structure of the Poincaré Map changes as the parameter is varied.

We see that the bifurcation diagram can be separated into sections that roughly correspond to how the structure of the Poincaré Map of the Duffing oscillator changes as A_0 is increased, as described in the beginning of this section. Region 1 corresponds to lower forcing

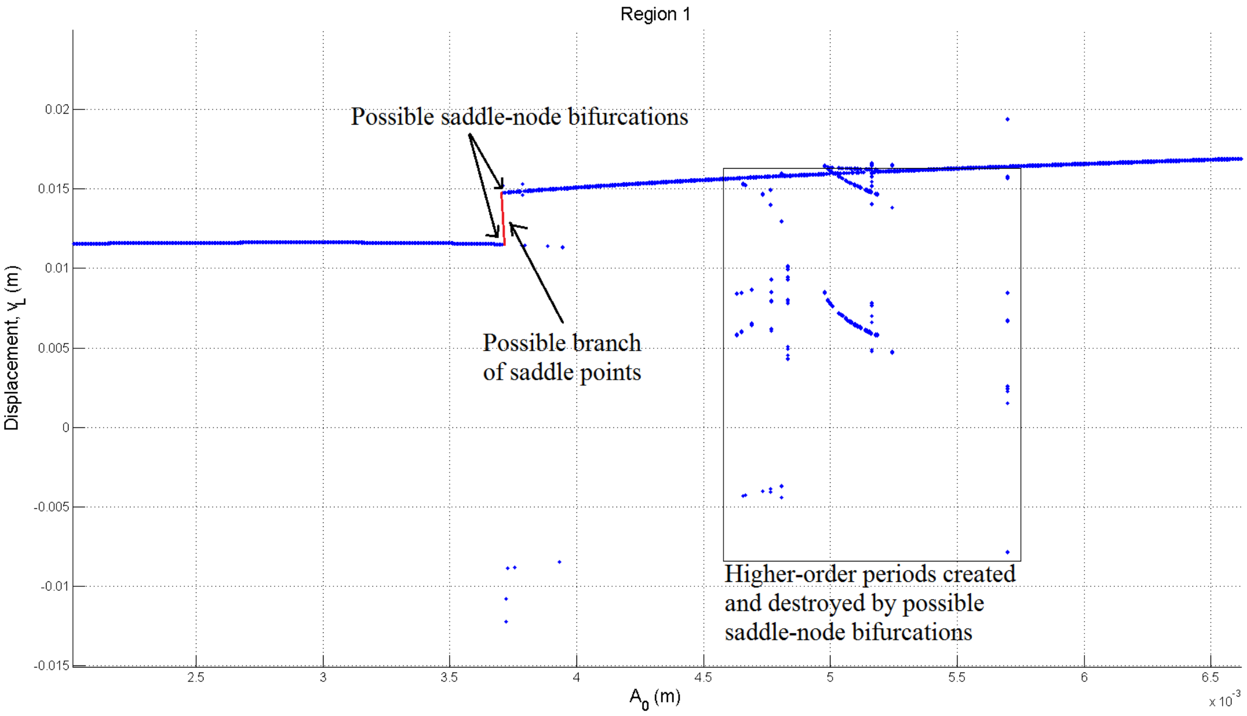

Figure 5.9: Possible saddle-node bifurcations in region 1 of bifurcation diagram, with a possible branch of saddle points shown in red. Appearance and subsequent destruction of higher-period orbits for certain parameters indicate presence of "unseen" branches of saddle points in bifurcation diagram.

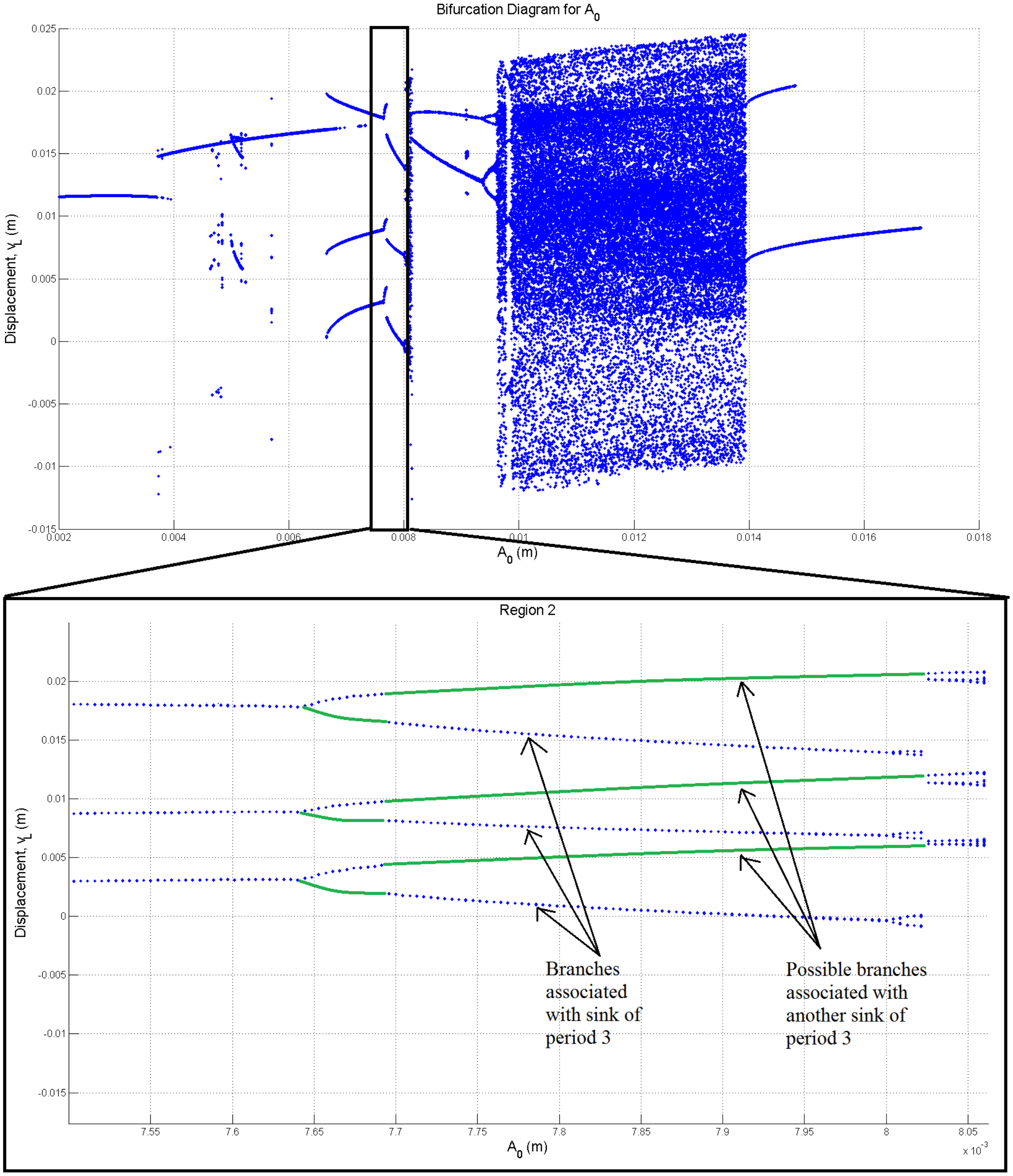

Figure 5.10: Magnification of region of bifurcation diagram where possible missing branches of fixed points from period-doubling bifurcations (indicated as green lines) are located.

amplitudes where there are still two stable sinks in the Poincaré Map, hence the orbits are of Period 1. We see that there are certain points where higher-period orbits can occur due to saddle-node bifurcations.

Region 2 corresponds to the sinks bifurcating into saddles and increasing the number of sinks on the Poincaré Map. This is seen from the existence of Period 2,3 and 4 orbits on the Poincaré map. The bifurcation diagram suggests that parameters in the middle of section 2 (between 8 and 8.2 mm) might give rise to a Strange Attractor on the Poincaré Map, but examining the actual Poincaré map for those parameters reveal that they are actually high-period orbits with no strange attractor structure. This emphasizes the fact that the bifurcation diagram is really an attempt at visualizing a 3-D structure, and the actual Poincaré Map should be checked to make sure that the orbits on the Poincaré Map correspond to what is expected from theory.

Region 3 corresponds to strange attractor motions, giving rise to the strange attractor S on the Poincaré map. In order to better visualize the strange attractor, the Poincaré map is shown in figure 5.11 for $A_0 = 1.2$ cm, and also magnification of the strange attractor to emphasize the fractal nature of the structure. The Poincaré map was generated by simulating a time series for 90000 seconds using the full model.

Furthermore, there is a “window of stability” in region 3 where there are period-5 orbits instead of strange-attractor motions, similar to the description given by Holmes in [3]. See figure 5.12 for a magnification of the bifurcation diagram. The Poincaré map for a period-5 orbit is shown in figure 5.13.

Finally, section 4 corresponds to a large enough forcing where the motion is periodic once again as the orbits are attracted towards the sink that appears ‘outside’ the homoclinic points.

Thus, we see that the experimental data as well as the full computational model support the idea of irregular motions of the beam tip which give rise to a strange attractor structure of the corresponding Poincaré Map, as suggested from the theory of the Duffing oscillator. Furthermore,the experimental data as well as the bifurcation diagrams produced using the full model are consistent with the bifurcations described by Holmes for the Duffing oscillator (which is a simplification of the full model), indicating that the cubic approximation for F_{static} used for Duffing’s oscillator models the original, more complex magneto-elastic system well.

We note that although both experimental data and numerical simulation agree with the theory for the forced Duffing Oscillator as the forcing amplitude is increased, there is a discrepancy between the experiment and the full model in that the forcing amplitudes required for transient chaos and chaotic motions for the full model are larger than that observed experimentally. The full model predicts that forcing amplitudes of at least 9.6 mm are required

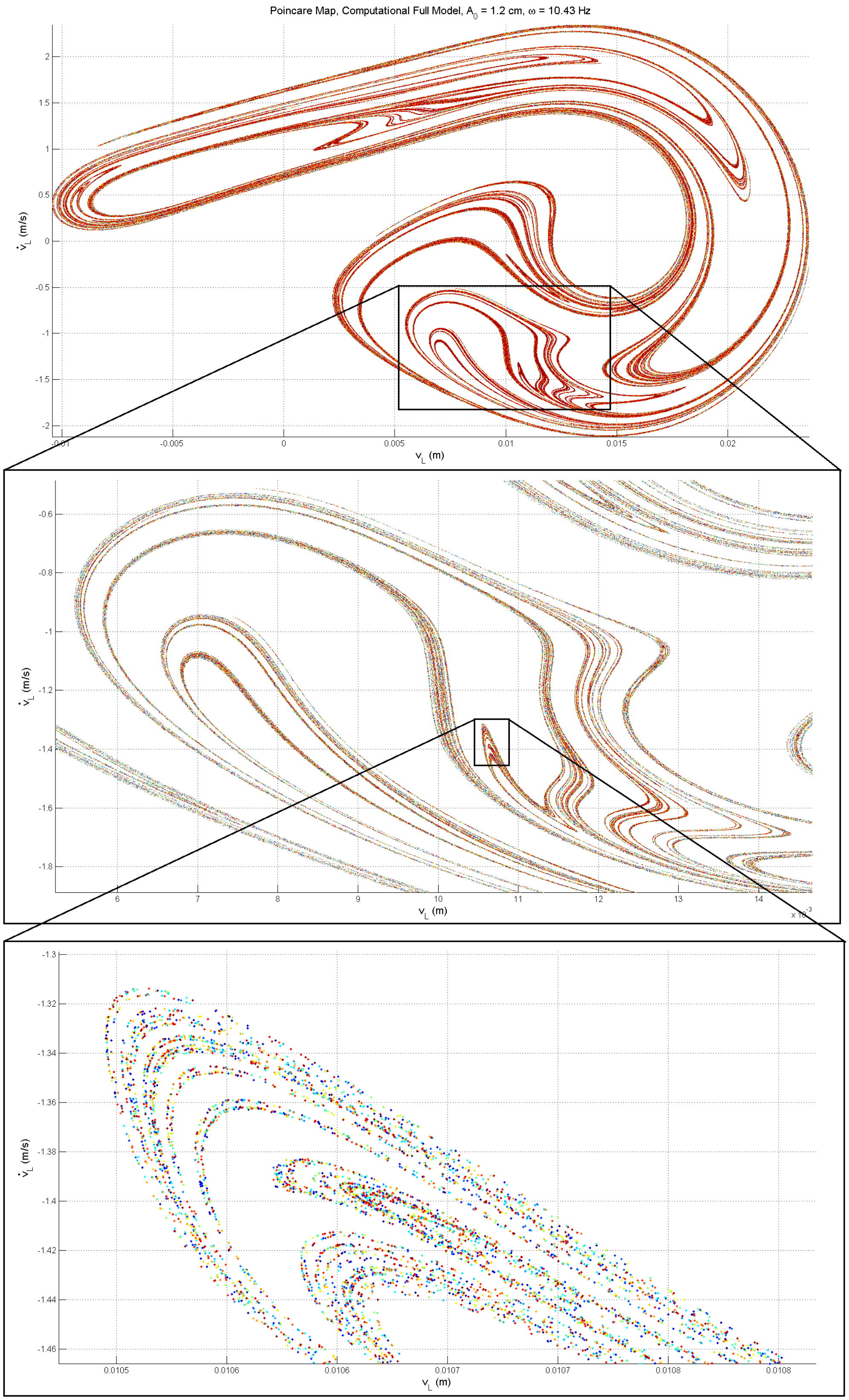

Figure 5.11: Poincaré Map for $A_0 = 1.2$ cm and $f = 10.43$ Hz from numerical simulations of the full model and magnifications of the resulting strange attractor structure to emphasize the fractal features.

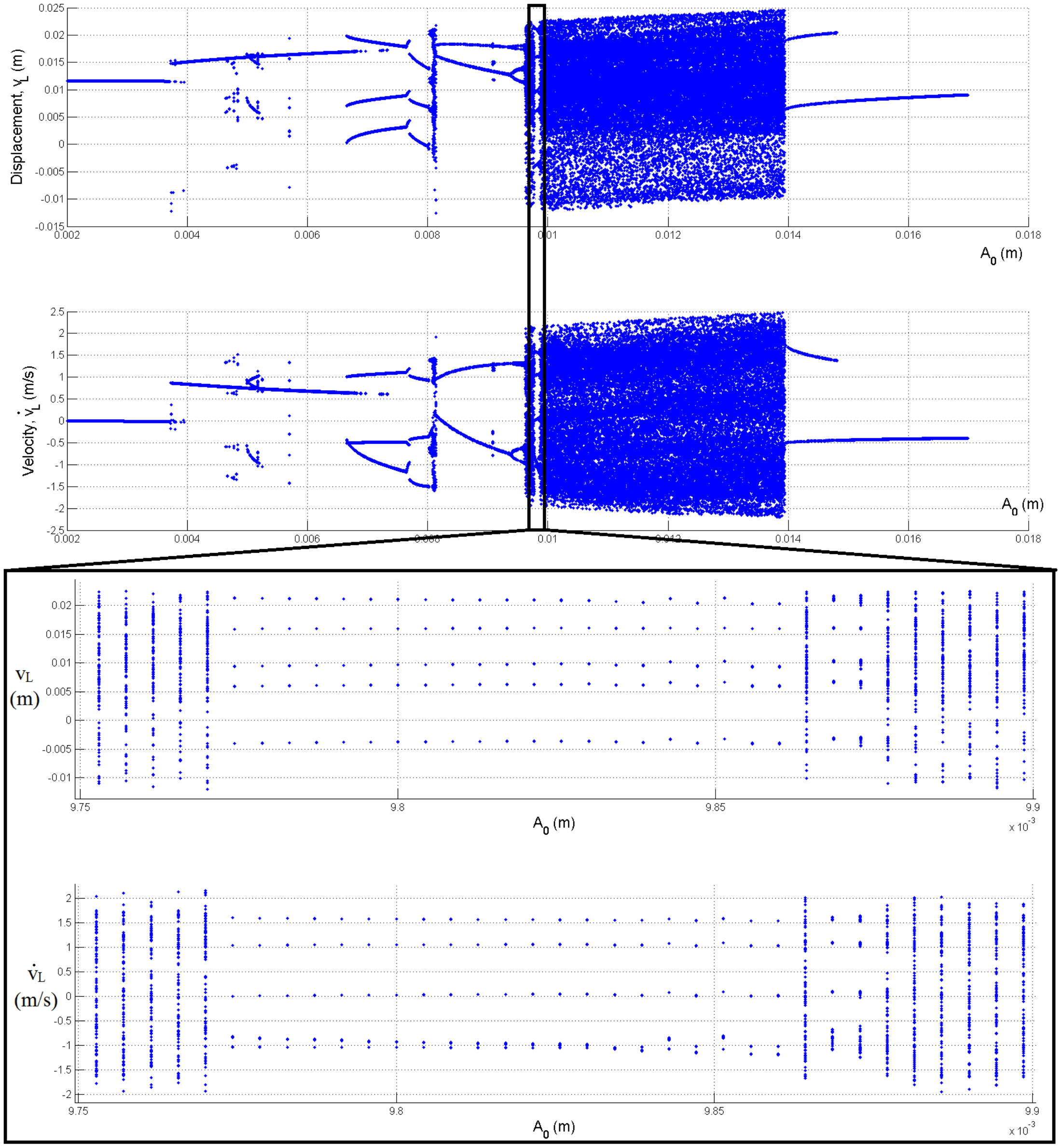

Figure 5.12: Magnification of bifurcation diagram for 9.75 mm $\leq A_0 \leq$ 9.9 mm, showing a parameter "window of stability" of period-5 orbits amidst parameters which give rise to chaotic motions.

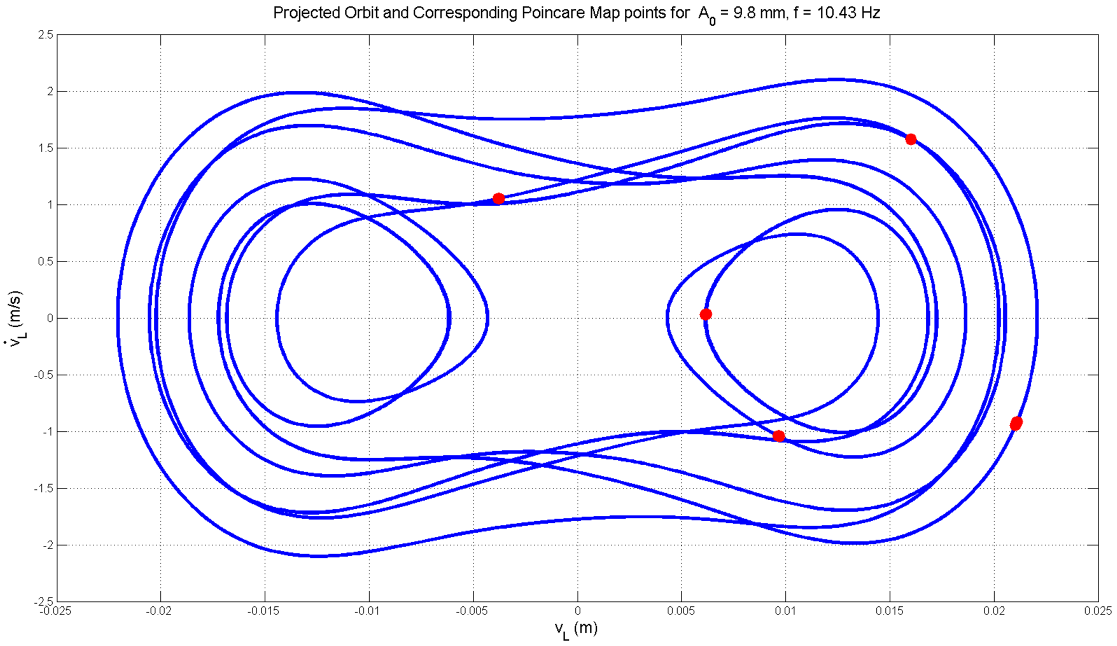

Figure 5.13: Projected orbits (blue) and corresponding Poincaré Map points (red) from numerical Simulations : Full Model with $A_0 = 9.8$ mm and $f = 10.43$ Hz.

for sustained irregular motions/orbits along a strange attractor, but experimentally we found that a forcing amplitude of 4.31 mm was enough to induce such motions. It could be possible that the experimentally-observed irregular motions were long transients, but other possible reasons for the discrepancy include lateral oscillations on the apparatus from the shaker due to imperfect fabrication of the mainframe as well as the bifurcation diagram of the full model not taking into account the asymmetric case where the magnets are not perfectly symmetric with respect to the vertical beam position. Although the full model's predictions do not match the experimental data closely, it is still useful in exploring possible bifurcations of the system as certain parameters are varied. A last example of this is presented below.

5.4 Bifurcations for varying magnetic field strengths

A bifurcation diagram is presented in figure 5.14 for increasing magnet strengths $B_{surface}$ (while keeping the magnet strengths of both magnets equal), and a forcing amplitude of $A_0 = 9.8$ mm (or $P = 65.9$) with frequency $f = 10.43$ Hz. The computational setup is the same as that of the bifurcation diagram for increasing A_0. We see roughly the same behavior as for when the forcing amplitude is increased. As $B_{surface}$ is increased, a Period-1 orbit bifurcates into a Period-3 orbit, and later on period-doubling bifurcations occur until we reach a region where chaotic motions occur. Some branches of the fixed points from the

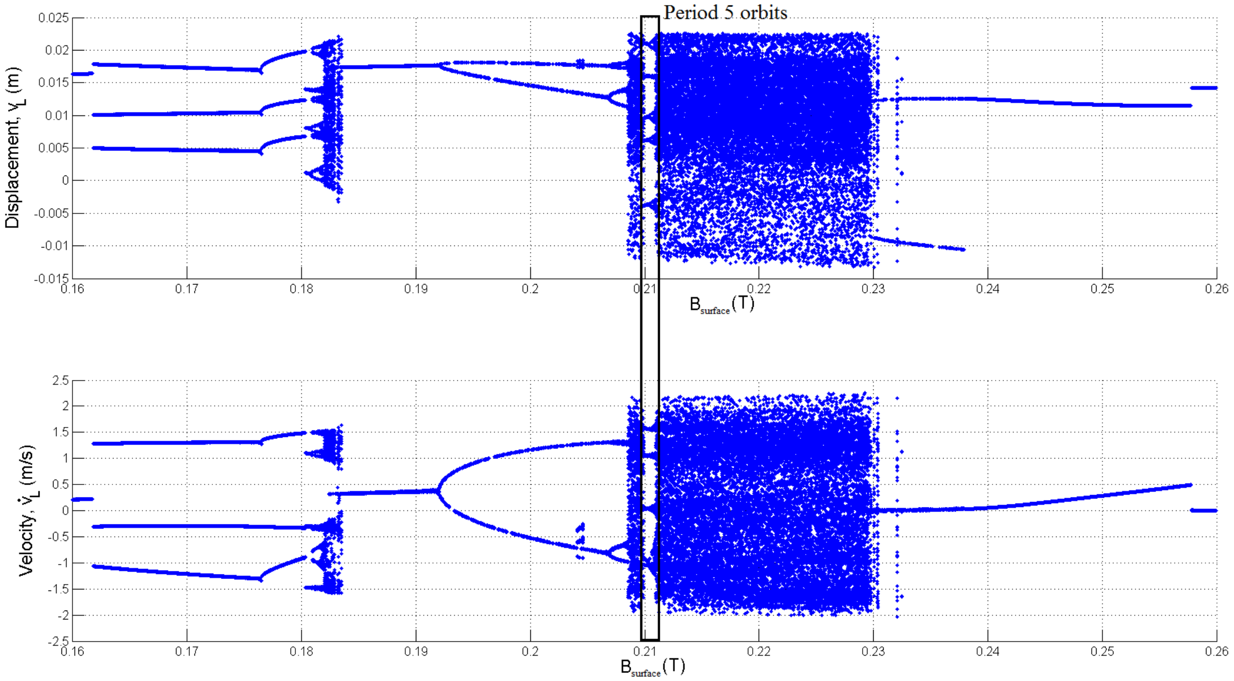

Figure 5.14: Bifurcation diagram for increasing magnetic field strengths for $d = 1.39$ cm, $A_0 = 9.8$ mm and $f = 10.43$ Hz. The parameter window of stability of period-5 orbits amidst parameters which give rise to chaotic motions is indicated.

bifurcations are missing due to reasons given in subsection 5.3.3. We also observe a ‘window of stability’ where period-5 orbits occur instead of chaotic orbits.

Thus, we see that the full model is useful in studying the bifurcations of the system as physical parameters are varied. It is possible to generate bifurcation diagrams for other physical parameters such as beam dimensions or magnet dimensions.

Chapter 6

Summary and Conclusion

We have developed a computational model for the magneto-elastic system consisting of a cantilevered beam placed in a non-uniform magnetic field created by two cylindrical magnets. The computational model is based on physical parameters as inputs, and this was achieved by combining the governing ODE for the modal amplitude of the beam with a numerical solution to find the magnetic field for any given point along and near the beam. The main result is the computation of all the terms involved in the static case as given in equation 2.1.6. A term can then be added onto the ODE to account for periodic forcing of the whole system.

We have also constructed an experimental setup of the system in order to compare the results obtained from experiment with those from the computational model. We also check our results against the theory for a Duffing oscillator, which models the system well if the system is in a double-well potential. In the static case, the experimental results agree with the results from the computational model to within experimental error. In the case of sinusoidal forcing of the system, the computational model does not quantitatively display as good an agreement with the experimental results as that of the static case, but still agrees well with Duffing oscillator theory in terms of qualitative changes in the orbits of the Poincaré Map that occur as the forcing parameter is increased.

The computational model is more flexible in the sense that we are able to investigate the behaviour of the system by varying physical experimental parameters, and hence allowing us to create bifurcation diagrams and bifurcation sets such as those presented in section 4.3. Double-well and triple-well potentials were observed in the computational model as a physical parameter such as magnet spacing was increased, and this was observed experimentally as well. More importantly, the computational model also enables us to visualize the orbits of the periodically-forced system via the Poincaré Map as the system parameters are increased, allowing for the estimation of parameters which would gives rise to chaotic orbits. Such a model would be a useful tool in aiding the design of magneto-elastic systems such as magnetic levitation transportation system [25] prior to their construction.

However, the way that the computational model is defined numerically also makes it not amenable to analytic methods. In some cases the system is well-modelled by a cubic or cubic-quintic Duffing oscillator, whose dynamics have been analyzed [3] and for which analytical approximate solutions are known [26]. It might be possible to treat the problem analytically by examining the equation that results by substituting the equation for the magnetic field that involves elliptic integrals into the governing ODE for the modal amplitude, but we suspect that the resulting problem will be no easier to solve.

Among possible future work that could be undertaken in continuation of the work presented here would be to design a control scheme based on physical system parameters to stabilize periodic orbits. Such control of chaos based on delayed linear feedback using forcing frequency as a control parameter has already been investigated by Hikihara and Kawagoshi [16], and so it might be possible to use the computational model that has been presented here to simulate the system with a physical parameter (such as the ratio of the magnetic strength of one magnet to the other).

On the same note, another possible avenue would be to consider the system as the magnetic field strengths are varied periodically in time. This would be similar to investigating the physical system where the cantilevered ferromagnetic beam is placed between two solenoids through which alternating currents (AC) are being passed through them, with the alternating currents not necessarily having the same phase. After all, the computational model already approximates the cylindrical magnets as ideal solenoids. This periodic variation in magnetic field strengths can be interpreted as another external source of periodic forcing on the system, only that this forcing directly affects F_{static} as presented in equation 2.1.6 instead of being an external forcing term such as $Pcos(\omega t)$. Such a setup would have several parameters that would lend themselves to investigation such as the amplitudes, frequencies and relative phases of the variations of the magnetic field strengths of both magnets. It would also be interesting to compute the orbits of the system in the presence of both variations in magnetic field strengths as well as external forcing of the system. Since the computational model demonstrated good qualitative agreement with experiment and theory in the cases studied here, we would expect the same as well when considering such variations in magnetic field strengths.

References

[1] F.C. Moon and P.J. Holmes 1979 *Journal of Sound and Vibration* **65** (2), 275-296. A Magnetoelastic Strange Attractor.

[2] J. Guckenheimer, P.J. Holmes 1983 *Applied Mathematical Sciences* 42. Nonlinear Oscillations, Dynamical Systems, and Bifurcations of Vector Fields.

[3] P.J. Holmes 1979 *Philosophical Transactions of the Royal Society (London).* A nonlinear oscillator with a strange attractor.

[4] P.J. Holmes and J.E. Marsden 1978 *Automatica* **14**, 367-384. Bifurcations to divergence and flutter in flow-induced oscillations: an infinite-dimensional analysis

[5] P.J. Holmes 1979 *Proceedings on 1978 IEEE Conference on Decision and Control, Paper W A7*, 181-185. Global Bifurcations and chaos in forced oscillations of buckled structures.

[6] N. Derby and S. Olbert 2010 *American Journal of Physics* **78** (3), 229. Cylindrical magnets and ideal solenoids.

[7] F.C. Moon 1939 *Wiley-VCH* Chaotic Vibrations: An introduction for Applied Scientists and Engineers.

[8] T. Kanamaru 2008 *Scholarpedia* **3** (3):6237 Duffing Oscillator.

[9] F.C. Moon and Y.H. Pao 1968 *Journal of Applied Mechanics* **35**, 53-58. Magnetoelastic buckling of a thin plate.

[10] F.C. Moon and Y.H. Pao 1969 *Journal of Applied Mechanics* **36**, 92-100. Vibration and dynamic instability of a beam-plate in a transverse magnetic field.

[11] F.C. Moon 1978 in emphMechanics Today **4** Chapter V, Problems in magneto-solid mechanics.

[12] S. Whitney 1999 http://emweb.unl.edu/Mechanics-Pages/Scott-Whitney/325hweb/Beams.htm. Vibrations of Cantilever Beams: Deflection, Frequency and Research Uses.

[13] C. Gonzálze and J. Llorca 2005 *Int. J. Solids and Structures* 42 1537-1545. Stiffness of a curved beam subjected to axial load and large displacements.

[14] S.H. Strogatz 1994 *Perseus Books Publishing* Nonlinear dynamics and chaos

[15] Kalmar-Nagy and Balachandran 2011 emphJohn Wiley & Sons (5), 140-173. Forced harmonic vibration of a Duffing Oscillator with linear viscous damping.

[16] Hikihara and Kawagoshi 1996 *Physics Letters* **A** 211 29-36 An experimental study on stabilization of unstable periodic motion in magneto-elastic chaos.

[17] V. Brunsden and P.J. Holmes 1987 *Physical Review Letters* **58** (17) 1699-1702. Power Spectra of strange attractors near homoclinic orbits.

[18] M.T. Heath 2001 *McGraw-Hill* Scientific Computing: An introductory survey.

[19] S.J. Farlow 2006 *Dover Publications, Inc.* An introduction to differential equations and their applications.

[20] K.D. Hjelmstad 2005 *Springer Science* Fundamentals of Structural Mechanics

[21] N.J. Kasdin 2011 *Princeton University Press* Engineering Dynamics: A Comprehensive Introduction.

[22] D. Kleppner and R.J. Kolenkow *McGraw-Hill* An Introduction to Mechanics

[23] T. Poston and I. Stewart 1978 *Catastrophe Theory and its Applications.* London:Pitman.

[24] V.K. Melnikov 1963 *Transactions of the Moscow Mathematical Society* **12**, 1-56. Stability of center to time periodic perturbations.

[25] F.C. Moon 1977 *Proceedings of the Conference on Noncontacting Suspension and Propulsion Systems for Advanced Ground Transportation*, MIT. Printed by the U.S. Department of Transportation. Static and dynamic instabilities in mag-lev model-experiments.

[26] A. Beléndez , M. L. Alvarez, J.Fracés et al., 2012 emphJ. of Applied Mathematics **12** Article ID 286290. Analytical Approximate Solutions for the Cubic-Quintic Duffing Oscillator in Terms of Elementary Functions.

[27] Feng, Chen and Hsu 2005 *Applied Mathematics Seminar* University of Texas-Pan American, Edinburg, TX. A Qualitative Study of the Damped Duffing Equation and Applications

[28] R.H. Rand 2005 Dept. Theoretical and Applied Mechanics, Cornell University, Ithaca NY. Lecture Notes on Nonlinear Vibrations.

[29] J.E. Berger and G. Nunes Jr. 1997 emphAm. J. Phys. **65** (9) 841-846. A mechanical Duffing oscillator for the undergraduate laboratory.

[30] Moosbrugger and Cverna 2000 *ASM International* Electrical and Magnetic Properties of Metals.

[31] Hikihara, Tuono and Kawagoshi 1997 *Int. J. of Bifurcation and Chaos* **7** (12) 2837-2846. Experimental Stabilization of unstable periodic orbit in magneto-elastic chaos by delayed feedback control.

[32] J.M. Gonzalez-Miranda 2004 *Imperial College Press*. Synchronization and Control of Chaos.

Appendices

Appendix A

Derivation of the governing PDE for the beam displacement $v(t)$ using linear beam theory and differential elements

Consider a differential beam element with uniform cross-sectional area shown in figure A.1. The differential element has differential arc-length ds, and is subject to body forces F_x, F_y and body moments C. One end of the element (labelled side 1) has a vertical displacement v from the x-axis, with given directions of shear Q and axial force T as well as moment M defined in a positive direction. The other end of the element (labelled side 2) has a vertical displacement $v + dv$ from the y-axis, with given directions of differential shear $Q + dQ$, axial force $T + dT$ and moment $M + dM$ defined in a positive direction. The given coordinate system also undergoes translation along the y direction in inertial space. Furthermore, let m be the mass per unit length along the beam.

If we assume that the element does not undergo deformation in the x-direction (that is, $u(s,t) = 0$), this implies that the sum of forces acting on the element in the x direction is zero. Thus,

$$F_x ds + (T + dT) - T = 0, \tag{A.0.1}$$

$$F_x ds + dT = 0, \tag{A.0.2}$$

$$\frac{dT}{dx} = -F_x, \tag{A.0.3}$$

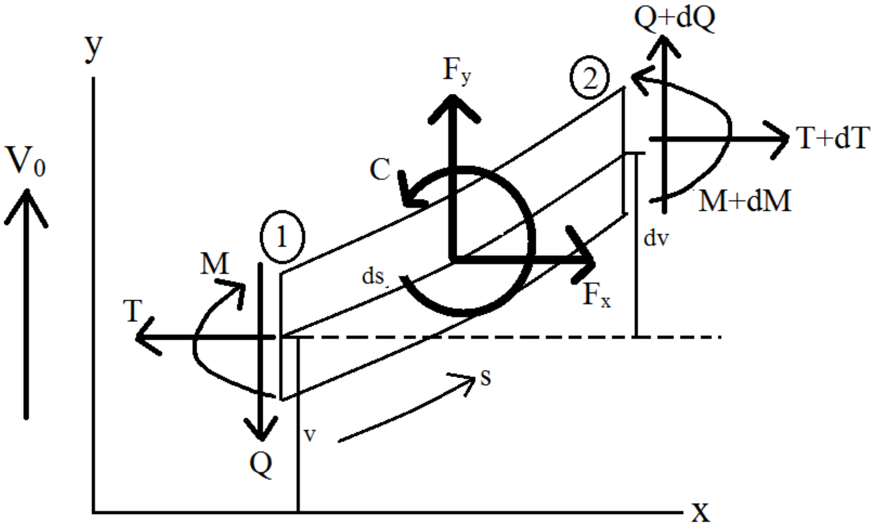

Figure A.1: Coordinate system and related quantities for the differential beam element.

$$T(s) = -\int_0^s F_x\,ds + c. \tag{A.0.4}$$

We see that $T(0) = c$. However, $T(0)$ is simply the axial reaction force at the cantilever point $s = 0$ in reaction to the applied axial body force F_x over the whole beam, and so $T(0) = \int_0^L F_x\,ds$. Thus,

$$T(s) = -\int_0^s F_x\,ds + \int_0^L F_x\,ds, \tag{A.0.5}$$

$$\boxed{T(s) = \int_s^L F_x\,ds.} \tag{A.0.6}$$

We now consider forces in the y direction. Doing this gives

$$(Q + \partial Q) - Q + F_y \partial s = (m\,\partial s)(\ddot{v} + \ddot{V}_0), \tag{A.0.7}$$

$$\frac{\partial Q}{\partial s} + F_y = m(\ddot{v} + \ddot{V}_0), \tag{A.0.8}$$

where we have replaced normal derivatives with partial derivatives to account for the dependence of quantities on v and therefore on t since v is a function of t.

To find an expression for $\frac{\partial Q}{\partial s}$, we consider a moment balance about the mid-point of side 2. Assuming that $ds \approx dx$, this gives

$$M - (M + \partial M) - C\,\partial s + T\,\partial v - Q\,\partial s = 0, \tag{A.0.9}$$

$$-\partial M - C\,\partial s + T\,\partial v - Q\,\partial s = 0, \tag{A.0.10}$$

$$Q = -\frac{\partial M}{\partial s} - C + T\frac{\partial v}{\partial s}, \tag{A.0.11}$$

$$\frac{\partial Q}{\partial s} = -\frac{\partial^2 M}{\partial s^2} - \frac{\partial C}{\partial s} + \frac{\partial}{\partial s}\left(T\frac{\partial v}{\partial s}\right). \tag{A.0.12}$$

and so substituting equation A.0.12 into equation A.0.8 gives

$$F_y - \frac{\partial^2 M}{\partial s^2} - \frac{\partial C}{\partial s} + \frac{\partial}{\partial s}\left(T\frac{\partial v}{\partial s}\right) = m(\ddot{v} + \ddot{V_0}). \tag{A.0.13}$$

Euler-Bernoulli beam theory states that the bending moment M is related to the displacement v by

$$M = D\frac{\partial^2 v}{\partial s^2}, \tag{A.0.14}$$

where $D = EI$, E is the Young's Modulus of the beam material and I is the second area moment of inertia [20].

Hence, substituting equation A.0.14 for the bending moment into equation A.0.13 gives

$$F_y - D\frac{\partial^4 v}{\partial s^4} - \frac{\partial C}{\partial s} + \frac{\partial}{\partial s}\left(T\frac{\partial v}{\partial s}\right) = m(\ddot{v} + \ddot{V_0}). \tag{A.0.15}$$

or

$$\boxed{F_y - D\frac{\partial^4 v}{\partial s^4} + \frac{\partial}{\partial s}\left(-C + T\frac{\partial v}{\partial s}\right) = m(\ddot{v} + \ddot{V_0}).} \tag{A.0.16}$$

which is the PDE that is given in equation 2.1.1.

We can also substitute equation A.0.14 into equation A.0.11 to get

$$Q = -D\frac{\partial^3 v}{\partial s^3} - C + T\frac{\partial v}{\partial s}, \tag{A.0.17}$$

The spatial cantilever boundary conditions are given as follows:

1. Zero displacement at cantilever point : $v(0, t) = 0$.
2. Zero slope at cantilever point : $\frac{\partial v}{\partial s}(0, t) = 0$.
3. Zero moment at beam tip : $M(L) = 0$, so $\frac{\partial^4 v}{\partial s^4}(L, t) = 0$ from equation A.0.14.
4. Zero shear at beam tip : $Q(L) = 0$, so $D\frac{\partial^3 v}{\partial s^3}(L, t) + C(L, t) = 0$ from equation A.0.17.

Appendix B

Derivation of the governing ODE for the modal amplitude $a(t)$

The governing partial differential equation given for $v(t)$ in equation 2.1.2 (which was also derived in Appendix A) is repeated below:

$$F_y - Dv'''' - C' + [Tv']' = m\left(\ddot{v} + \ddot{V_0}\right), \tag{B.0.1a}$$

$$T = \int_s^L F_x \, ds. \tag{B.0.1b}$$

We substitute the single-mode approximation $v(s,t) = \phi(s)a(t)$ to obtain

$$F_y - D\phi''''a - C' + [T\phi']' \, a = m\phi\ddot{a} + m\ddot{V_0}. \tag{B.0.2}$$

We then multiply both sides of equation B.0.2 by $\phi(s)$ and then take the integral over s from 0 to L for both sides to get

$$\int_0^L F_y\phi \, ds - Da\int_0^L \phi''''\phi \, ds - \int_0^L C'\phi \, ds + a\int_0^L [T\phi']' \, \phi \, ds = m\ddot{a}\int_0^L \phi^2 \, ds + m\ddot{V_0}\int_0^L \phi \, ds. \tag{B.0.3}$$

Using the single-mode approximation, the spatial boundary conditions for a cantilevered beam under a body forces and moments (See Appendix A) imply that:

1. $\phi(0) = 0$ (Zero displacement at cantilever point),

2. $\phi'(0) = 0$ (Zero slope at cantilever point),

3. $\phi''(L) = 0$ (Zero moment at beam tip),

4. $Da\phi'''(L) + C(L) = 0$ (Zero shear at beam tip),

5. $T(L) = 0$ (From the definition of T in equation B.0.1)

Looking at the terms in equation B.0.3 and using integration by parts, we have

$$a\int_0^L [T\phi']'\,\phi\,ds = a\left(T\phi'\phi\big|_0^L - \int_0^L T\phi'^2\,ds\right) = -a\int_0^L T\phi'^2\,ds, \tag{B.0.4}$$

and

$$\begin{aligned}
&- Da\int_0^L \phi''''\phi\,ds - \int_0^L C'\phi\,ds \\
&= -Da\left(\phi'''\phi\big|_0^L - \phi''\phi'\big|_0^L + \int_0^L \phi''^2\,ds\right) - \left(C\phi\big|_0^L - \int_0^L C\phi'\,ds\right) \\
&= -Da\phi'''(L)\phi(L) - C(L)\phi(L) - Da\int_0^L \phi''^2\,ds + \int_0^L C\phi'\,ds \qquad \text{(B.0.5)} \\
&= -\phi(L)\left[Da\phi'''(L) + C(L)\right] - Da\int_0^L \phi''^2\,ds + \int_0^L C\phi'\,ds \\
&= -Da\int_0^L \phi''^2\,ds + \int_0^L C\phi'\,ds,
\end{aligned}$$

Also, we have defined ϕ such that $\int_0^L \phi^2\,ds = 1$. Hence, substituting equations B.0.4 and B.0.5 into equation B.0.3 gives

$$\int_0^L F_y\phi\,ds - Da\int_0^L \phi''^2\,ds + \int_0^L C\phi'\,ds - a\int_0^L T\phi'^2\,ds = m\ddot{a} + m\ddot{V}_0\int_0^L \phi\,ds. \tag{B.0.6}$$

Rearranging terms gives

$$m\ddot{a} = \int_0^L C\phi'\,ds - \left[\int_0^L T\phi'^2\,ds + D\int_0^L \phi''^2\,ds\right]a + \int_0^L F_y\phi\,ds - m\ddot{V}_0\int_0^L \phi\,ds \tag{B.0.7}$$

which is the desired equation in equation 2.1.4.

Appendix C

Derivation of equation for magnetization of beam

For any given point on the beam, let $\hat{\mathbf{a}}$ be a unit vector tangent to the beam at that point, and let $\hat{\mathbf{n}}$ be a unit vector normal to the beam at that point. For the coordinate system shown in figure 2.1, let $\hat{\mathbf{i}}$ be a unit vector along the x-axis and $\hat{\mathbf{j}}$ be a unit vector along the y-axis. Let γ and ψ be angles defined against the local magnetic field $\mathbf{B}$ for the x-axis and the beam respectively, as illustrated in figure C.1. The geometry is such that $\psi = \frac{\pi}{2} + \theta - \gamma$.

Let B_0 be the magnitude of the magnetic field at the point on the beam. Thus, we can define $B_x = B_0 cos(\gamma)$ and $B_y = B_0 sin(\gamma)$, where $\mathbf{B} = B_x\,\hat{\mathbf{i}} + B_y\,\hat{\mathbf{j}}$

Under the assumptions given in section 2.2, the magnetization per unit length of the

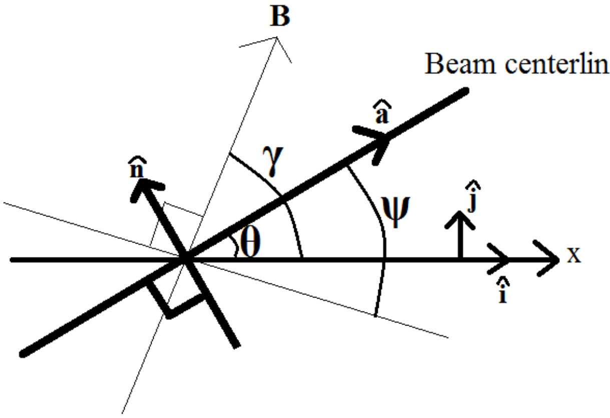

Figure C.1: Coordinate systems and relevant angles. Adapted from figure 4b) in [1].

beam in the magnetic field can be written as [11]

$$\mathbf{M} = \frac{\chi A B_0}{\mu_0 \mu_r}(cos(\psi)\,\hat{\mathbf{n}} + \mu_r sin(\psi)\,\hat{\mathbf{a}}), \tag{C.0.1}$$

where A is the cross-sectional area of the beam, χ is the volumetric magnetic susceptibility of the beam material, $\mu_r = \chi + 1$ is the relative magnetic permeability and μ_0 is the magnetic constant, $\mu_0 = 4\pi * 10^{-7}\frac{Vs}{mA}$.

We want to write $\mathbf{M}$ in the form $\mathbf{M} = M_x\hat{\mathbf{i}} + M_y\,\hat{\mathbf{j}}$. The coordinate systems are related by the rotation

$$\begin{aligned} \hat{\mathbf{a}} &= cos(\theta)\,\hat{\mathbf{i}} + sin(\theta)\,\hat{\mathbf{j}}, \\ \hat{\mathbf{n}} &= -sin(\theta)\,\hat{\mathbf{i}} + cos(\theta)\,\hat{\mathbf{j}}. \end{aligned} \tag{C.0.2}$$

Hence,

$$\mathbf{M} = \frac{\chi A B_0}{\mu_0 \mu_r}\left[cos\left(\frac{\pi}{2} + \theta - \gamma\right)(-sin(\theta)\,\hat{\mathbf{i}} + cos(\theta)\,\hat{\mathbf{j}}) + \mu_r\, sin\left(\frac{\pi}{2} + \theta - \gamma\right)(cos(\theta)\,\hat{\mathbf{i}} + sin(\theta)\,\hat{\mathbf{j}})\right]. \tag{C.0.3}$$

Since

$$\begin{aligned} &B_0 cos\left(\frac{\pi}{2} + \theta - \gamma\right) \\ &= B_0(cos(\theta)sin(\gamma) - sin(\theta)cos(\gamma)) \\ &= B_y cos(\theta) - B_x sin(\theta), \end{aligned} \tag{C.0.4}$$

and similarly

$$\begin{aligned} &B_0 sin\left(\frac{\pi}{2} + \theta - \gamma\right) \\ &= B_y sin(\theta) + B_x cos(\theta). \end{aligned} \tag{C.0.5}$$

Thus, we have

$$\begin{aligned} \mathbf{M} = \frac{\chi A}{\mu_0 \mu_r}&[(B_y cos(\theta) - B_x sin(\theta))(-sin(\theta)\,\hat{\mathbf{i}} + cos(\theta)\,\hat{\mathbf{j}}) \\ &+ \mu_r\,(B_y sin(\theta) + B_x cos(\theta))(cos(\theta)\,\hat{\mathbf{i}} + sin(\theta)\,\hat{\mathbf{j}})]. \end{aligned} \tag{C.0.6}$$

Rearranging the terms along with using $\mu_r = \chi + 1$ gives

$$\begin{aligned} \mathbf{M} = \frac{\chi A}{\mu_0 \mu_r}&([(1 + \chi cos^2(\theta))B_x + \chi\sin(\theta)cos(\theta)B_x]\hat{\mathbf{i}} \\ &+ [\chi sin(\theta)cos(\theta)B_x + (1 + \chi sin^2(\theta))B_y]\hat{\mathbf{j}}). \end{aligned} \tag{C.0.7}$$

Thus,

$$M_x = \frac{\chi A}{\mu_0 \mu_r} \left[(1 + \chi cos^2(\theta)) B_x + \chi \sin(\theta) cos(\theta) B_y \right] \tag{C.0.8a}$$

$$M_y = \frac{\chi A}{\mu_0 \mu_r} \left[\chi sin(\theta) cos(\theta) B_x + (1 + \chi sin^2(\theta)) B_y \right] \tag{C.0.8b}$$

Appendix D

Creo (Pro/E) Model

The mainframe along with the magnets are modelled in Pro/E. The model is shown in figure D.1.

The mass properties are shown in figure D.2, with the center of mass of the system indicated relative to the Pro/E coordinate system. We see that the axis of the connection hole is close to the lateral and vertical components of the center of mass of the system.

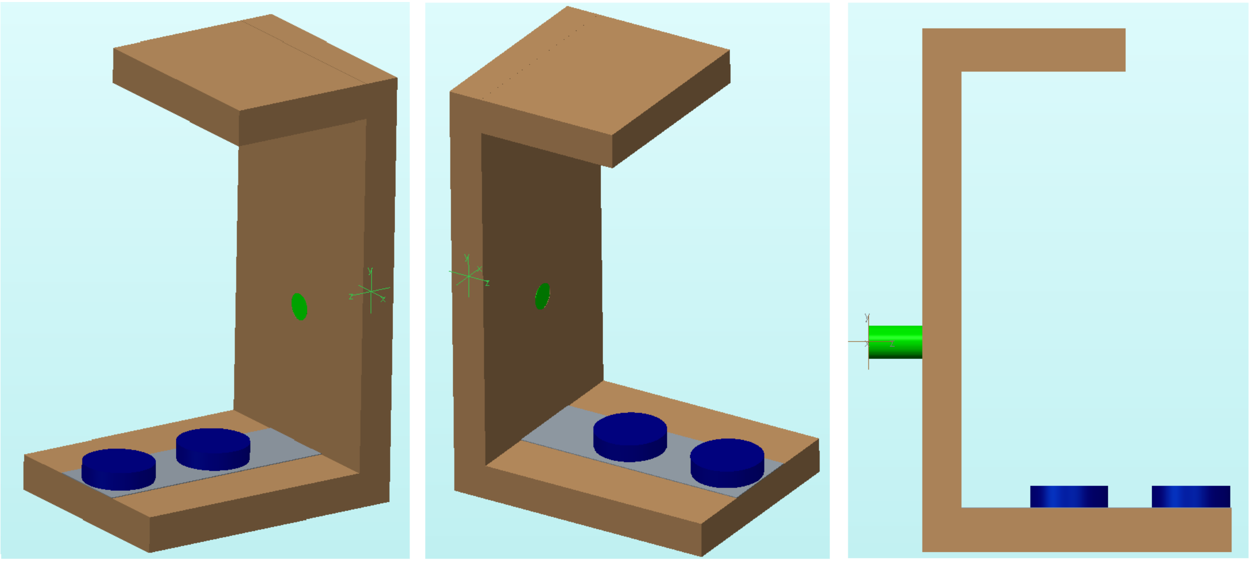

Figure D.1: Various views of mainframe model with indicated Pro/E coordinate system along the axis of the connection hole to the shaker.

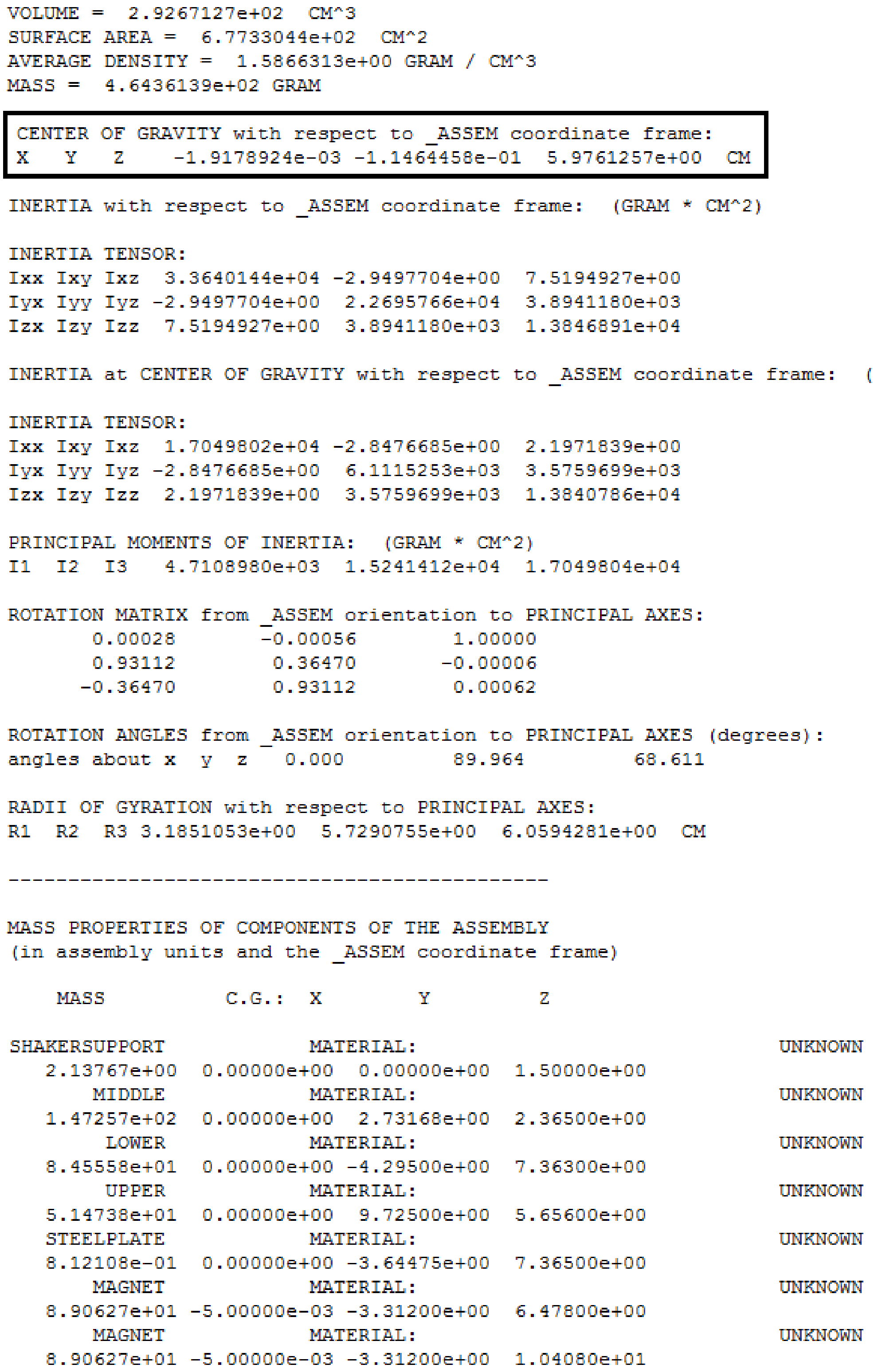

```
VOLUME =  2.9267127e+02  CM^3
SURFACE AREA =  6.7733044e+02  CM^2
AVERAGE DENSITY =  1.5866313e+00 GRAM / CM^3
MASS =  4.6436139e+02 GRAM

CENTER OF GRAVITY with respect to _ASSEM coordinate frame:
X   Y   Z    -1.9178924e-03 -1.1464458e-01  5.9761257e+00  CM

INERTIA with respect to _ASSEM coordinate frame:  (GRAM * CM^2)

INERTIA TENSOR:
Ixx Ixy Ixz  3.3640144e+04 -2.9497704e+00  7.5194927e+00
Iyx Iyy Iyz -2.9497704e+00  2.2695766e+04  3.8941180e+03
Izx Izy Izz  7.5194927e+00  3.8941180e+03  1.3846891e+04

INERTIA at CENTER OF GRAVITY with respect to _ASSEM coordinate frame:  (GRAM * CM^2)

INERTIA TENSOR:
Ixx Ixy Ixz  1.7049802e+04 -2.8476685e+00  2.1971839e+00
Iyx Iyy Iyz -2.8476685e+00  6.1115253e+03  3.5759699e+03
Izx Izy Izz  2.1971839e+00  3.5759699e+03  1.3840786e+04

PRINCIPAL MOMENTS OF INERTIA:  (GRAM * CM^2)
I1  I2  I3   4.7108980e+03  1.5241412e+04  1.7049804e+04

ROTATION MATRIX from _ASSEM orientation to PRINCIPAL AXES:
       0.00028       -0.00056       1.00000
       0.93112        0.36470      -0.00006
      -0.36470        0.93112       0.00062

ROTATION ANGLES from _ASSEM orientation to PRINCIPAL AXES (degrees):
angles about x  y  z   0.000         89.964         68.611

RADII OF GYRATION with respect to PRINCIPAL AXES:
R1  R2  R3 3.1851053e+00  5.7290755e+00  6.0594281e+00  CM

---------------------------------------------

MASS PROPERTIES OF COMPONENTS OF THE ASSEMBLY
(in assembly units and the _ASSEM coordinate frame)

    MASS          C.G.:  X        Y         Z

SHAKERSUPPORT           MATERIAL:                              UNKNOWN
   2.13767e+00  0.00000e+00  0.00000e+00  1.50000e+00
       MIDDLE           MATERIAL:                              UNKNOWN
   1.47257e+02  0.00000e+00  2.73168e+00  2.36500e+00
        LOWER           MATERIAL:                              UNKNOWN
   8.45558e+01  0.00000e+00 -4.29500e+00  7.36300e+00
        UPPER           MATERIAL:                              UNKNOWN
   5.14738e+01  0.00000e+00  9.72500e+00  5.65600e+00
   STEELPLATE           MATERIAL:                              UNKNOWN
   8.12108e-01  0.00000e+00 -3.64475e+00  7.36500e+00
       MAGNET           MATERIAL:                              UNKNOWN
   8.90627e+01 -5.00000e-03 -3.31200e+00  6.47800e+00
       MAGNET           MATERIAL:                              UNKNOWN
   8.90627e+01 -5.00000e-03 -3.31200e+00  1.04080e+01
```

Figure D.2: Mass properties of Pro/E model, with center of mass of system indicated relative to the coordinate system.

Appendix E

Circuit Schematic

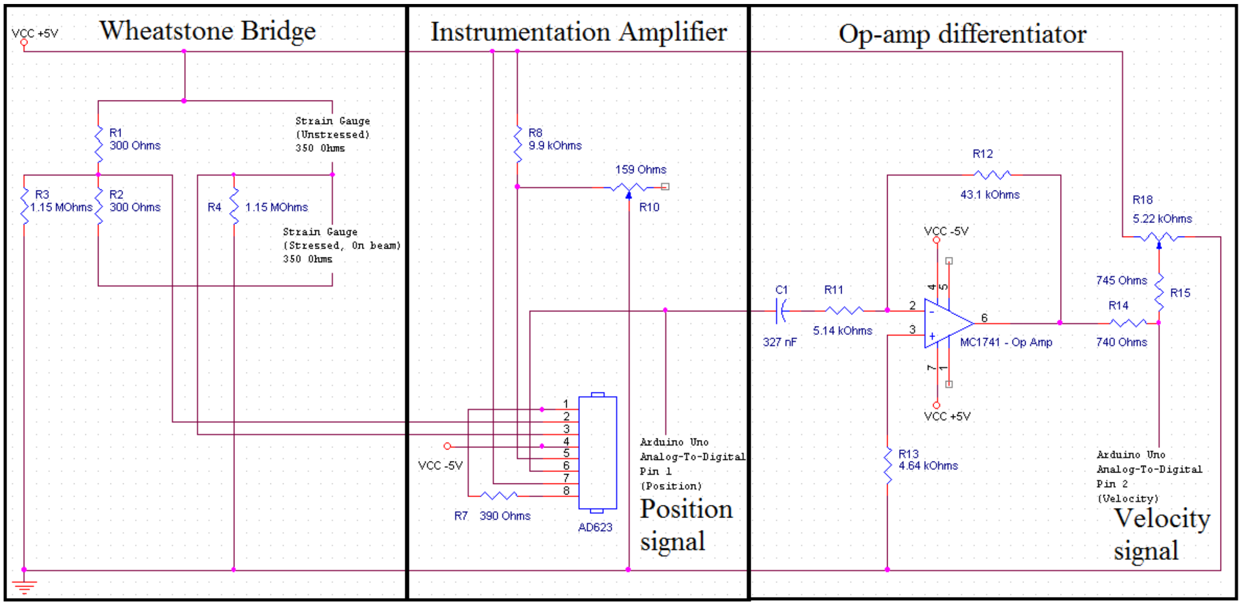

Figure E.1: Schematic of electronic used to collect and process data, with major circuit blocks indicated.

Appendix F

Matlab Code

We present the main code that was used to calculate F_{static} and obtain data from numerical simulations. Other secondary code was written to process the generated data, but they are omitted here as the goal is to show the main algorithms used to compute F_{static}.

Two important differences in the code must be noted:

1. The coordinate system in the code is different from the coordinate system given in the text above. The coordinate system zero is located at the base directly below the vertical beam position. The “x” axis in the code corresponds to the “y” axis in text, and the “y” axis in the code corresponds to the “-x” axis in the text.
2. The variable ”d” in the code refers to the distance between the closer edges of the magnets, and not the distance between magnet centers. This was done because it is experimentally easier to measure the former.

F.1 Main Script to calculate F_{static} and perform numerical simulations

```
%%%%%%%%%%%%% Input Parameters %%%%%%%%%%%%%%%%%%%%%%%%%%%%%%%%%%%
%Electromagnetic constants/Properties
miu_0 = 4*pi*10^-7;  %Permeability, T m/A
Xi = 1*10^3;          %Susceptibility
miu_r = Xi + 1;       %Relative permeability
```

```
%Beam Properties
L = 10.88*10^-2;                  %Length of beam, m
thickness = 0.254*10^-3;         %Thickness of beam, m
rho = 7.833*10^3;                %Density of beam, kg/m^3
width = 0.95*10^-2;%5.4*10^-3;  %Width of beam,m
Area = width*thickness;          %Cross-sectional area of beam, m^2
E = 206843*10^6;                 % Young's Modulus, Pa
I = (width*thickness^3)/12;      % Moment of Inertia, m^4
D = E*I;                         % N m^2

m = rho*Area;               %Mass of beam per length kg/m

%Magnet Properties
radiusMagnet = 2.54/2*10^-2;      %m
heightMagnet = radiusMagnet/2;    %m
B_CenterSurface1 = 0.21;          %Magnet field strength of magnet 1, T
B_CenterSurface2 = 0.21;          %Magnet field strength of magnet 1, T

%Magnet Placement
d = 1.39*10^-2;          %Spacing between edges of magnets, m
h = 12.8*10^-2 - L;      %Height of beam tip above ground, m
offset = 0;

%Shaker parameters
omega = 12*2*pi;    %Frequency, rad/s
A0 = 0;%7*10^-3;    %4.6*4.5/12*10^-2;      %Peak displacement, m

%Damping
delta = 6.2;
%%%%%%%%%%%%%%%%%%%%%%%%%%%%%%%%%%%%%%%%%%%%%%%%%%%%%%%%%%%%%%%%%%%%

%Equations for Phi (beam mode), its derivatives and related quantities
%(Constant Beam mode)
modeConst = 1.875104069;
k = modeConst/L;
                                  points = 2000; %Number of grid points over s
```

```
s = linspace(0,L,points)';
delX = (s(2,1)-s(1,1));

K = (-cos(modeConst)-cosh(modeConst))/(sin(modeConst)+sinh(modeConst));

Phi = 0.5*(K*(sin(k*s)-sinh(k*s))+(cos(k*s)-cosh(k*s)));

normalizer = -1/sqrt(delX*trapz(Phi.^2));
Phi = normalizer*Phi;

dPhi     = normalizer*0.5*k*   (K*(cos(k*s)-cosh(k*s))+(-sin(k*s)-sinh(k*s)));
ddPhi    = normalizer*0.5*k^2*(K*(-sin(k*s)-sinh(k*s))+(-cos(k*s)-cosh(k*s)));
dddPhi   = normalizer*0.5*k^3*(K*(-cos(k*s)-cosh(k*s))+(sin(k*s)-sinh(k*s)));
ddddPhi  = normalizer*0.5*k^4*(K*(sin(k*s)-sinh(k*s))+(cos(k*s)-cosh(k*s)));

dPhiSquared = dPhi.*dPhi;

Int_Phi = delX*trapz(Phi);
Int_Phi_Squared = delX*trapz(Phi.^2);
Int_dPhi_Squared = delX*trapz(dPhi.^2);
Int_ddPhi_Squared = delX*trapz(ddPhi.^2);

Phi_L = Phi(end);
dPhi_L = dPhi(end);
dddPhi_L = dddPhi(end);
%%%%%%%%%%%%%%%%%%%%%%%%%%%%%%%%%%%%%%%%%%%%%%%%%%%%%%%%%%%%%%%%%%%%%%%%

%%%% Calculate all Forces %%%%
%Modal displacement
gridStart =  -(d/2+2*radiusMagnet);
gridEnd = (d/2+2*radiusMagnet);
                                        n = 1000; %Grid points over modal displacement
del = (gridEnd-gridStart)/n;

a = [gridStart:del:gridEnd]/Phi_L;
```

```
%Displacement across all of the beam for each modal displacement
v = zeros(size(s,1),size(a,2));
v = Phi*a;
Fx = zeros(size(v,1),size(v,2));
Fy = zeros(size(v,1),size(v,2));
kappa = zeros(size(v,1),size(v,2));
Moment = zeros(size(v,1),size(v,2));

y = h+L-s;

for i = 1 : size(v,2) %For each modal displacement
    i/size(v,2)
    theta = dPhi*a(1,i);

    x = v(:,i);

    [Fx(:,i) Fy(:,i) kappa(:,i)  C(:,i)] =
    getMagneticForce(radiusMagnet, heightMagnet/2,d,offset,B_CenterSurface1,...
    B_CenterSurface2,width,thickness,Xi,theta,x,y,0.00000000001,0.00000000001);
end

ds = delX;

%Calculate terms in static force distribution
CumFy = ds*cumtrapz(-Fy,1);
TL = CumFy(end,:);
T = ones(size(CumFy,1),1)*TL-CumFy;

tip = a*Phi_L;  %Beam tip displacement

TransverseForce = ds*trapz(Fx.*(Phi*ones(1,size(Fx,2))),1)./(m*Int_Phi_Squared)*Phi_L;
momentForce = (ds*trapz(C.*(dPhi*ones(1,size(C,2))), 1))./(m*Int_Phi_Squared)*Phi_L;
AxialForce = -ds*trapz(  T.*(dPhiSquared*ones(1,size(T,2))),1)./(m*Int_Phi_Squared).*tip;
BeamForce = -D*Int_ddPhi_Squared./(m*Int_Phi_Squared)*tip;

magneticForce =  TransverseForce + momentForce + AxialForce;
```

```
TotalForce = magneticForce  + BeamForce;

%Plot static force distribution
figure();
hold on;
plot(tip,TransverseForce,tip,momentForce,tip,AxialForce,tip,BeamForce,tip,TotalForce);
grid on;
hold off;
legend('F_{Transverse}','F_{Moment}','F_{Axial}','F_{Beam}','F_{static}');
xlabel('Beam Tip Displacement, v_{tip} (m)');
ylabel('Force/Mass (N/kg)');

%Forcing amplitude for Duffing oscillator.
F = Int_Phi*omega^2*A0*Phi_L/(Int_Phi_Squared);

%Numerical Simulation
t0 = 0;   %Initial time (s)
tf = 10;  %Final time (s)

x0 = [1*10^-2 0]'; %Initial point

Period = 2*pi/omega; %Forcing Period

NumPoincarePoints = (tf-t0)/Period;
NumMiddlePoints = 1000; %Number of points between Poincare points

tspan = t0:Period/NumMiddlePoints:tf; %Time points

% Set tolerances
options = odeset('OutputSel',1, 'OutputFcn',@odeplot,'RelTol',10^-10,'AbsTol',10^-8);
figure();
[t,y] = ode113(@BeamEndSimTableLookup,tspan,x0,options,tip,TotalForce,delta,F,omega);

%%% Plot Poincare Map %%%
index = [1:NumMiddlePoints:size(t,1)];
tP = tspan(index);
```

```
yP1 = y(index,1);
yP2 = y(index,2);



timeFrac = 0.8; %Fraction of time series to use in poincare Map
sizeT = size(t,1);
timeSize = ceil((1-timeFrac)*sizeT)+1;

c = colormap(jet(size(yP1,1))); %use colors

figure()
hold on;
for i = 1 : size(yP1,1)
    plot(yP1(i),yP2(i),'.','MarkerSize',4,'Color',c(i,:)');
end
hold off;
xlabel('Displacement␣,a␣␣(m)');
ylabel('Velocity␣,␣a␣(m/s)');
    minX = min(min(y(:,1)));
    maxX = max(max(y(:,1)));
    minY = min(min(y(:,2)));
    maxY = max(max(y(:,2)));
    axis([minX maxX minY maxY]);
    grid on;



%%% plot FFT of time series %%%
FFTSampleFrac = 0.7; %Fraction of time series to use in FFT

ySample = y( floor(size(t,1)*(1-FFTSampleFrac)) : size(t,1),:);
tSample = t(floor(size(t,1)*(1-FFTSampleFrac)) : size(t,1));

averageDt = mean(diff(tSample));
SampleFreq = 1/averageDt;
SampleLength = size(ySample(:,1),1);
NFFT = 2^nextpow2(SampleLength);
```

```
yFFT = fft(ySample(:,1)-mean(ySample(:,1)),NFFT)/SampleLength;
f = SampleFreq/2*linspace(0,1,NFFT/2+1);

figure();
plot(f,abs(yFFT(1:NFFT/2+1)));
xlabel('Frequency␣(Hz)')
ylabel('FFT␣Power')
```

F.2 Function to compute magnetic forces and moments

```
function [Fx Fy kappa C] = getMagneticForce(a,b,d,offset,...
B_CenterSurface1,B_CenterSurface2,width,thickness, Xi, theta, xPoint,yPoint, dx, dy)

%Calculate magnetic field strengths and derivatives of two magnets
[Bx By dBxx dByy dBxy dByx] = PointTwoMagnetFieldDerivatives(a,b,d,offset...
,B_CenterSurface1,B_CenterSurface2, xPoint,yPoint, dx, dy);

%Multiplication constant
c = Xi*width*thickness/((4*pi*10^-7)*(Xi+1));

%Magnetizations
M1 = c*(-(1+Xi*cos(theta).^2).*By + Xi*sin(theta).*cos(theta).*Bx);
M2 = c*(-Xi*sin(theta).*cos(theta).*By + (1+Xi*sin(theta).^2).*Bx);

%x and y forces
Fy = -(M1.*dByy + M2.*-dByx);
Fx = M1.*-dBxy + M2.*dBxx;

B2 = 2*(Xi)*(-By).*(Bx);
B3 = Xi*(By.^2-Bx.^2);

%Moments
C = 1/2*c*(B2.*cos(2*theta)-B3.*sin(2*theta));

end
```

F.3 Function to compute magnetic field and derivatives

```
function [Bx By dBxx dByy dBxy dByx] = PointTwoMagnetFieldDerivatives(a,b,d,offset...
,B_CenterSurface1,B_CenterSurface2, xPoint,yPoint, dx, dy)
%First magnet
nI1 = (sqrt((2*b)^2+a^2)/b)*(B_CenterSurface1)/(4*pi*10^-7);

n = size(xPoint,1); %Number of points

%Radial and height components of magnetic field
Br1 = zeros(n,9); Bz1 = zeros(n,9);
Br2 = zeros(n,9); Bz2 = zeros(n,9);

%Grid scheme
%      7
%      6
% 1 2  5 8 9
%      4
%      3

%Magnet position
yCenter = b; xCenter = -(d/2+a+offset);

xMid = xPoint-xCenter;
yMid = yPoint-yCenter;

%Number of beam points across rows
%Number of integration points across columns
xArray = [xMid-2*dx, xMid-dx, xMid, xMid, xMid, xMid, xMid, xMid+dx, xMid+2*dx];
yArray = [yMid, yMid, yMid-2*dy, yMid-dy, yMid, yMid+dy, yMid+2*dy, yMid, yMid];

%Calculate magnetic field from magnet 1
for i = 1 : 9
    x = xArray(:,i);
```

```
    y = yArray(:,i);

   [Bi Bj] = BFieldCylinder(b,a,nI1,abs(x),y);

    Br1(:,i) = sign(x).*Bi;
    Bz1(:,i) = Bj;
end

%Second magnet
nI2 = (sqrt((2*b)^2+a^2)/b)*(B_CenterSurface2)/(4*pi*10^-7);

%Magnet position
yCenter = b; xCenter = (d/2+a-offset);

xMid = xPoint-xCenter;
yMid = yPoint-yCenter;

xArray = [xMid-2*dx, xMid-dx, xMid, xMid, xMid, xMid, xMid, xMid+dx, xMid+2*dx];
yArray = [yMid, yMid, yMid-2*dy, yMid-dy, yMid, yMid+dy, yMid+2*dy, yMid, yMid];

%Calculate magnetic field from magnet 2
for i = 1 : 9
    x = xArray(:,i);
    y = yArray(:,i);

   [Bi Bj] = BFieldCylinder(b,a,nI2,abs(x),y);

    Br2(:,i) = sign(x).*Bi;
    Bz2(:,i) = Bj;
end

%Compute total magnetic field and derivatives
Br = Br1 + Br2;
Bz = Bz1 + Bz2;

Bx = Br(:,5);
```

```
By = Bz(:,5);

%Derivatives
dBxx = (1/12*Br(:,1)-2/3*Br(:,2)+2/3*Br(:,8)-1/12*Br(:,9))/(dx);
dByy = (1/12*Bz(:,3)-2/3*Bz(:,4)+2/3*Bz(:,6)-1/12*Bz(:,7))/(dx);
dBxy = (1/12*Br(:,3)-2/3*Br(:,4)+2/3*Br(:,6)-1/12*Br(:,7))/(dx);
dByx = (1/12*Bz(:,1)-2/3*Bz(:,2)+2/3*Bz(:,8)-1/12*Bz(:,9))/(dx);

end
```

F.4 Function to calculate magnetic field of an ideal solenoid

Algorithm adapted from [6].

```
%Cylinder has height '2b'
%Cylinder has radius 'a'
%Equivalent Solenoid with 'n' turns per unit length carrying current 'I'
function [B_r, B_z] = BFieldCylinder(b, a, nI, r, z)
miu_0 = 4*pi*10^-7;

B_0 = (miu_0/pi)*nI; %Magnetic field on magnet surface.

zPlus = z + b;
zMinus = z - b;

aPlus = a./sqrt(zPlus.^2 + (r+a).^2);
aMinus = a./sqrt(zMinus.^2 + (r+a).^2);

bPlus = zPlus./sqrt(zPlus.^2 + (r+a).^2);
bMinus = zMinus./sqrt(zMinus.^2 + (r+a).^2);

gamma = (a-r)./(a+r);

kPlus = sqrt( (zPlus.^2 + (a-r).^2)./(zPlus.^2 + (a+r).^2) );
kMinus = sqrt( (zMinus.^2 + (a-r).^2)./(zMinus.^2 + (a+r).^2) );
```

```
onezies = ones(size(gamma,1),size(gamma,2));

B_r = B_0*(aPlus.*EllipInt(kPlus,onezies,onezies,-onezies)
-aMinus.*EllipInt(kMinus,onezies,onezies,-onezies));

B_z = (B_0*a./(a+r)).*(bPlus.*EllipInt(kPlus,abs(gamma),onezies,gamma)
-bMinus.*EllipInt(kMinus,abs(gamma),onezies,gamma));
end
```

F.5 Function to compute generalized elliptic integral

Algorithm taken from [6].

```
function [out] = EllipInt(kc,p,c,s)

tol = 0.0001;

k = abs(kc);

pp = p;
cc = c;
ss = s./pp;
em = ones(size(kc,1),size(kc,2));

f = cc;
cc = cc + ss./pp;
g = k./pp;
ss = 2.*(ss+f.*g);
pp = g + pp;
g = em;
em = k + em;
kk = k;

while(1)
    k = 2.*sqrt(kk);
```

```
        kk = k.*em;
        f = cc;
        cc = cc + ss./pp;
        g = kk./pp;
        ss = 2.*(ss + f.*g);
        pp = g + pp;
        g = em;
        em = k + em;

        if(abs(g-k) < g*tol)
            break;
        end
end

out = pi/2.*(ss + cc.*em)./(em.*(em+pp));
end
```